Piezoelectric composite films for energy harvesting devices

Doctoral Dissertation
Doctoral Program in Materials Science and Technology (XXXII Cycle)

Piezoelectric composite films for energy harvesting devices

Donatella Duraccio
* * * * * *

Supervisor
Prof. Giulio Malucelli

Politecnico di Torino
July 29, 2020

I hereby declare that, the contents and organisation of this dissertation constitute my own original work and does not compromise in any way the rights of third parties, including those relating to the security of personal data.

…….

Donatella Duraccio

Turin, July 29, 2020

Summary

The main aim of this work is the development of novel, flexible, efficient, versatile piezoelectric films of easy fabrication and low impact, which may lead to a real competition in the field of renewable/alternative energy technologies. Among the large variety of solutions, we decided to prepare UV-cured composites made of an acrylic resin (EB) filled with different shaped ZnO structures, synthesized on the purpose, and/or cellulose (pristine form: nanocrystals). More in detail, four different morphologies of ZnO were synthesized, following a facile aqueous sol-gel route, namely: nano-particles (ZNP), bipyramidal (ZBP), flower-like (ZNF) and long needles (ZLN) morphologies. Commercially available cellulose nanocrystals (CNC) were subjected to mechanical treatments by grinding in a mortar (C) or by ball milling (BMC). Films of 150 μm of thickness were obtained with the highest achievable cross-linking density.

For the composites containing ZnO, only EB-ZLN and EB-ZNF showed a uniform distribution and dispersion of the fillers within the polymer matrix, which was maintained also when the filler amount increased. For the composites containing cellulose, ball milling allowed obtaining a better dispersion, as well as a decrease of the size of cellulose domains embedded in the polymer matrix as compared to the composites containing grinded cellulose.

The thermal stability of the composites was not worsened by the presence of the fillers. For ZnO composites, whatever the fillers morphology was, a slight increase in the thermal stability at low temperatures was observed; besides, at higher temperatures, ZnO was found to catalyse the degradation processes. For the cellulose-containing composites (with and without ZnO), ball milled cellulose promoted a higher stability of composite films with respect to those containing grinded cellulose.

In general, the increase of filler content (ZnO, cellulose or ZnO+cellulose) caused an increase of glass transition temperature (T_g) and a decrease of the storage modulus in the glassy state. The composites containing ZnO were stiffer than those containing cellulose; besides, the samples containing grinded cellulose with or without ZnO showed higher T_g values than those containing BMC (being equal the composition).

Then, the piezoelectric response generated by the polymer composites and measured in cooperation with the Institute of Metrological Research (INRIM) of Torino (Italy) and the Institute of Microelectronics and Microsystems (IMM) of the National Research Council (CNR) in Lecce (Italy), was satisfactory in terms of RMS (root mean square) voltage measured as a function of the applied waveform, both at low and at resonance frequency. The highest voltage was registered for EB-ZNF (with and without cellulose) in all the range of analyzed frequencies. This result was explained by the higher probability that the flower-like particles, in the UV-cured films, have a higher number of 0002 planes oriented perpendicularly to the measured solicitation with respect to the other morphologies: indeed, this is due to their peculiar geometry.

Furthermore, the RMS voltage generated at 19 Hz as a function of the acceleration increased with increasing ZFL loading, reaching the maximum value at 20 wt.%, though the increase in RMS voltage was not linearly correlated with the ZFL loading. This finding was not ascribed to the dispersion of filler and to the number of particles on the surface of the composite films, but to the decrease of storage modulus of the composites at high ZFL concentration.

As far as cellulose-containing composites are considered, it worthy to underline that cellulose showed a detrimental effect on the piezoelectric properties of the composite films as compared with ZnO. This is probably due to different factors, including the lower crystallinity of cellulose, as well as the worse interfacial adhesion with the polymer matrix. Besides, though the correlation with the storage

modulus was not clearly interpreted, it seems that a lower storage modulus provides lower piezoelectricity. Finally, it was also possible to observe that ball milling process, by enhancing dispersion and distribution of cellulose within the UV-cured acrylic network, improved the piezoelectricity and dielectric values with respect to the composites containing grinded cellulose.

Despite the high gap between the measured voltage values in this PhD thesis and those related to fully inorganic piezoelectric systems (which are 2-3 orders of magnitude higher), the proposed piezoelectric films show two main advantages, i.e. flexibility and cost-effective scalability, which are key elements for the development of innovative devices in the field of green technologies and that suggest to further continue the work on energy harvesting devices.

Acknowledgment

Firstly, I would like to express my sincere gratitude to my supervisor Prof. Giulio Malucelli, not only for the chance he gave to me but also for his patience, motivation, and knowledge. In these three years, I have had the possibility to relate to him in an open, fruitful and cooperative manner.

Besides my supervisor, I would like to thank Dr. Luca Francioso (CNR- Institute of Microelectronics and Microsystems-IMM- of Lecce), Dr. Pier Paolo Capra (Institute of Metrological Research-INRIM- of Torino) and their research group for the development of the apparatus for piezoelectric measurements and for the fruitful cooperation which stimulated me to widen my research from various perspectives.

My sincere thank also goes to Dr. Maria Giulia Faga (CNR-IMAMOTER), Dr. Giovanna Maria Gautier di Confiengo (CNR-IMAMOTER) for the precious support in scanning electron measurements and commenting the research results.

I am grateful to Giuseppina Iacono, Valentina Strongone and Dr. Mattia Di Maro for supporting some of experimental measurements.

Last but not the least, I would like to thank my love Gabriele that convinced me in undertaking this adventure and my children Margherita and Giulio for the time stolen to family.

CONTENTS

General part

Chapter 1

Introduction

1.1 The energy harvesting concept

The process, by which wind, solar, thermal and mechanical sources are converted into electrical energy and stored for making self-powered systems is known as energy harvesting. The research and development of energy harvesting devices have grown rapidly in the last years, driven by the quickly increasing energy consumption and further accelerated by concerns about carbon emission from fossil fuel-based energy sources. Among the variety of renewable energy sources, the mechanical energy (e.g., pressure, bending, stretching and vibrational motions) is preferred with respect to others, because of its ubiquity and accessibility from the surroundings [1-4] There is a wide variety of mechanical energy sources including vibrations from in-body motion (such as chest and heart movement) [5] and human action from walking [6]. Their conversion into electricity has been proposed by means of piezoelectric materials by several research groups [6-8]. A piezoelectric material is able to create a potential when subjected to a mechanical stress, due to the absence of a symmetry center in its crystals. More precisely, when a vibration, tension, bending or compression [9, 10] results in a deformation of the dipole moment, a polarization phenomenon occurs, which is able to induce an external electric potential difference.

One of the advantages of piezoelectric materials for energy harvesting is the scalability at small scale that allows powering small devices where a standard battery is not a convenient or possible solution, as for example in MEMS (Micro-Electro-Mechanical System).

It already exists a number of excellent reviews in the field of energy harvesting describing not only the wide range of possible exploitable materials, but also the survey of the potential devices [11-16].

Summarizing, piezoelectric energy devices have been fabricated using both inorganic components (namely, Lead zirconate titanate (PZT) [17-19], $BaTiO_3$ (BTO)[20,21] $(Na,K,Li)NbO_3$ [22]], GaN [[23], ZnO nanowires [24,25]), organic films (poly(vinylidene fluoride) - PVDF [26, 27]), cellulose [28-30], and a combination of them [31-33], all deposited on almost all imaginable substrates [34, 35]. Among the inorganic components, PZT contains lead that is a toxic heavy metal causing environmental pollution during production and can affect the human body [36].

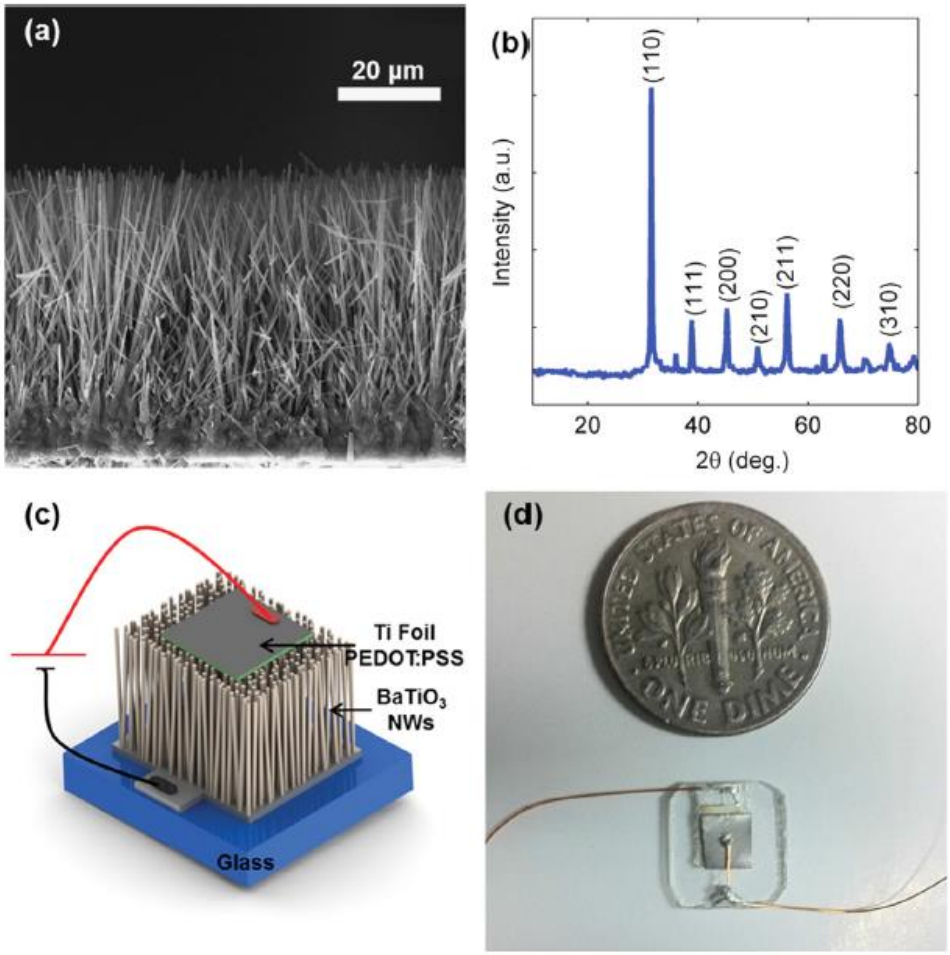

Figure 1.1. Energy harvester using BaTiO3 nanowires. (a) BTO nanowires SEM image; (b) WAXD pattern of BTO; (c) Schematic representation of BTO harvester; (d) Photograph of the BTO energy harvester with a coin for size comparison [21].

Different morphologies of BTO have been widely investigated [24, 37-42], because of its high piezoelectric coefficient and dielectric constant [43,44]. An example of energy harvesting device made with BTO is shown in Figure 1.1 [21]. There are some drawbacks in durability and flexibility of BTO, despite it

has been compounded with soft polymeric matrices such as PVDF and poly-dimethylsiloxane (PDMS) [2,45].ZnO has attracted great attention in the last years, because it possesses several key advantages: it is a biologically safe piezoelectric semiconductor occurring in a wide range of nanostructured forms by various synthetic methods. One-dimensional ZnO nanowires or arrays onto different substrates can be fabricated by thermal evaporation, vapor-liquid-solid (VLS) processes, chemical vapor deposition (CVD), whereas other morphologies such as flower-like, cauliflower-like, rodlike, hourglasslike etc can obtained by sol-gel processes, hydrothermal and solvothermal methods, laser-induced decomposition, ultra-sonic and microwave irradiation techniques and vapor phase transport [46-52]. Besides, ZnO is a potential candidate for commercial purposes, due to its inexpensiveness, relative abundance, and chemical stability in air atmosphere. Then, ZnO nanorods can growth easily in aligned arrays on plastic substrates. Figure 1.2 shows one of the first flexible harvesters, which was able to generate an open circuit voltage of 350mV [53].

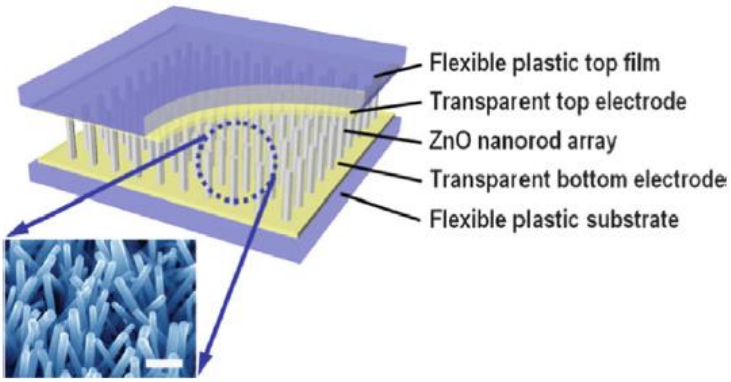

Figure 1.2. Schematic representation of a flexible energy harvester obtained by using ZnO nanorods (SEM shown in inset) grown on conductive plastic substrates. From [46].

Among the organic piezoelectric materials, PVDF is able to form thin flexible devices that can be either supported or not by a polymer substrate. Many studies have been performed also on PVDF nanocomposites, using, as example, reduced graphene oxide (RGO), $BaTiO_3$, potassium sodium niobate ($KNaNbO_3$), different metal oxides (ZnO, MgO, TiO_2), metal nanoparticles (Ag, Pt), carbon nanotubes (CNTs) [29, 54, 55]. In addition, electrospun nanofibres of PVDF have been investigated for a number of energy harvesting applications [56, 57]. More recently, cellulose has been considered in the field, although the piezoelectricity of wood was known from 1950 [58]. However, its piezoelectric constant is small, mainly due to the heterogeneous distribution of crystals and relatively low crystallinity of cellulose in the lignocellulose matrix. Given the native crystalline nature of cellulose nanocrystals (CNC), they have been reasonably studied as potential material for energy harvesting purposes [29, 30].

In a recent work, an ultrathin film of cellulose nanocrystals has been deposited on a mica substrate by using electric field assisted shear. The so-built device was able to display a piezoelectric behaviour comparable to that of some metal oxides (Figure 1.3), with a piezoelectric constant (d_{25}) of 2.1 Å/V [28].

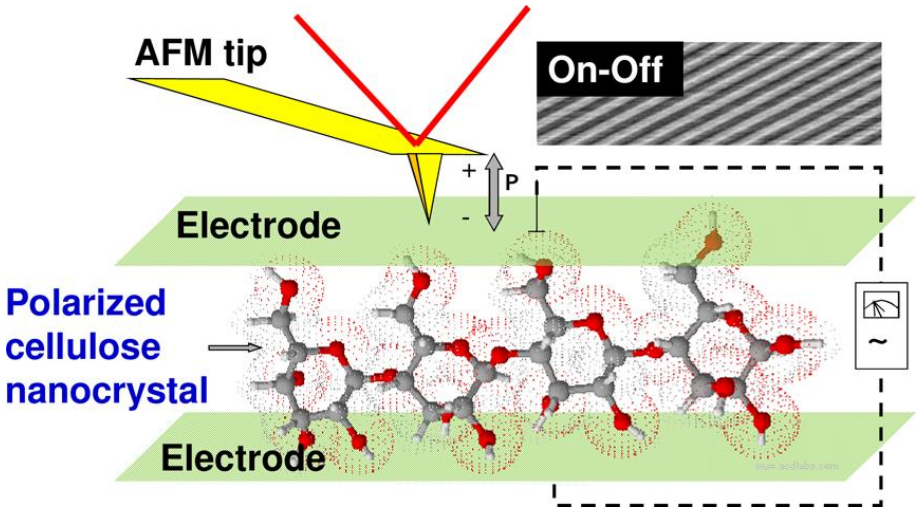

Figure 1.3. Ultrathin film of polarized cellulose nanocrystals deposited on a mica substrate with a piezoelectric constant (d_{25}) of 2.1 Å/V [28].

Although the inorganic materials have been used in energy harvesting fairly successfully, the high cost as well as the not easy integrability in a device hinder their true potentials. Furthermore, although inorganic materials

possess higher piezoelectric coefficients than polymers, they also exhibit higher elastic moduli (i.e. a higher stiffness) [59, 60], which makes them less sensitive to small vibrations and more prone to stress failure [27]. However, polymer-based generators represent a relatively small proportion of the total research and are almost exclusively based on PVDF and cellulose, which need to be polarized under high electrical fields prior to be used [27].

Furthermore, most of the strategies reported in literature involve complicated material processing and device fabrication (using precise manipulators): this, indeed, is cost and time consuming. Although these reports have made significant contributions and set benchmarks, it seems important to explore innovative, cheap, scalable technologies based on new materials, as in the present PhD thesis.

1.2. Piezoelectric systems based on ZnO composites and on cellulose

Recently, the use of ZnO dispersed in photocurable polymers has been considered for MEMS/NEMS (Micro and Nano Electro-Mechanical Systems), sensors and energy harvesting devices [61-65].

As reported in literature, ZnO nanostructures, in form of nanowires, have been used in various self-powered electronic systems [66-71].

However, despite the high piezoelectric coefficient, the applications of ZnO as nanogenerator are limited, due to its brittle nature, particularly where a high impact resistance is required. Besides, the material processing and device fabrication are often very complex and expensive. Recently, some pioneering works have explored the possibility to integrate ZnO into a photocurable polymer matrix for producing more flexible devices based on cheap and easy-to be scaled technologies [72,73].

In particular, Prashanthi et al. [72], for the first time, have integrated ZnO nanoparticles (at 20 wt.% loading) into SU-8, i.e. a commercial epoxy photoresist, to make simple lithography-based micro/nano fabrication. SU-8/ZnO composites films, 0.5 μm thick, were obtained by spin coating a mixture of components on a Ti/Au coated Si substrate at 3000 r.p.m, followed by a thermal treatment to evaporate the solvent. The piezoelectric coefficient

(d_{33}) of SU8/ZnO, measured by piezoresponse microscopy (PFM), was 6.2 pm/V, close to that of bulk ZnO [66]. Pursuing this research, Kandpal et al. [73] have extensively characterized the physical properties of the same SU-8/ZnO nanocomposite thin films at different ZnO loadings (namely, 5, 10, 15 and 20 wt.%). They also investigated the influence of ZnO filler concentration on the photo-patternability properties of SU-8 and tried to adjust the process for the fabrication of MEMS, tuning the exposure to UV radiation for patterning the microstructures with a size of 60 μm. As main results, it was found that: a) the resonant frequency response of the resulting piezoelectric MEMS devices depends on the stiffness of structural materials that in turn is related to ZnO loading; b) the piezoelectric coefficients of ZnO NPs ranged between 15 and 23 pm V^{-1}, which are the highest values for this material ever reported.

Then, the combination of cellulose nanocrystals and zinc oxide (ZnO) nanostructures has been considered as a promising way for the fabrication of self-powered nanogenerators. In particular, Li and co-workers [74] described a simple and efficient method to fabricate branched hierarchical flower-like nanostructures of ZnO on natural cotton fibers by combining electrospinning and the low-temperature hydrothermal growth technique. This way, it was possible to demonstrate the compatibility between ZnO and the cellulosic material.

Pursuing this research, Kumar et al. [75] prepared and characterized nanocomposite films made of ZnO nanorods, obtained by means of solvothermal and hydrothermal methods, homogeneously grown on a common paper matrix. The obtained flexible devices, which can be fabricated over large areas, were able to produce high output voltages (up to 80 mV) and power (50 nW cm^{-2}).

1.3. Aim of the work

The main aim of this work is the development of novel flexible, efficient, versatile piezoelectric films of easy fabrication and low impact, which could lead to a real competition in the field of renewable/alternative energy

technologies. Among the large variety of solutions, we decided to prepare UV-cured composites composed by an acrylic resin filled with different shaped ZnO, synthesized on the purpose, and/or cellulose (pristine form: nanocrystals). The use of a UV curable system has considered as particularly suitable for the implementation of new smart composites thanks to its rapid cure and wide range of properties [76]. In fact, UV-curing represents a more economic, faster method than the other curing processes. The UV-cured systems, in particular those based on acrylic resins, show flexibility, ease of processing large areas, simple integration into devices, reduction of device size, improved device reliability, and lower production costs, notwithstanding high conversions of the reactive functional groups upon exposure to the UV radiation [77]. Besides, the novelty of the present work refers to the selection of different ZnO shapes, which could provide different piezoelectric responses according to their morphologies. In literature, a comparison among them has not been reported yet.

First, the synthesis of different shaped ZnO and the preparation of UV cured composites films is detailed in Chapter 2, section 2.1; the characterization methods are described in Chapter 2, section 2.2. All the results and discussion are reported and discussed in Chapter 3: this chapter is divided into five sections. In section 3.1, the characterization of the starting materials in term of structure and morphology is reported. Section 3.2 discusses the curing process of the UV-curable resin, demonstrating that the adopted experimental conditions are able to complete the double bonds conversion, hence ensuring the obtainment of stable systems. Besides, in the same section, the structural characterization and morphological analysis of the different shaped ZnO fillers and of cellulose, before and after being incorporated into the resin, are presented. In section 3.3, the thermal properties of the designed systems are thoroughly investigated by means of thermogravimetric (TG) and Differential scanning calorimetry (DSC) analyses. Section 3.4 is fully dedicated to the dynamic-mechanical (DMTA) characterization of the prepared composite films and section 3.5 to the piezoelectric property assessment. The measurement systems for the determination of the piezoelectric characteristics have been set up both at the Institute of Metrological Research (INRIM) of Torino (Italy)

and at the Institute of Microelectronics and Microsystems (IMM) of the National Research Council (CNR) in Lecce (Italy). Finally, Chapter 5 highlights the main results obtained and discusses some possible perspectives for the future work.

The great challenge is to retain piezoelectric properties in the composites, even using very low filler loadings, without significantly changing the overall properties of the host polymer matrix. To the best of our knowledge, the piezoelectric response of such UV–curable polymer systems containing different shaped ZnO and/or cellulose has not been reported in the literature yet.

Therefore, the proposed study could open a new field of investigation in energy harvesting and remarkably widen the choice of composite materials and devices suitable for advanced applications.

Experimental Part

Chapter 2

Materials and methods

2.1. Materials

Zinc oxide samples were prepared through wet chemistry processes obtaining powders in different forms shaped like nano-particles (ZNP), bipyramidal morphologies (ZBP), flower-like morphologies (ZNF) and long needles (ZLN). Cellulose Nanocrystals obtained by freeze-drying were purchased by CelluloseLab (Canada). The UV-curable resin was a commercially bis-phenol A ethoxylate diacrylate (Ebecryl 150, hereinafter coded as EB), kindly supplied by Cytec Industries BV (Netherlands). 2,2-dimethyl-2-hydroxy acetophenone (Irgacure 1173) from BASF (Italy) was used as photoinitiator.

2.1.1. Synthesis of ZnO nanostructures

The synthesis of all ZnO with different nanomorphologies (ZNP, ZBP, ZFL and ZLN) was performed by means of sol-gel method. Several works in the scientific literature report on the synthesis of different shaped ZnO nanoparticles [46-52]. However, the peculiarity in this work is that our methodology represents a facile pathway for obtaining different shaped ZnO morphologies, using a common basic approach. In particular it is possible:

1) to start from the same precursor, namely zinc nitrate hexahydrate ($Zn(NO_3)_2 \bullet 6H_2O$, ≥99.0 %, Sigma-Aldrich),

2) to dissolve the precursor in water with a final concentration of 0.05 M,

3) to use a weak base (ammonia solution, from ammonium hydroxide (28%, Carlo Erba Reagents, Italy)) to catalyzed the hydrolysis,

4) to perform the processes at low temperatures.

Nanoparticles ZNP and Bipyramids ZBP were prepared by adding, under continuous mechanical stirring, the proper amount of ammonium hydroxide to 0.05 M aqueous solution of $Zn(NO_3)_2 \bullet 6H_2O$ and adjusting the solution pH to 10. By ageing the solution at room temperature for 1 h or 24 h, ZNP and ZPB precipitates were obtained, respectively. They were filtered by gravity

filtration (by using cellulose filters with pore size of 1 µm), washed several times with deionized water and diethyl ether (Aldrich, USA), dried at 100 °C overnight and then calcinated at 400 °C for 2 h for obtaining ZNP and ZBP. The synthesis yields were in the range 95-97%.

Long needles ZLN were obtained by following the ZNP preparation, but treating the mixture at 95 °C for about 7 h. The precipitate was filtered by gravity filtration (by using cellulose filters with pore size of 1 µm), washed several times with deionized water and diethyl ether (Aldrich, USA) and dried at 100 °C overnight. The synthesis yields were in the range 95-97%.

Flowers ZNF - Flower-like powders were prepared through direct precipitation of ZnO starting from the same reagents with the same molar concentrations as in the nanoparticle synthesis, but maintaining the temperature for the hydrolysis step at 60 °C. The precipitate was then filtered by gravity filtration (by using cellulose filters with pore size of 1 µm), washed several times with deionized water and diethyl ether (Aldrich, USA) and dried at 100 °C overnight. The synthesis yields were in the range 77-80%.

Figure 2.1 reports a schematic representation of the synthesis of the different ZnO morphologies.

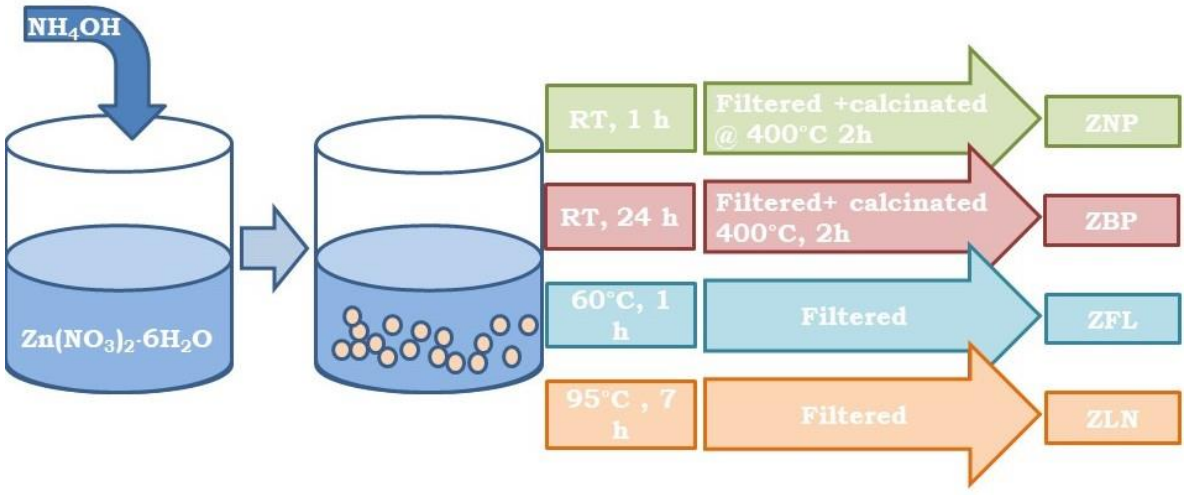

Figure 2.1. Schematic representation of nanostructured ZnO synthesis., ZNP= ZnO nanoparticles, ZBP= ZnO bipyramidal morphologies, ZNF= ZnO flower-like and ZLN= ZnO long needle morphologies.

2.1.2. Preparation of the nanocomposite films

4% wt. of photoinitiator (Irgacure 1173) was added to the acrylic UV-curable resin; then, cellulose, ZnO fillers or a mixture of them in equal amount were dispersed into the resin and ultrasonicated for 30 min at room temperature. Cellulose and ZnO were dried before mixing in a vacuum oven for 24 hours at 80°C. Furthermore, cellulose was grinded in order to reduce its size, using two different techniques. The first exploited a standard ceramic mortar, where cellulose was grinded manually for 10 min. Conversely, for the second technique, a home-made ball milling unit (Figure 2.2), similar to those conventionally employed for metals or ceramics, was employed, working at 30 rpm for 1h.

The resulting dispersions were coated on glass slides, using a wire wound applicator and then exposed to the UV radiation provided by a F300 S apparatus (Heraeus Noblelight, USA) working in static conditions.

Figure 2.2. Home-made ball milling unit developed at the Energy Department of the Politecnico di Torino and used for grinding cellulose.

The radiation intensity on the sample surface, measured with an UV-meter, was about 800 mW/cm^2; two not consecutive exposures of 15 s were enough for completing the photopolymerization reaction, also in the presence of the different fillers. The obtained UV-cured films were peeled off from the glass slides and used for the different characterizations and for the fabrication of cantilevers for piezoelectric tests. Films 150 μm thick were obtained. Table 2.1.1 lists the prepared samples together with their code and composition.

Table 2.1.1. Codes and composition of the prepared composite films.

Sample code	EB150 (wt.%)	ZnO (wt.%)	Cellulose (wt.%)
Composite films containing different ZnO morphologies			
EB	100	-	-
EB-ZNF 4	96	4	-
EB-ZLN 4	96	4	-
EB-ZBP 4	96	4	-
EB-ZNP 4	96	4	-
EB-ZNF 10	90	10	-
EB-ZNF20	80	20	-
Composite films containing cellulose grinded in a mortar (C)			
EB-C 4	96	-	4
EB-C 10	90	-	10
Composite films containing ball milled cellulose (BMC)			
EB-BMC 2	98	-	2
EB-BMC 4	96	-	4
EB-BMC 10	90	-	10
Composite films containing grinded cellulose (C) and different ZnO morphologies			
EB-C-ZFL 4 (2-2)	96	2	2
EB-C-ZLN 4 (2-2)	96	2	2
Composite films containing ball milled cellulose (BMC) and different ZnO morphologies			
EB-BMC-ZFL 4 (2-2)	96	2	2
EB-BMC-ZFL 10 (5-5)	90	5	5
EB-BMC-ZLN 4 (2-2)	96	2	2
EB-BMC-ZLN 10 (5-5)	90	5	5

2.2. Characterization techniques

2.2.1. Fourier transform infrared (FTIR)-attenuated total reflection (ATR) spectroscopy

FTIR-ATR spectra of the obtained films were recorded using a Perkin-Elmer FTIR spectrometer (model Paragon 500 equipment) with the aim to assess the completeness of the photopolymerization process. The spectra (32 scans) were recorded between 4000 and 400 cm^{-1} wavelength range and 4 cm^{-1} resolution.

2.2.2. Scanning Electron Microscopy (SEM)

The morphology of ZnO powders was investigated by field emission scanning electron microscopy (FE-SEM), using a Carl Zeiss Sigma microscope equipped with a Schottky field-emitter (tip made of <100> tungsten crystal and a ZrO_2 reservoir). Besides, a scanning electron microscope (SEM Zeiss Evo 50 XVP

with LaB6 source) was employed for analyzing either the cellulose powder or the surface and cross-section of the composite films. To this aim, the samples were fractured in liquid nitrogen and then gold-metallized using a E5 150 SEM coating unit.

2.2.3. Wide Angle X-ray Diffraction (WAXD)

Wide Angle X-ray Diffraction was carried out by using a Philips PW 1830 vertical diffractometer with Bregg–Brentano geometry (Cu K_α radiation, 40 kV, 30 mA). Diffraction patterns of ZnO were collected over the range 2θ=10–120°, with steps of 0.02° and 10 s of dwell time. The XRD data were elaborated using a Rietveld analysis program FullProf (release 2011) [78,79]. The crystallite size was estimated according to the Scherrer formula (equation 1) [80]:

$$L = \frac{k \cdot \lambda}{\beta cos\theta} \quad (1)$$

where λ is the wavelength of X-ray radiation, k is the dimensionless constant taken as 0.9, β is the full width at half maximum height and θ is the diffraction angle. Diffraction patterns of cellulose and of the composites were collected in the same condition as the previous ones, over the range 2θ=10–40° and 2θ=10-60°, respectively. The crystallinity index of cellulose was measured using the empirical method described by Segal et al. (equation 2) [81]:

$$\chi = \frac{I_{200} - I_{am}}{I_{200}} \cdot 100 \quad (2)$$

where I_{200} is the maximum intensity of the principal diffraction peak (200) (at 2θ=22.6° for cellulose I, and at 2θ=21.7° for cellulose II), and I_{am} is the intensity minimum between the peaks at 200 and 110 (at about 18°). This method does not resolve the absolute value of the crystallinity index of the material, but it is convenient for comparative purposes.

2.2.4. Differential scanning calorimetry

The thermal behavior of the composite films was assessed by using a Mettler DSC-822 apparatus. DSC analyses were carried out according to the following cycle: (1) heating up from 0 °C to 160 °C at 10 °C/min; (2) cooling down to 0

°C at 10 °C/min; and (3) heating up from 0 °C to 160 °C at 10 °C/min. The glass transition temperature (T_g) was taken at the midpoint of heat capacity changes. Calibration was performed using indium as standard (T_m = 156.4 °C; ΔH_m = 28.15 J/g).

2.2.5. Thermogravimetric analyses

Thermogravimetric (TG) analyses were performed both in nitrogen and air, from 30 to 800 °C with a heating rate of 10 °C/min, using a TA Q500 thermo balance (TA Instruments) (experimental error: ± 0.5% wt., ±1 °C). The samples (ca. 20 mg) were placed in open alumina pans and fluxed with nitrogen or air (gas flow: 60 ml/ min). $T_{10\%}$ (temperature, at which 10% weight loss occurs) and T_{max} (temperature, at which maximum weight loss rate is achieved) were evaluated, as well as the residues at T_{max} and at the end of the tests.

2.2.6. Dynamic-mechanical analyses

Dynamic-mechanical (DMTA) analyses were performed using a DMA Q800 (TA Instruments) in tensile configuration on all the composite films. The following experimental conditions were adopted: temperature range from 25 to 120 °C, heating rate of 3 °C/min, 1 Hz frequency and 0.05% of oscillation amplitude in strain-controlled mode. Storage modulus (E'), loss modulus (E") and tanδ curve were recorded. T_g values were calculated from the peak value of tanδ curve. For each formulation, the tests were repeated three times and the experimental error was calculated as standard deviation for all the measured parameters.

2.2.7. Piezoelectric measurement setup

Different cantilevers of about 10×10 mm^2 were fabricated employing the UV-cured nanocomposite films as active material. A gold film having a final thickness of about 80 nm, working as electrode to collect the generated charges, was deposited on both sides by RF sputtering in Ar atmosphere (deposition pressure: 2.5 × 10^{-2} mbar), applying an RF power of 150W on an Al target. The electrodes thickness represents a good trade-off between the mechanical reliability of the electrical contact and the limited stiffness induced

on the resin resonant beam (that also affects the resonance frequency). After the deposition, coated resin substrates were slowly cooled down to room temperature and unloaded from sputtering tool. The samples, once positioned in the sample holder, had a free square surface of 1 cm^2 that was mechanically stressed to obtain the piezoelectric current generation (Figure 2.3). All the materials were tested at 150 Hz (chosen for typical environmental vibration energy harvesting applications) and at their resonance frequencies. The block diagram of the measurement system for the determination of the piezoelectric characteristics is shown in Figure 2.4. The sinusoidal excitation signal is generated by a programmable function generator (1) at the chosen frequencies between 0.1 and 4500 Hz.

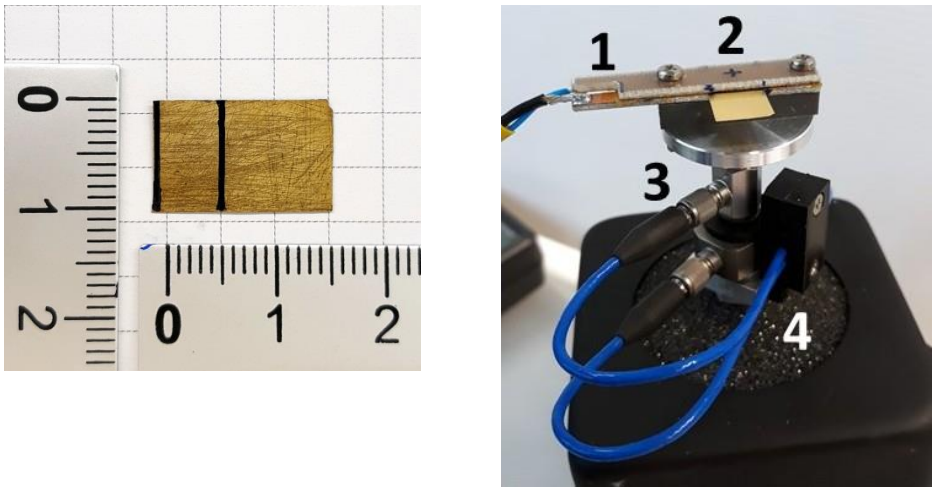

Figure 2.3. (Left) Sample of bare acrylic polymer (EB) after the gold metallisation process. The rectangular part on the left is clamped into the sample holder. (Right) View of the system used to clamp the sample under test (1, 2) and the two sensors (3, 4)

The generator is connected to an audio frequency amplifier (2), which drives the shaker actuator (3) with a power of about 15 W, enough to move the whole test group (4) consisting of the sample itself, the sample holder and the sensors, in the full frequency range needed. The original excitation signal is also fed both to CH 3 input of the oscilloscope (8) for monitoring and synchronization purpose and to the lock-in amplifier (7) as a reference signal for demodulation. CH 1 input of the oscilloscope is connected to the

accelerometer amplifier and conditions the signals from both the accelerometer and the force sensor for the correct measurement.

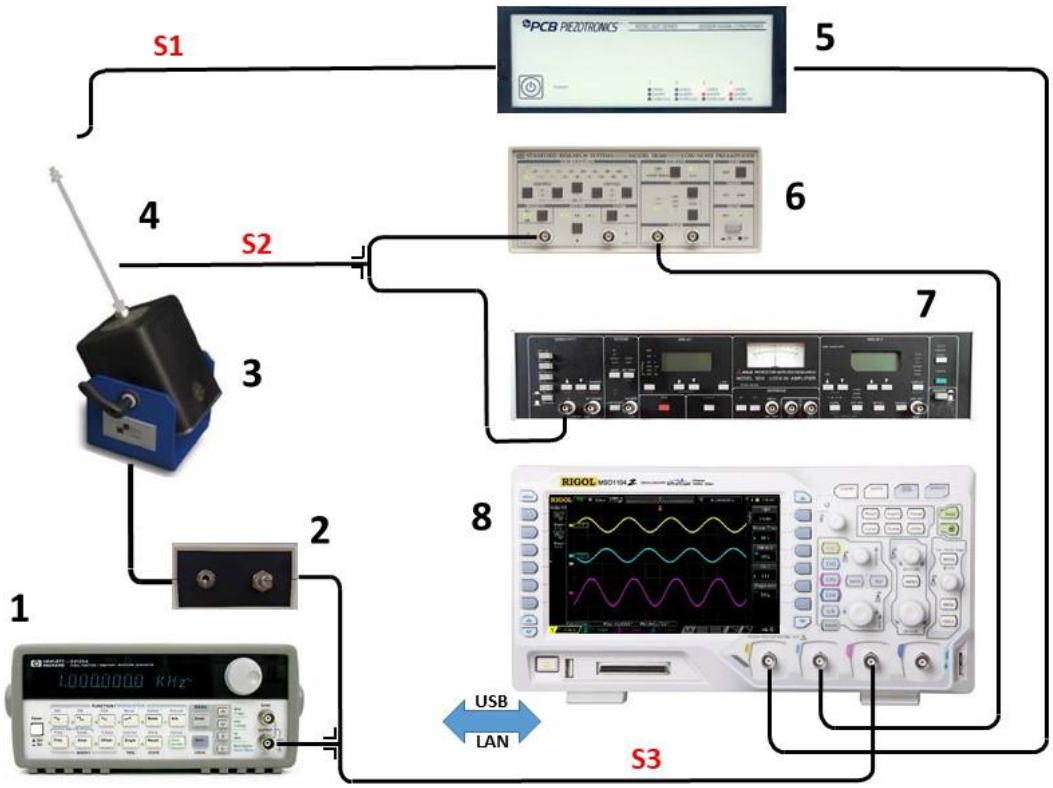

Figure 2.4. 1) Function generator; 2) Audio-frequency amplifier; 3) Shaker; 4) Detectors Head and sample holder; 5) Accelerometer amplifier; 6) Low noise amplifier; 7) Lock-in amplifier; 8) Oscilloscope.

The piezoelectric signal generated by the polymeric sample is then collected by the conductive paint and connected, through a coaxial cable, to a low noise amplifier (6) equipped with a series of selectable input filters. The output of that amplifier is connected to CH 2 input of the oscilloscope. The characterization with respect to humidity and pressure is carried out at a constant temperature using a commercial air-bath. The tests can be carried out between 15 and 30 ° C.

The piezoelectric charge constant d_{33} was measured with a d_{33} meter (Piezotest, PM200) depicted in Figure 2.5.

Figure 2.5. Piezotest PM200 employed for the calculation of d33 values of the analyzed samples.

This system works by applying a low frequency force to the sample under test clamped between two jars. The electrical signals acquired by the sample under test are compared with a built-in reference and processed to give a direct reading of the d_{33} coefficient, which indicates the charge per unit force in the polarization direction. The operation method is called "quasi-static" or "Berlincourt" method [82]. The tests were performed at a fixed frequency of 110 Hz and dynamic force of 0.25 N.

Chapter 3

Results and discussion

3.1. Morphological and structural analysis of ZnO powders and cellulose

3.1.1. Morphological analysis of ZnO powders

The typical SEM micrographs of the different ZnO morphologies are shown in Figure 3.1.1; several magnifications are reported in order to highlight the features of each different morphology. ZNP (Figure 3.1.1. A) shows spherical nanoparticles, whose sizes are about 50–60 nm, while ZBP and ZNF samples appear as nanoparticle aggregates in form of bipyramidal and flower-like morphologies, as observable in Fig. 3.1. B and D respectively. In particular, the bipyramidal morphologies (Figure 3.1.1. B and C) show the z-axis of about 10 μm and a fine morphology made of roundish nanoparticles, whose sizes are heterogeneous and are only slightly lower than those of ZNP counterparts. A similar hierarchical morphology appears in ZNF powders (Figure 3.1.1. D and E), where particles of about 30 nm in size are assembled in 1 μm size. Fig. 3.1. F and G show the typical SEM images of ZLN particles consisting of bi-dimensional nanocrystals shaped as long needles (about 100 nm wide and 7–8 μm long).

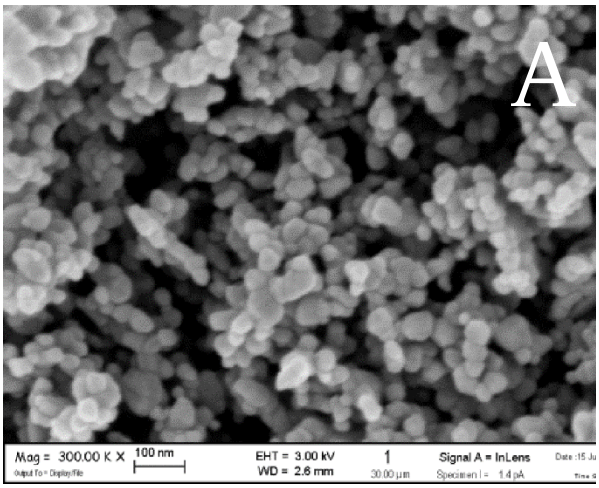
A
Mag = 300.00 K X
100 nm
EHT = 3.00 kV
WD = 2.6 mm
Signal A = InLens

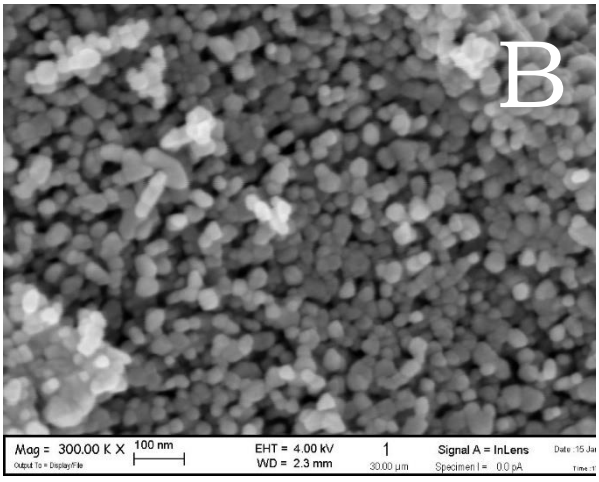
B
Mag = 300.00 K X
100 nm
EHT = 4.00 kV
WD = 2.3 mm
Signal A = InLens

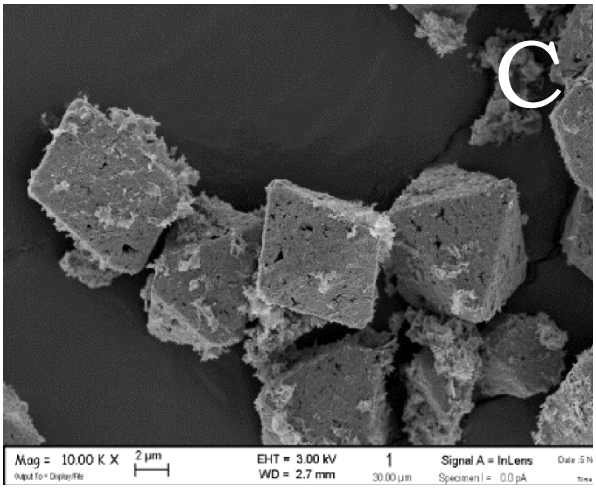
C
Mag = 10.00 K X
2 µm
EHT = 3.00 kV
WD = 2.7 mm
Signal A = InLens

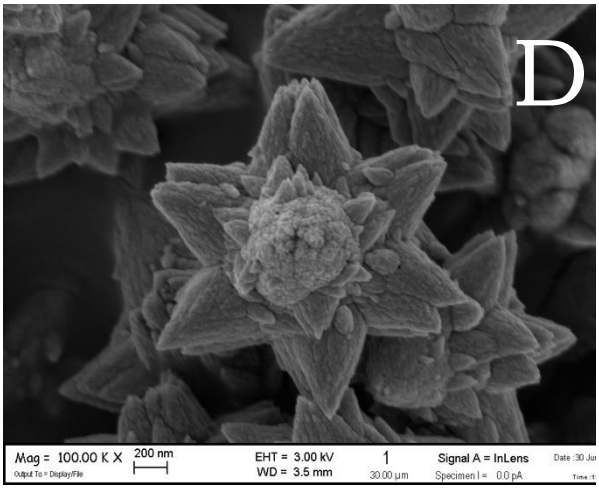
D
Mag = 100.00 K X
200 nm
EHT = 3.00 kV
WD = 3.5 mm
Signal A = InLens

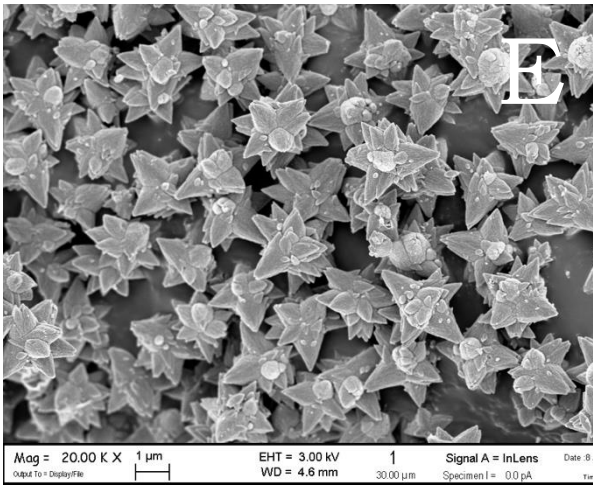
E
Mag = 20.00 K X
1 µm
EHT = 3.00 kV
WD = 4.6 mm
Signal A = InLens

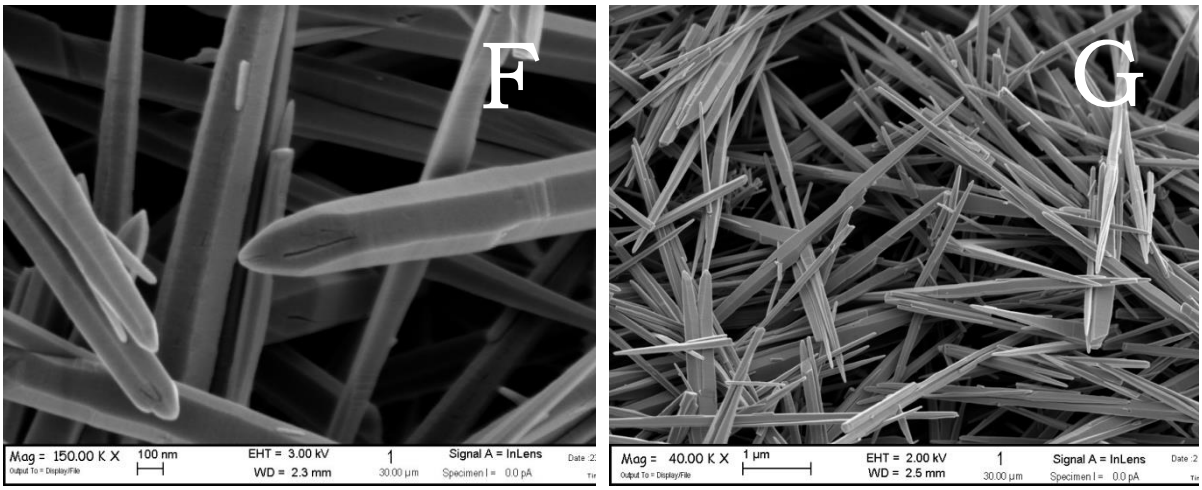

Figure 3.1.1. SEM micrographs of ZnO morphologies: (A) nanoparticles, (B and C) bipyramidal morphologies, (D and E) nanoflowers and (f and G) long needles.

3.1.2. Morphological analysis of cellulose nanocrystals

The commercial cellulose has been obtained by freeze-drying and it falls in to the category of nanocellulose (e.g. cellulose nanocrystals -CNC). However, it appears composed of very big sheets of different size as evidenced in the picture and in the SEM micrograph shown in Figure 3.1.2. For this reason, cellulose was grinded with a mortar or a ball milling unit, as already described in chapter 2. SEM micrographs of grinded and ball milled cellulose are presented in Figure 3.1.3: they clearly indicate that the used techniques reduce the pristine average size of cellulose. In particular, ball milling is more effective, as it is able to produce smaller cellulose powders. Considering that in this work the cellulose shows micrometric dimensions, it will not be indicated as CNC (as by the producer), but simply as cellulose.

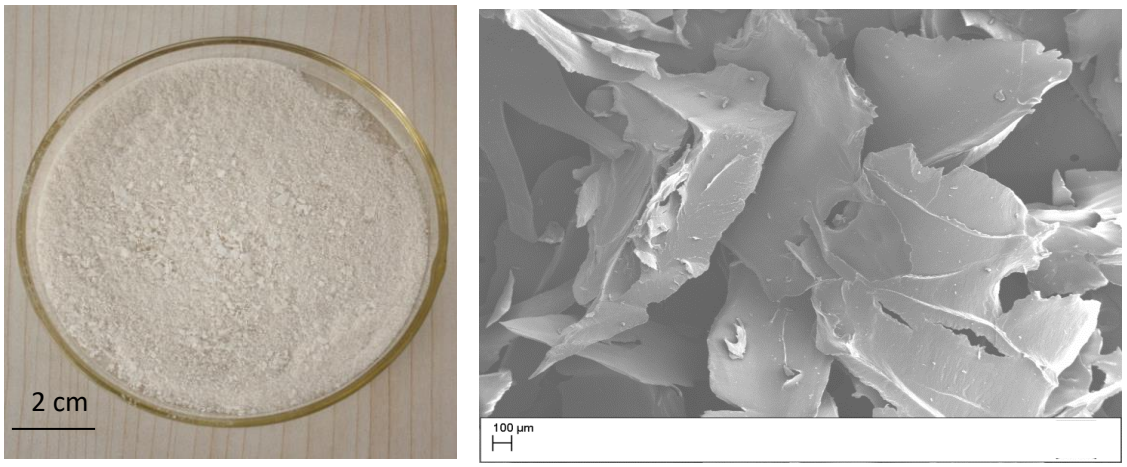

Figure 3.1.2. (Left) Picture and (right) SEM micrograph of as purchased cellulose.

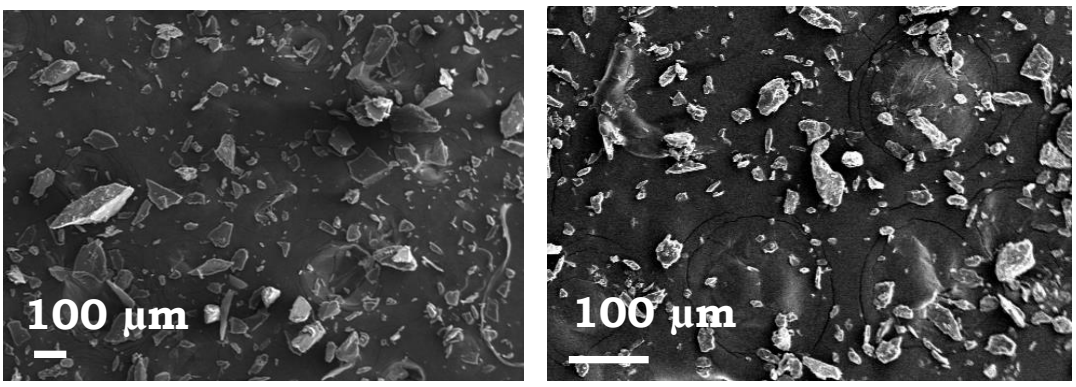

Figure 3.1.3. SEM micrograph of (A) grinded cellulose and (B) ball milled cellulose.

3.1.3 WAXD analysis of ZnO nanostructures and cellulose

According to the WAXD patterns shown in Figure 3.1.4, all the synthesized nanostructures exhibit a hexagonal wurtzite structure (space group P63mc), irrespective of both the synthesis process and the morphology. XRD spectra show the typical peaks (at 2θ values of 31.9, 34.5, 36.3, 56.7 and 62.9°) for the zinc oxide when synthesized in a nanostructured form [83].

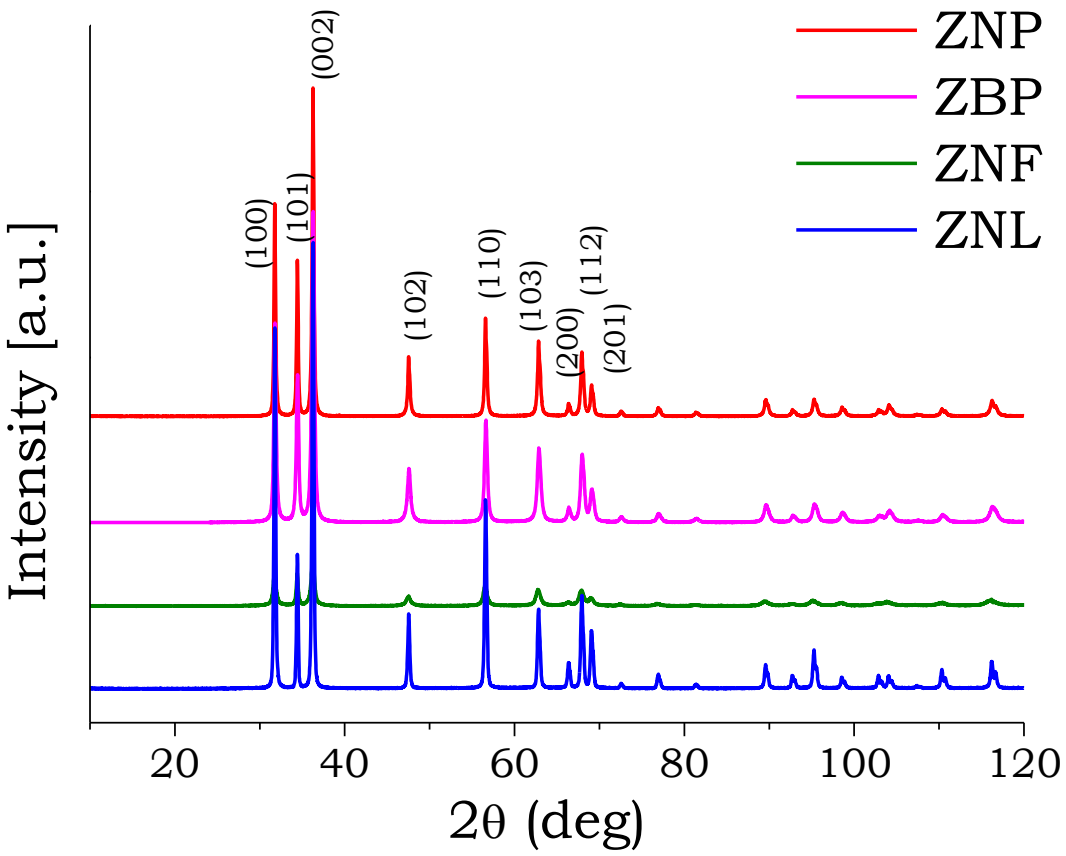

Figure 3.1.4. WAXD patterns of ZnO nanostructures.

The crystallite sizes, evaluated by the Scherrer formula, highlight significant differences: in particular, the values calculated on the (101) diffraction peaks for ZNP, ZBP, ZNF and ZLN powders were 28, 24, 30 and 39 nm, respectively. The dimensions and crystallite sizes of the different ZnO morphologies are collected in Table 3.1.1.

Figure 3.1.5 shows the diffraction patterns of commercial, grinded and ball milled cellulose. The curves have been corrected for the background signal and normalized to the most intense peak of the spectra (i.e. 2001 & 0202 centered at about 22.3°).

Table 3.1.1. Dimensions and crystallite sizes of different ZnO morphologies

Code	Morphology	Dimensions[a]	Crystallite size[b] (nm)
ZNP	nanoparticles	50-60 nm	28
ZBP	bipyramidal nanoaggregates	10 μm (z axis)	24
ZNF	flower-like morphologies	1 μm (diameter)	30
ZLN	long needles	100 nm (width) 7-8 μm (length)	39

[a] measured by SEM images, [b] measured by WAXD

It is well known that cellulose nanocrystals include two polymorphs, namely cellulose I and II [84,85]. The peaks at 2θ = 12.2° and 19.7° shown in Figure 3.1.5 are assigned to -110 and 110 crystalline planes of cellulose II [86]. Peaks at 2θ = 14.7° and 16.5° are due to the diffraction of the -110 and 110 crystalline planes of cellulose I [86]. The 200 (at 2θ = 22.3°) and 004 (at 2θ = 34.5°) reflections belong to cellulose I and overlap with the 020 and 040 reflections of cellulose II. The spectra in Figure 3.1.5 clearly indicate that the cellulose used in this work is a mixture of the two forms. Besides, the grinding and ball milling processes do not induce any phase transformation as sometimes reported in literature [87]: in the normalized curves of grinded and ball milled cellulose, there is not the same variation (positive or negative) of the peak intensity relative to form I as regards to that of form II. This means that the two processes have only modified the preferential orientation of some crystallographic planes with respect to others.

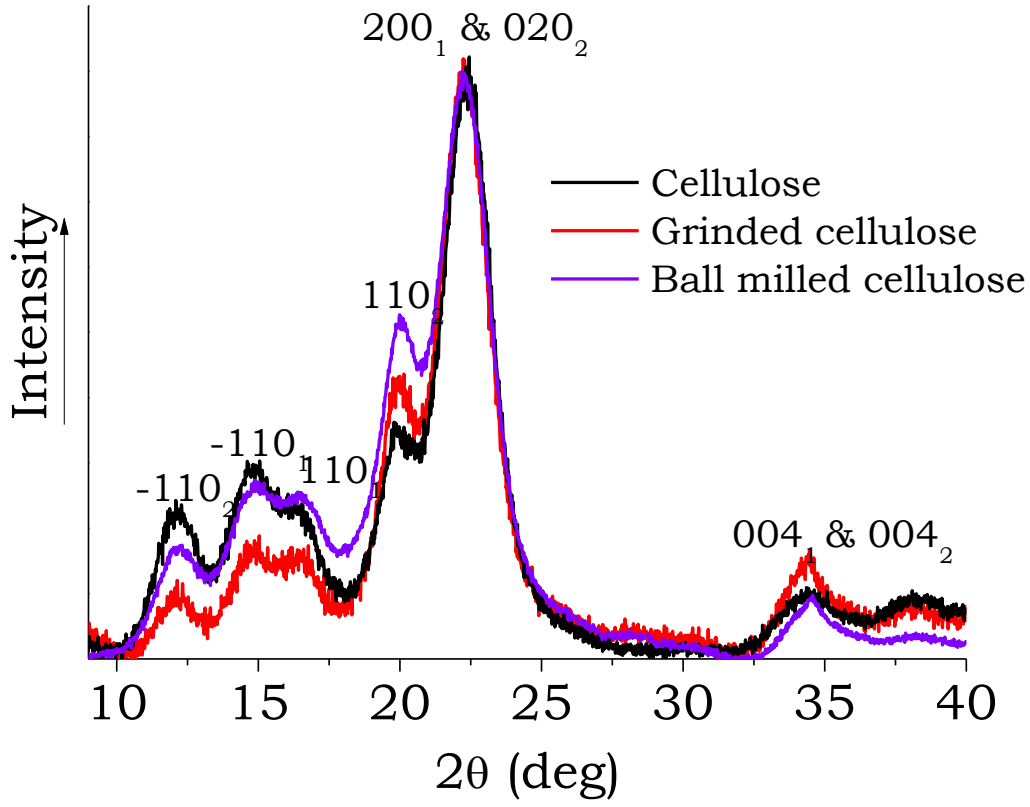

Figure 3.1.5. WAXD pattern of as obtained, grinded and ball milled cellulose

The crystallinity index (χ) of the cellulose was measured according to equation 2 (Segal equation, Chapter 2). This method for calculating the crystallinity index provides reliable relative crystallinity for comparison purposes, as it assumes that the amount of the crystalline region is represented by the intensity of the highest diffraction peak and the amount of amorphous region is represented by the minimum intensity between the 200_1 & 020_2 peaks and 110_2. Though other methods, reported in literature, are more realistic [88], the Segal approach is very straightforward and quick to use. The crystallinity index of cellulose found by following the Segal method is 91% for the as obtained cellulose, 90% for the grinded cellulose, 82% for the ball milled cellulose. The decrease in crystallinity due to the mechanical treatment is well documented in literature [89].

3.2. Structural and morphological characterization of composites

3.2.1. FTIR-ATR spectroscopy for studying the curing process of composites

Ebecryl 150 is a commercially available acrylate with a high reactivity, especially in combination with suitable photoinitiators. It is well known that the UV-curing of acrylate systems occurs at R.T., providing the system with the ultimate achievable cross-linking density, i.e. with the maximum conversion of the double bonds [83,90]. However, in order to assess whether the adopted experimental conditions employed for the photocuring process were suitable for achieving the completeness of the double bonds conversion, Attenuated Total Reflectance-Fourier Transform Infrared spectroscopy (ATR-FTIR) was employed. As an example, Figure 3.2.1 shows the typical spectra, in the range between 1800 and 1550 cm^{-1}, for the systems containing ZLN and ZFL morphologies (ZFL in different amount), immediately before and after 30 minutes from the exposure to the UV radiation. In all cases, the complete disappearance of the band at 1635 cm^{-1} is evident, indicating that all the acrylic double bonds [91] have participated in the curing reaction. This finding, as reported in the next chapter, was further supported by the absence of exothermal peaks in the first heating up traces of DSC thermograms.

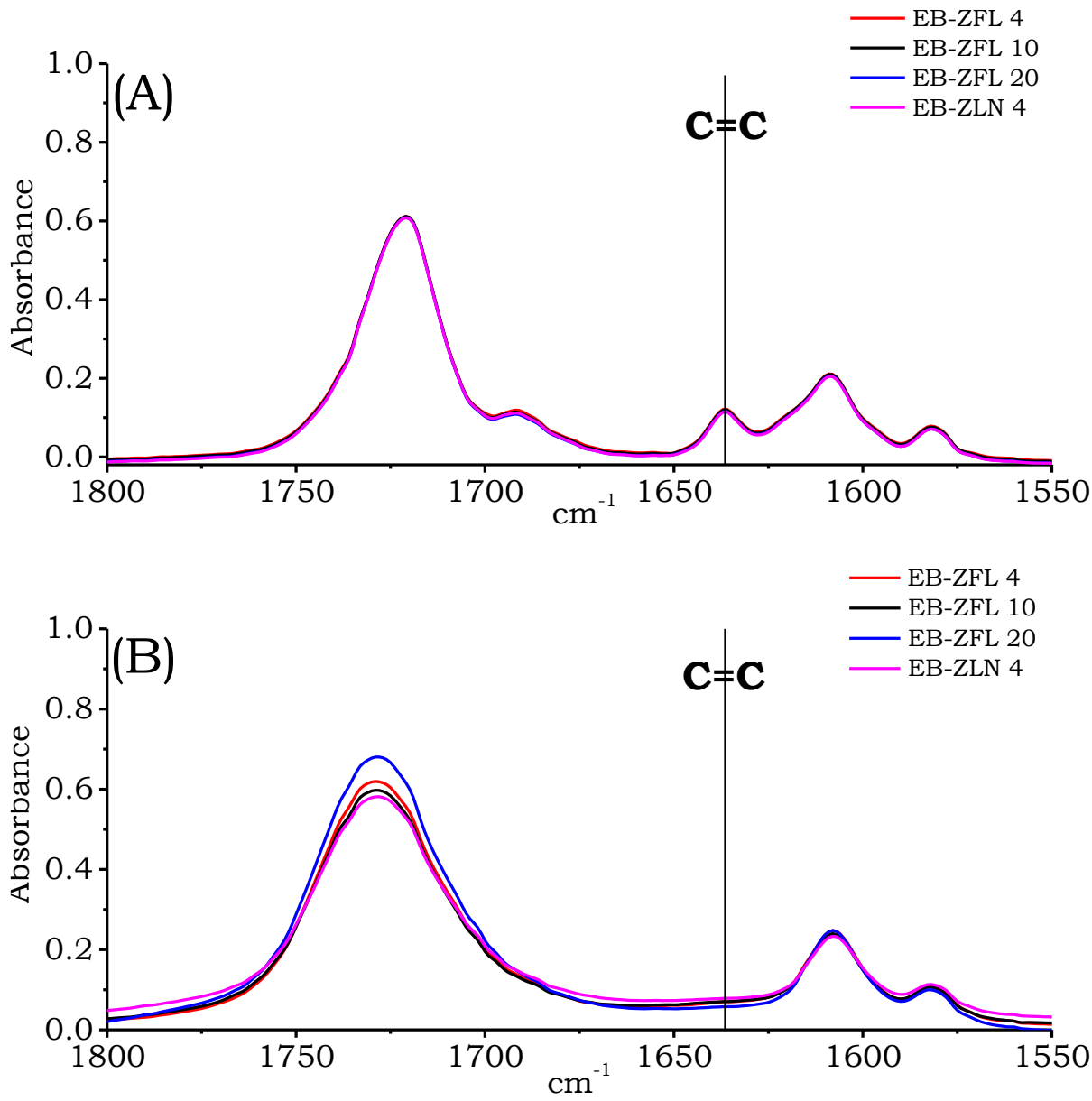

Figure 3.2.1. FTIR-ATR spectra of EB-ZnO composites, before (A) and after (B) exposure to the UV radiation. The absence of the band at about 1635 cm^{-1} after the exposure to UV radiation is a clear indication of the completeness of the UV curing process.

3.2.2. Morphological analysis of ZnO composites, cellulose composites and ZnO+cellulose composites

SEM micrographs of cryogenically fractured surfaces for ZnO, cellulose and ZnO+cellulose composites are shown in Figure 3.2.2, 3.2.3 and 3.2.4, respectively. Different magnifications are reported in order to evidence the features of each different morphology. Furthermore, in some cases, back scattered analysis was used in order to assess the filler distribution. The

fractured surface (Figure 3.2.2. A) of the cured acrylic matrix appears smooth and with characteristic features of brittle fracture. EB-ZNP surface (Figure 3.2.2. B) is characterized by heterogeneous dispersion of the filler within the matrix, with the formation of very big micrometric clusters. Though EB-ZBP (Figure 3.2.2. C) surface does not show aggregation of bipyramids, they appear not uniformly distributed within the polymer matrix and sometimes with a different shape. All these findings demonstrate that it was not possible to prepare films with uniform mechanical/piezoelectric behavior when ZNP or ZBP were incorporated: therefore, these fillers have not been considered for the preparation of further composites.

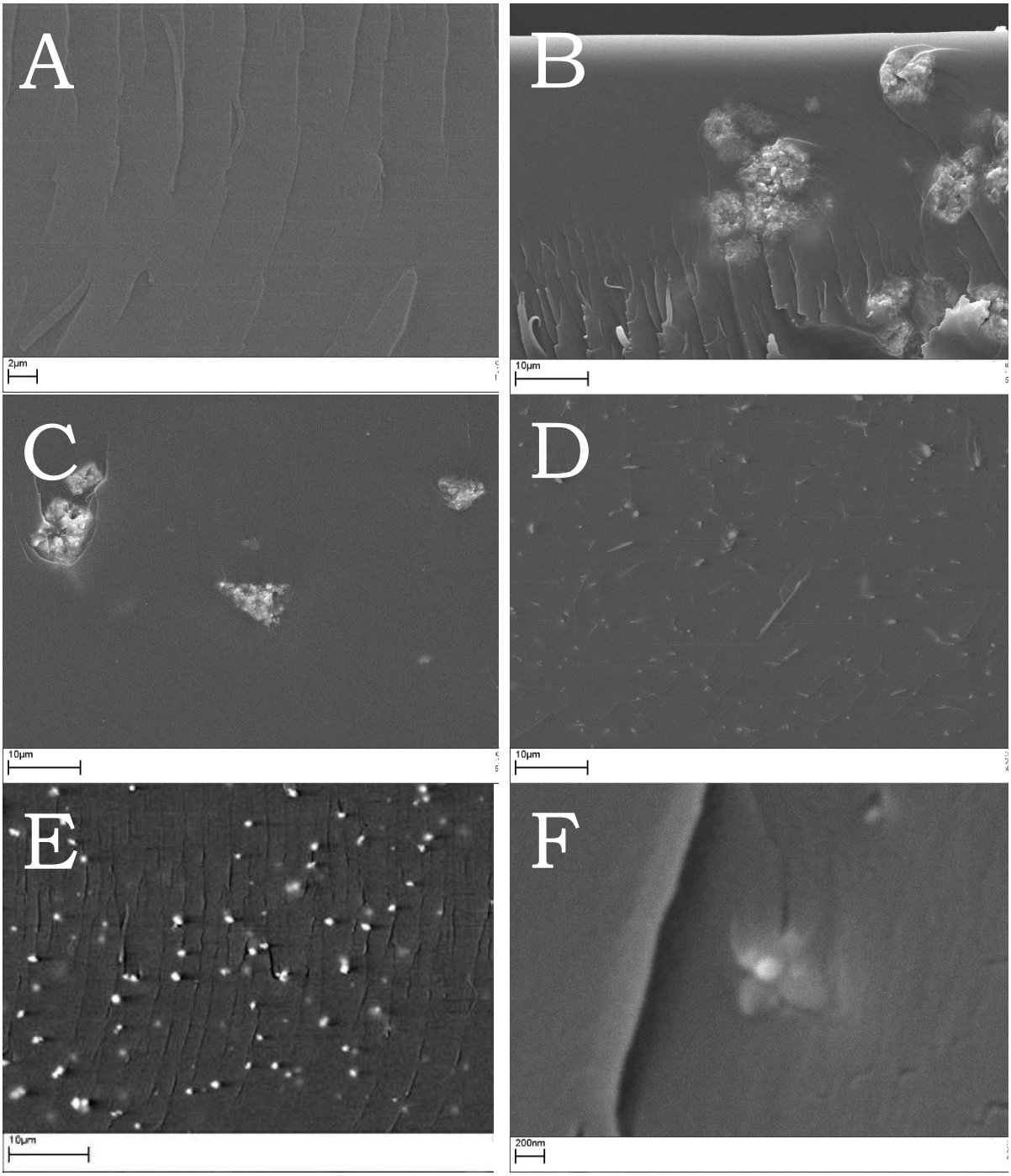

Figure 3.2.2. SEM micrographs of ZnO composites: (A) neat EB, (B) EB-ZNP 4, (C) EB-ZBP 4, (D) EB-ZLN 4, and (E and F) EB-ZFL 4. ZNP=nanoparticles, ZBP=bipyramidal morphology, ZLN=long niddle, ZFL= flower-like morphology.

Conversely, EB-ZLN and EB-ZNF surfaces (Figures 3.2.2. D and E, respectively) appear characterized by a uniform distribution and dispersion of the fillers within the polymer matrix. Only in few cases, small aggregates were

observed. Besides, ZLN and ZNF particles retain their shape, as shown in Figure 3.2.2. F for ZNF.

Figure 3.2.3 reports the typical SEM micrographs of EB-C 96-4 and 90-10 composites, for which cellulose was grinded in a mortar. It is noteworthy that the morphology of these composites is not homogeneous because of the presence at both compositions of domains of the pristine cellulose, having variable size, ranging from few to about 50 microns.

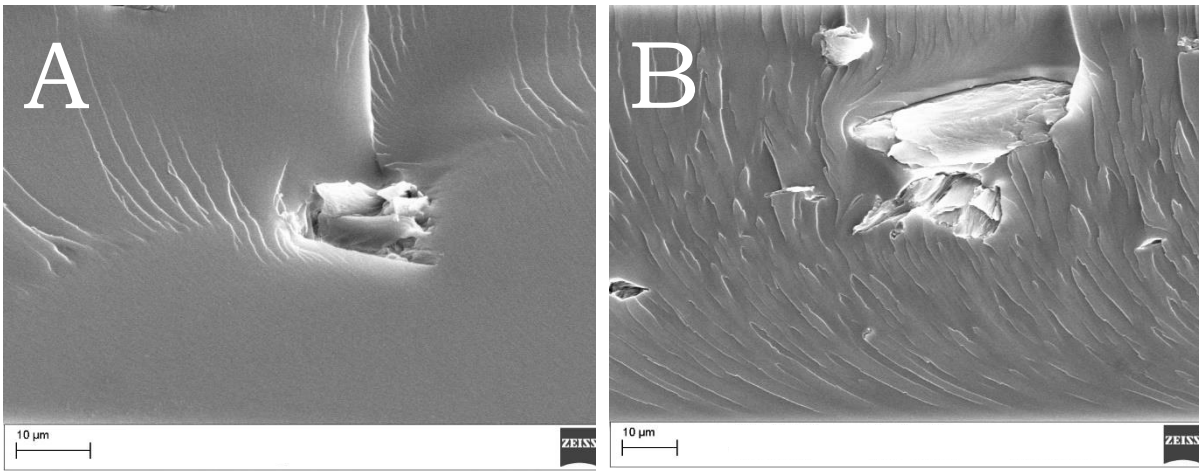

Figure 3.2.3. SEM micrographs of cellulose composites: (A) EB-C 4 and (B) EB-C 10. Before mixing, cellulose was grinded in a mortar. C= grinded cellulose.

Figure 3.2.4 shows the typical SEM micrographs of EB-C-ZnO. Cellulose, before using, was grinded in a mortar. ZnO particles (both ZFL and ZNL) are uniformly distributed in the polymer matrix and cellulose appears again as big domains still visible and/or pulled out during fracturing. The size of cellulose domains is similar to that found in EB-cellulose composites (i.e. from few to 50 microns).

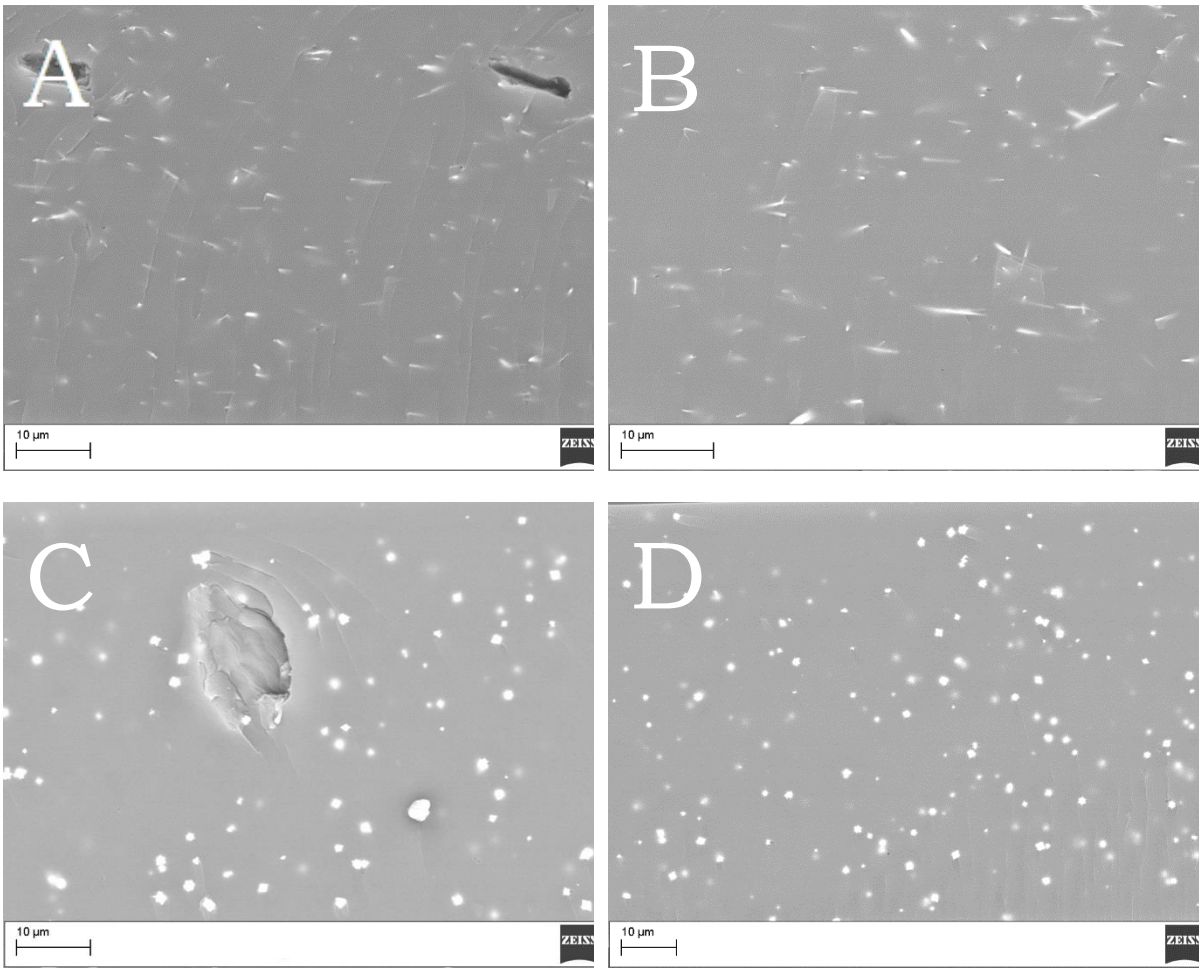

Figure 3.2.4. SEM micrographs of cellulose+ZnO composites: (A and B) EB-C-ZLN 4 and (C and D) EB-C-ZFL 4. Before mixing, cellulose hand as been grinded in a mortar. C= grinded cellulose.

In order to try to reduce the size of cellulose domains, ball milling was used (see Chapter 2). The SEM micrographs of fractured surfaces of EB-BMC, shown in Figure 3.2.5, clearly indicate that the process significantly reduced the size of the cellulose domains to few microns as evidenced by the red circles at any composition.

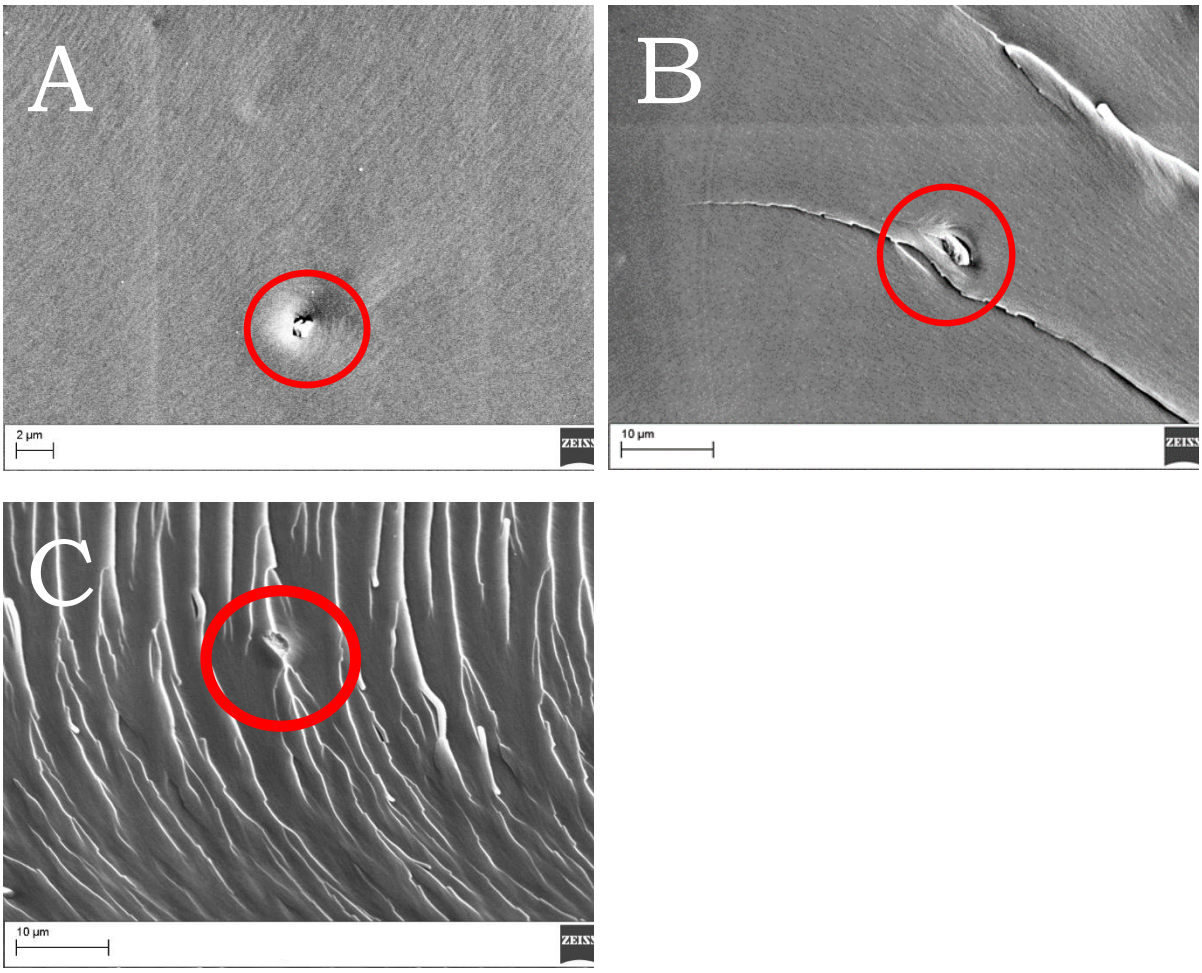

Figure 3.2.5. SEM micrographs of BM cellulose composites: (A) EB-BMC 2 (B) EB-BMC 4 and (C) EB-BMC 10. BMC = ball milled cellulose.

The typical SEM micrographs of EC-BMC-ZnO are presented in Figure 3.2.6. Again, ZnO particles (both ZFL and ZNL) are uniformly distributed in the polymer matrix and cellulose is likely to form domains still visible and/or pulled out during fracturing. The size of cellulose domains does not differ from that found in EB-BMC composites (i.e. <10 µm).

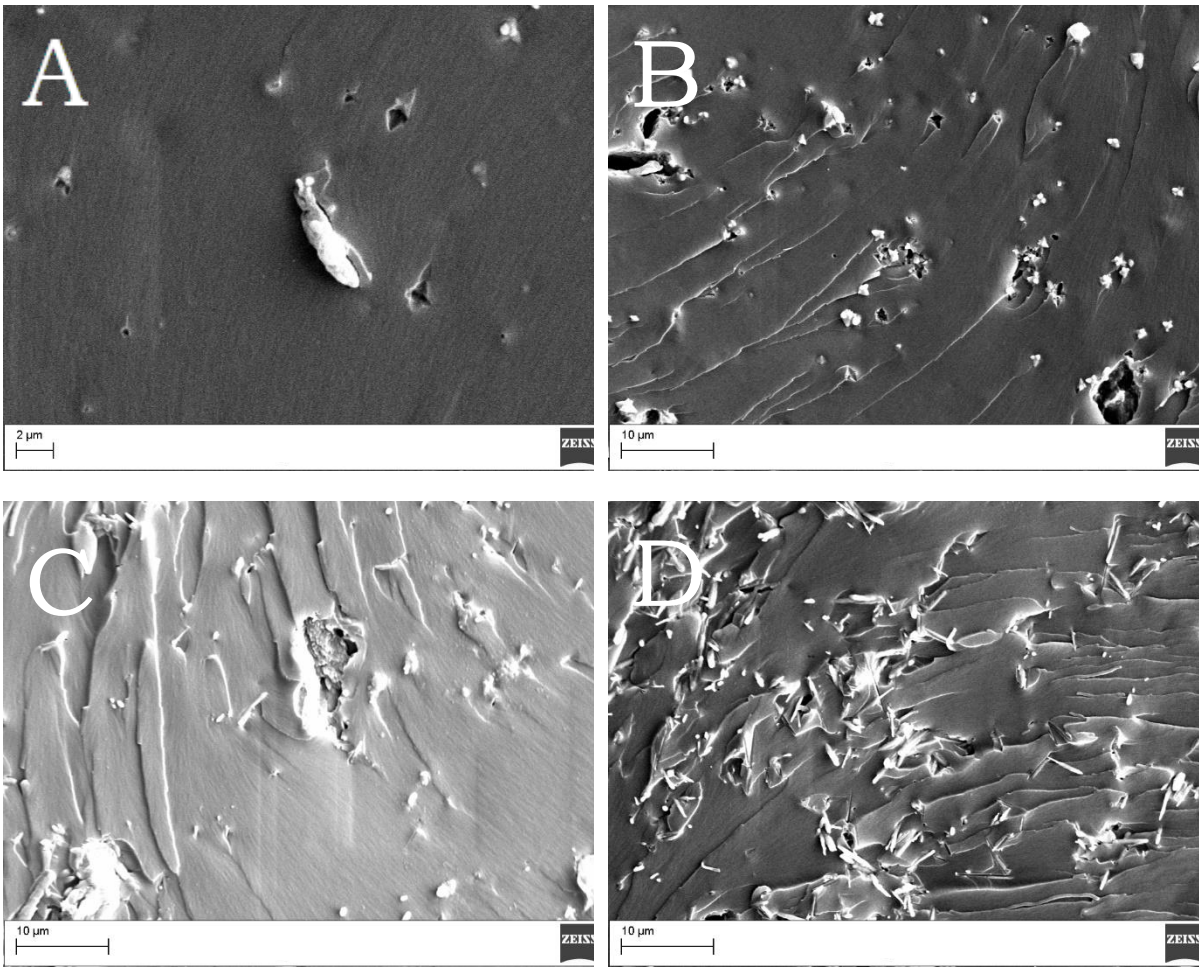

Figure 3.2.6 SEM micrographs of BMC+ ZnO composites: (A) EB-BMC-ZFL 4, (B) EB-BMC-ZFL 10, (C) EB-BMC-ZLN 4 and (D) EB-BMC-ZLN 10. BM cellulose = ball milled cellulose.

3.2.3. Morphological analysis of EB-ZnO surfaces

The piezoelectric response of composites, which will be discussed in section 3.5, could be interpreted in term of piezoelectric element density present on the surface of the film. For this reason, the SEM micrographs of ZFL composites surfaces, containing 4, 10 and 20 wt.% of filler are compared in Figure 3.2.7. It is clear that, independently from the analyzed morphology, all the composites surfaces show a good distribution of piezoelectric filler.

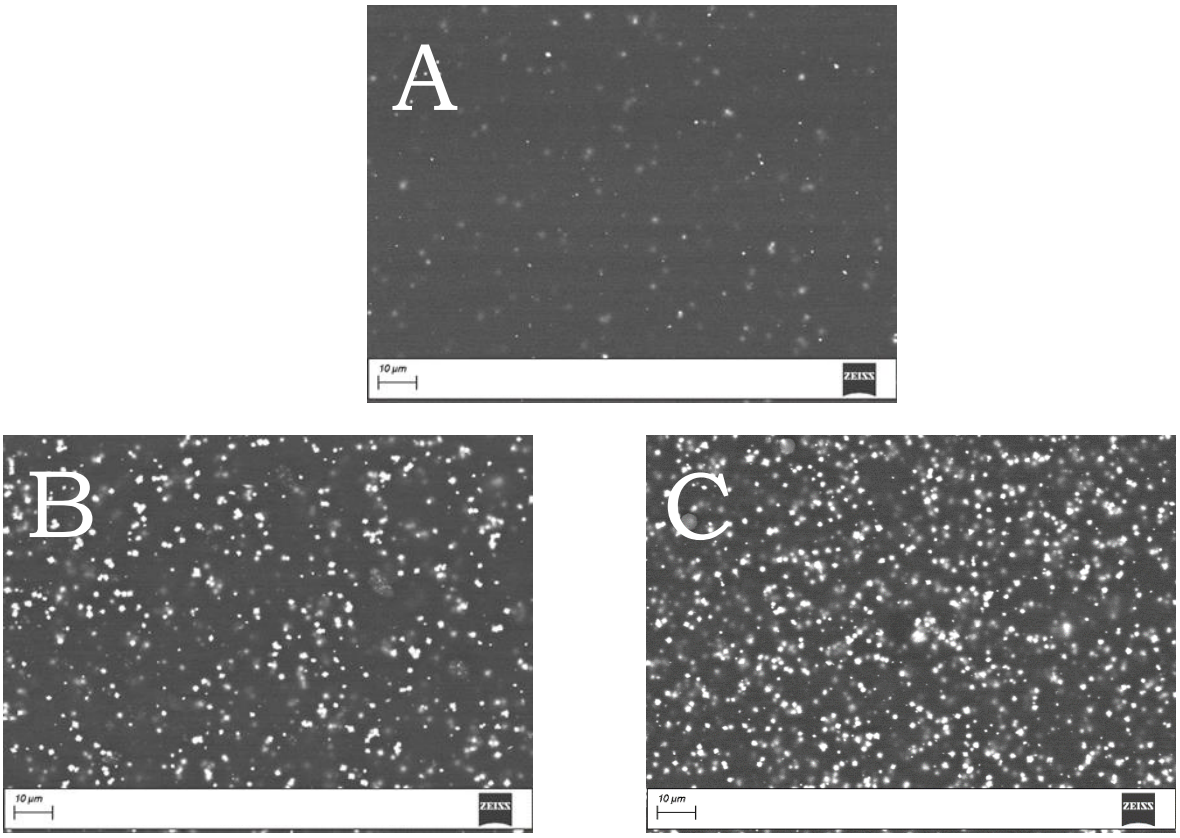

Figure 3.2.7. SEM micrographs obtained by using back scattered electrons of EB-ZFL 4, 10 and 20 surfaces.

3.2.4. Structural analysis of ZnO composites, cellulose composites and ZnO+cellulose composites

Figure 3.2.8 collects the X-ray diffraction patterns of ZnO composites. All the spectra are characterized by the presence of the broad amorphous halo centered at about 2θ =19°, due to the acrylic polymer matrix.

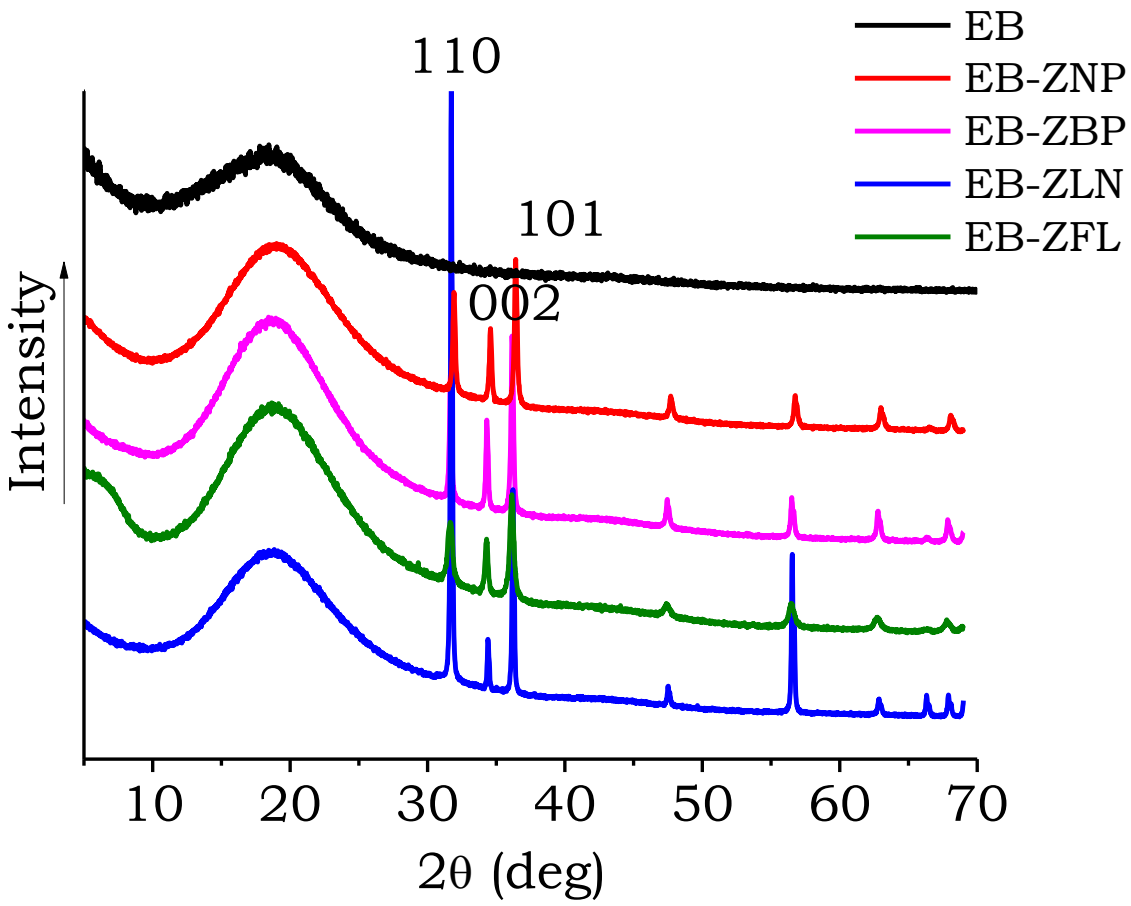

Figure 3.2.8. WAXD patterns of ZnO composites.

They also contain the most intense reflections of the crystallographic planes belonging to the hexagonal form of wurtzite (ZnO) at 2θ = 31.9° (110), 34.5° (002) and 36.3° (101).

In Figure 3.2.9, the diffraction patterns of grinded and ball milled cellulose composites are shown. The main peaks of cellulose, that appear in the range between 19 and 26°, are generally hindered by the acrylic amorphous halo centered at about 2θ =19°. In some spectra, the peak at 22.6° appears as a small shoulder in the graph, as indicated by the arrows.

Finally, Figure 3.2.10 compares all the WAXD spectra of EB-C-ZnO composites and EB-BMC-ZnO composites. Here, again, the most intense crystallographic planes of the ZnO hexagonal form are visible, together with a small shoulder at 22.6°, attributable to cellulose.

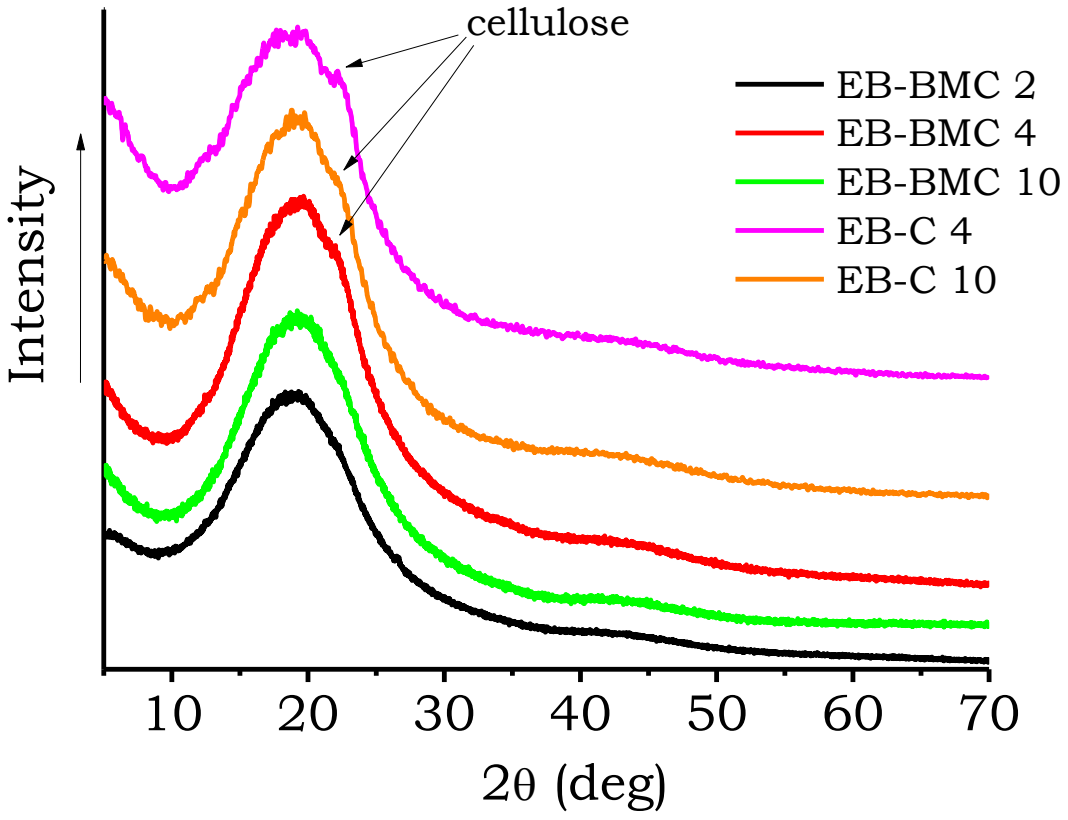

Figure 3.2.9. WAXD patterns of cellulose composites.

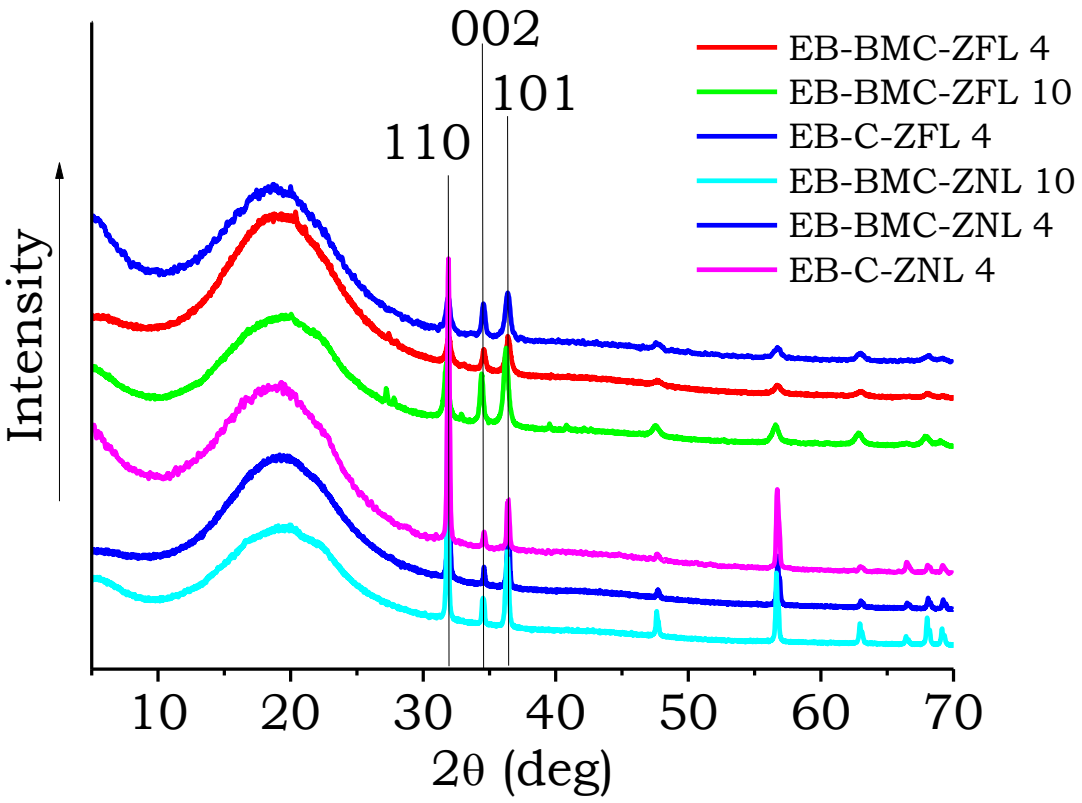

Figure 3.2.10. WAXD patterns of cellulose composites.

The most interesting result provided by these measurements is the different orientation of the characteristic crystallographic plane of ZnO in the composites. In Figure 3.2.11 A, the diffraction patterns of ZnO composite is reported in the range between 30 and 37°. The curves have been normalized with respect to the 110 crystallographic peak. It is noteworthy that the composite containing ZLN has a low amount of 002 planes oriented in the plane of the film, whereas these planes are more abundant in the films incorporating ZNP, ZBP or ZFL. In particular, the ZFL composite has the most intense 002 peak. As expected, no variation in the relative intensity of the peaks by changing the ZnO loading occurs (Figure 3.2.11B). The same behaviour has been found for the systems containing ZnO and cellulose as shown in Figure 3.2.11C. This result is important, because it can help to understand the different behaviour in terms of piezoelectric response.

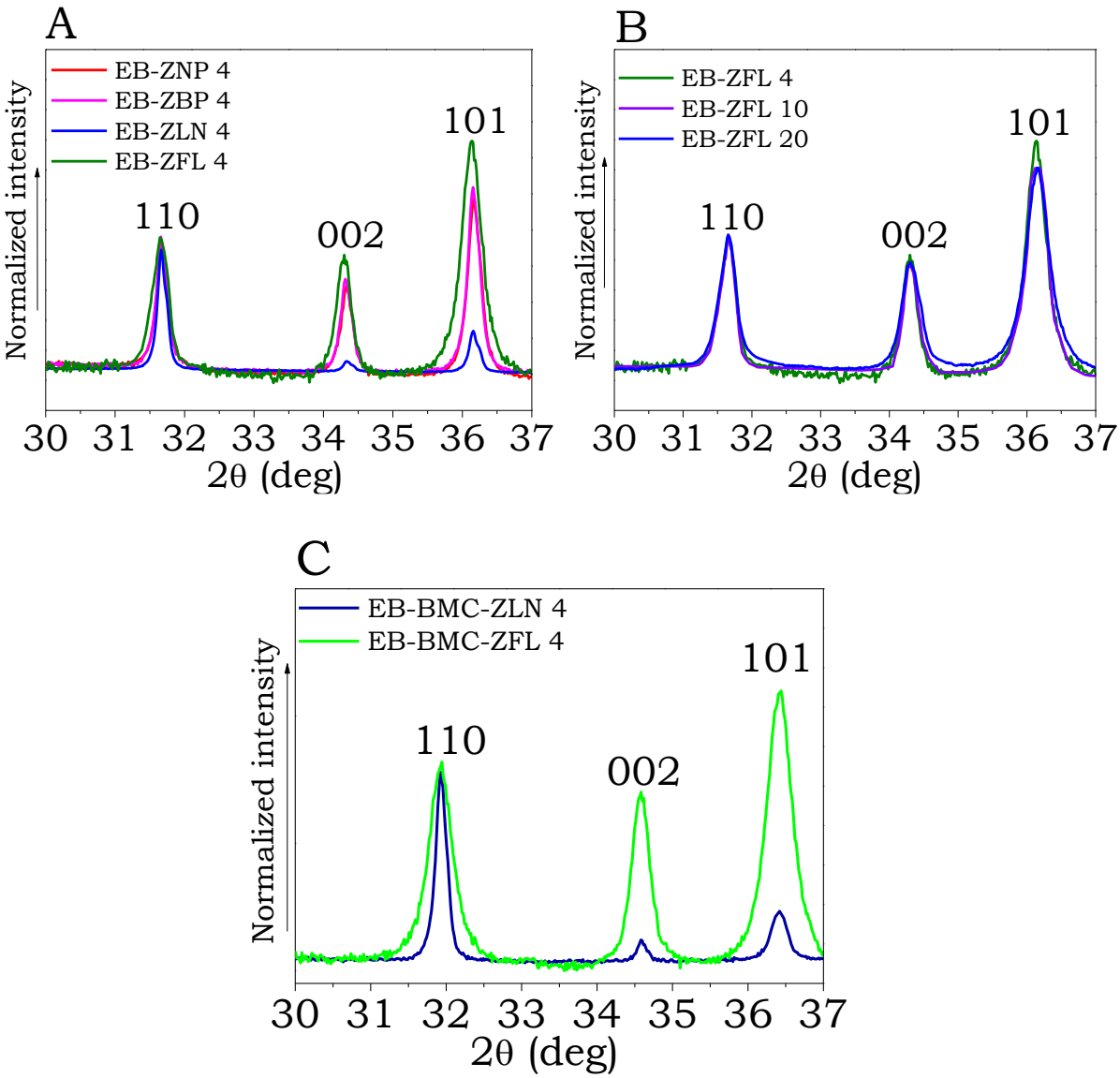

Figure 3.2.11. WAXD patterns of ZnO composites in the range between 30 and 37° for highlighting the preferential orientation of crystallographic planes of different ZnO morphologies in the composite films. Spectra have been normalized respect to the 110 crystallographic peak.

3.3. Thermal behavior of the composite films

3.3.1. Thermogravimetric analysis of ZnO powders and cellulose

Figure 3.3.1 shows the TG curves of ZnO powders in air. As expected, even in oxidative conditions, the oxides are stable and no significant weight loss is recorded even at 800°C.

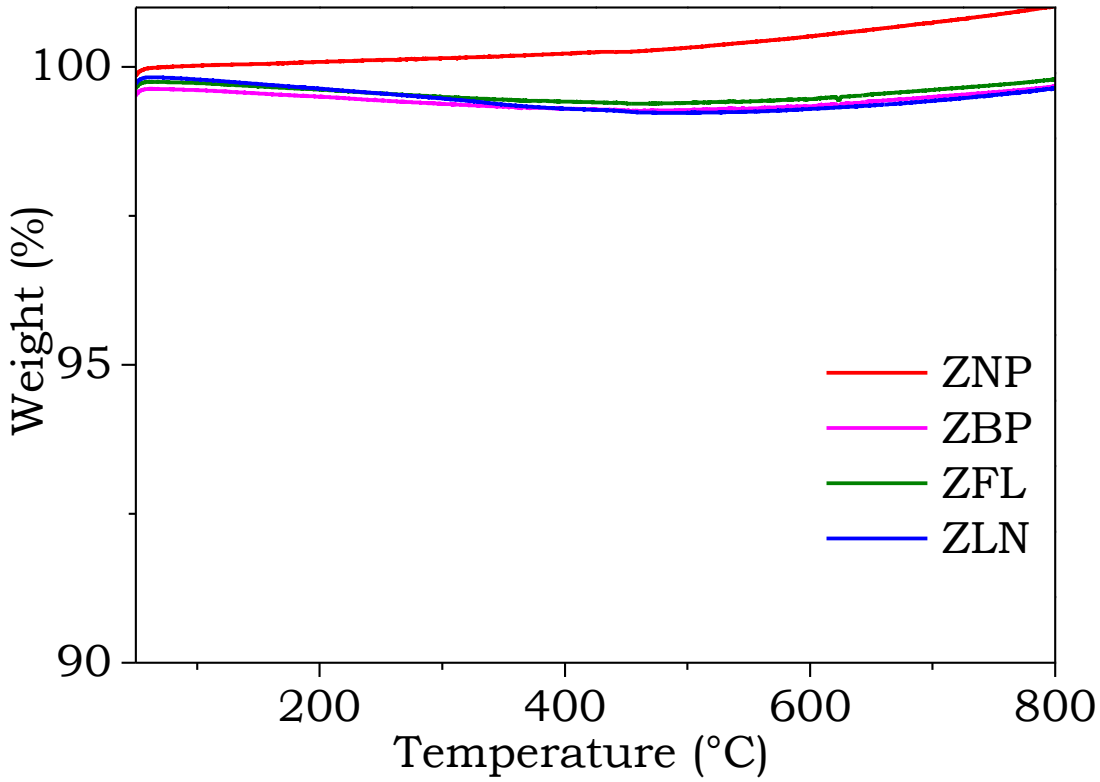

Figure 3.3.1. TGA of ZnO powders in air.

Figure 3.3.2 shows the TG and dTG curves for commercial, grinded and ball milled cellulose, both in air and in N_2. All the thermograms show the typical multi steps thermal degradation of cellulose nanocrystals.

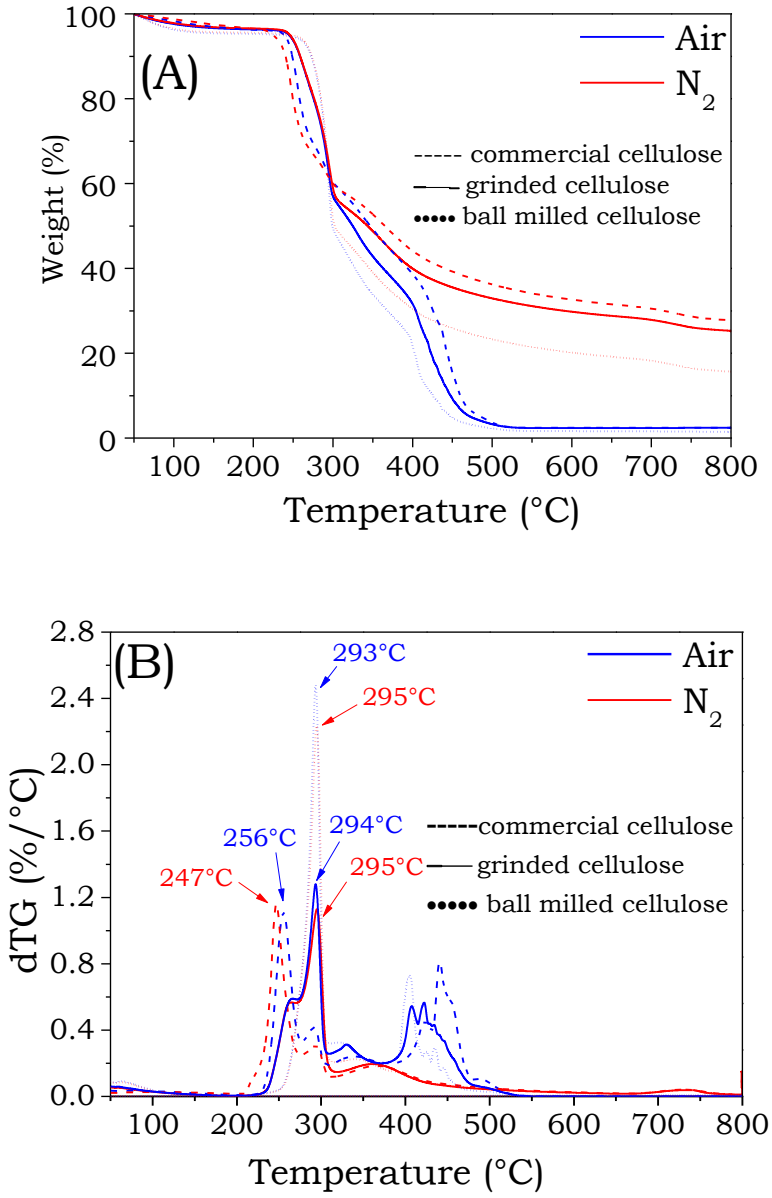

Figure 3.3.2. (A) TG and (B) dTG of commercial, grinded and ball milled cellulose in air and in N_2.

In the literature, this stepwise behavior is ascribed to the presence of sulphate groups, as a consequence of the treatment with sulphuric acid used for obtaining the cellulose nanocrystals, which lowers the thermal stability of the nanocrystals and is responsible for the broad temperature range of degradation with respect to native cellulose [92,93]. The initial weight loss of about 4% is due to the removal of loosely bound moisture [93-95] from the surfaces of these materials and is given off at approximately 130°C.

In N_2 atmosphere, the commercial cellulose loses nearly 45% of its mass within 180 and 300 °C. This weight loss is followed by a further 30% mass loss between 300 and 500 °C, leaving a residue of about 28 % at 600°C. The peaks in the dTG curves in the range between 180 and 400°C are attributable to concurrent degradation processes such as depolymerization, dehydration, and decomposition of glycosyl units, followed by the formation of a charred residue [93].

The charred residues of cellulose are almost completely volatilized by oxidation when air is used as purging gas. In particular, the dTG peaks above 425°C can be attributed to the oxidation and breakdown of the residues, toward the formation of gaseous product. The final residue is 2.3 wt.%.

Grinded cellulose, in the range 150-300°C is more stable than the commercial counterpart, both in air and N_2 (Figure 3.3.2.A); besides, position and intensity of the degradation peaks differ from those of the commercial cellulose. In this range, the lower temperature degradation step corresponds to degradation of the most accessible, and therefore most highly sulphated, amorphous regions, whereas the higher temperature degradation step is attributed to the breakdown of the non-sulphated crystal interior. During grinding, the rearrangement of the sulphated regions that probably become less accessible, is responsible for different intensity and position of dTG peak. Finally, the peak at about 380°C, which corresponds to the decomposition and volatilization of sulfuric acid molecules released in the previous step [96], is not significantly affected by the grinding process. The final residue is almost similar to that of commercial cellulose.

Ball milled cellulose is more stable in the range 150-300°C with respect to grinded and commercial counterpart, both in air and N_2 (Figure 3.3.2.A). Its thermograms show a principal fast decomposition step with onset temperature just close to 300 °C (Fig. 3.3.2.B). The ball milling process, that is stronger than grinding, has probably rearranged the sulphated regions that are even less accessible than before, causing a further shift of the degradation step at higher temperatures. The second peak is slightly shifted at lower temperatures with respect to those of grinded cellulose. Finally, in air, a massive mass loss occurs, leaving only 1.5 wt.% residue at 600 °C.

3.3.2. Thermogravimetric analysis of ZnO, cellulose and ZnO+Cellulose composite films.

Figures 3.3.3 A and B show the TG and dTG curves of composite films containing 4 wt.% of ZnO in nitrogen and air, respectively. The thermograms of EB-ZFL 10 and EB-ZFL 20 are similar to those of the films containing lower amounts of ZnO and are not reported for sake of simplicity. $T_{10\%}$ and T_{max}, i.e. the temperatures corresponding to 10% weight loss and to the maximum of the derivative curves, respectively, together with the char content at T_{max} and 700°C for all the compositions are listed in Table 3.3.1. In nitrogen atmosphere, the degradation of the neat resin and of all the ZnO composite films occurs according to a single step, ascribed to the breakage of the polymer network.

Furthermore, a slight weight loss, with a maximum at about 150°C, is observed: this finding may be attributed to the breaking up and loss of water strongly bound to the polymer network [97].

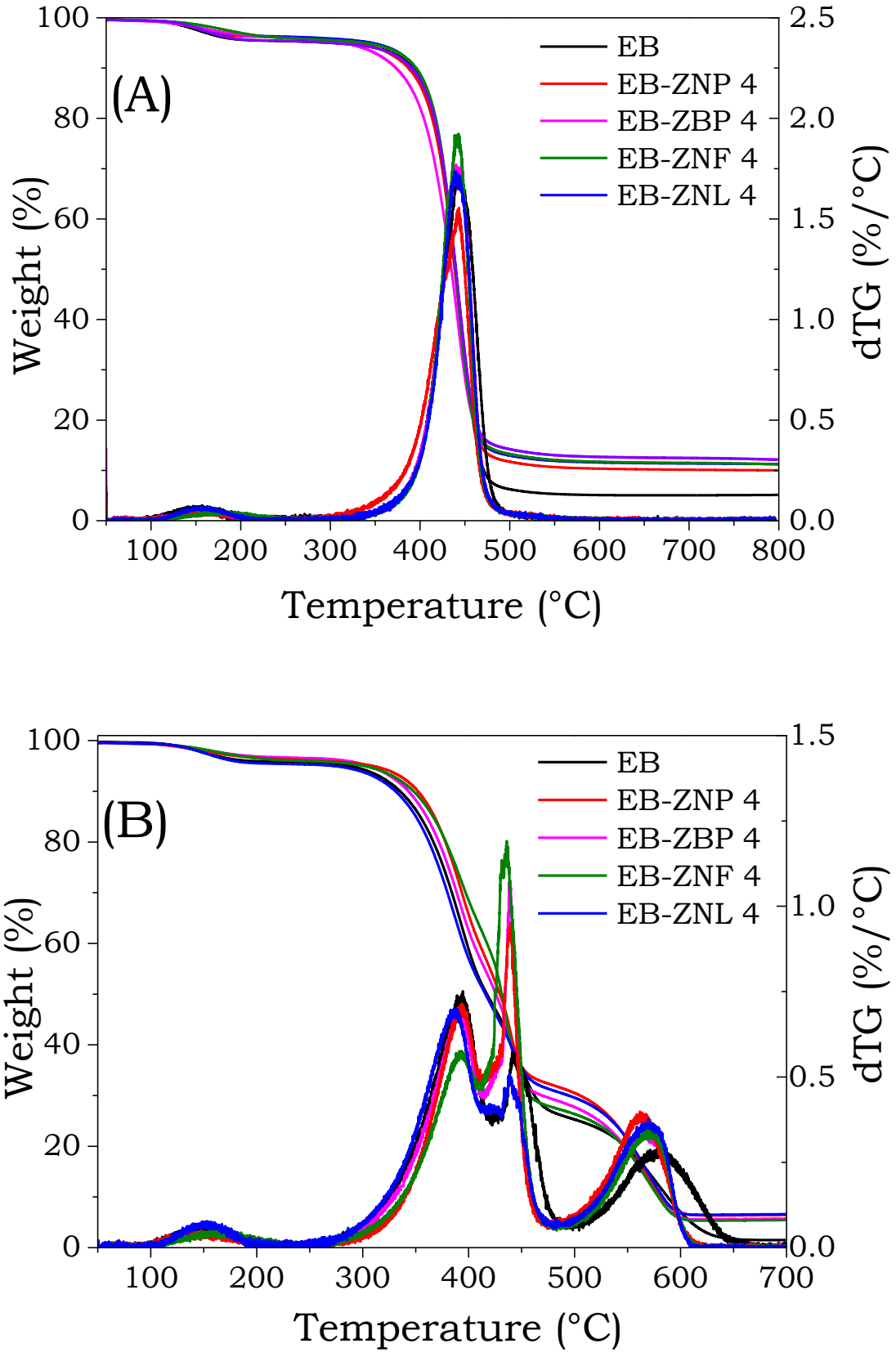

Figure 3.3.3. TG and dTG curves of ZnO composite films in nitrogen (A) and air (B).

In nitrogen, the type of morphology of ZnO fillers does not affect significantly the resin degradation process. Only EB-ZNP composite film shows a decrease of $T_{10\%}$ value (Table 3.3.2), indicating a slight anticipation of the degradation as compared to the unfilled UV-cured film. Furthermore, this anticipation increases by increasing the amount of ZnO filler. For the composite films EB-ZLF and EB-ZLN, $T_{10\%}$ and T_{max} values decrease by increasing the amount of filler (Table 3.3.2).

The thermo-oxidative degradation in air proceeds by three different steps (Figure 3.3.3B). The first one is ascribed to the degradation of dimers, trimers, …, which are formed during the UV-curing process. The second one refers to the main degradation of the cross-linked polymer, while the last peak is attributed to the oxidation of the degradation products formed during the previous steps [83]. Whatever the fillers morphology is, a slight increase in the thermal stability at low temperatures can be observed, as shown by the shift of the thermograms toward higher temperatures. In fact, $T_{10\%}$ values increase as compared with the unfilled UV-cured network. This effect is even more pronounced for compositions containing filler loadings beyond 4 wt.% and can be ascribed to the initial physical barrier exerted by ZnO to the diffusion of the degradation products of the polymer matrix [98,99]. Conversely, at higher temperature, ZnO catalyzes the degradation processes, decreasing the T_{max} values and sharpening the curves as compared to that of neat resin. All the composite films show a higher residue at 700°C with respect to the unfilled UV-cured resin, both in nitrogen and in air: in particular, in air, the residues at 700°C are in good agreement with the theoretical nanofiller content.

Figures 3.3.4A and B show TG and dTG curves of composite films containing different amounts of ball milled cellulose in nitrogen and in air atmosphere, respectively. The thermogravimetric data are listed in Table 3.3.2. All the thermograms (both in N_2 and in air) are similar in shape to that of neat EB; the further peak detected at about 300°C is due to the cellulose degradation, as described in paragraph 3.3.1.

Table 3.3.1. Thermogravimetric data of EB/ZnO composite films

	N_2				Air							
	$T_{10\%}$ (°C)	T_{max} (°C)	Residue @ T_{max} (%)	Residue @700°C (%)	$T_{10\%}$ (°C)	T_{max1} (°C)	Residue @ T_{max1} (%)	T_{max2} (°C)	Residue @ T_{max2} (%)	T_{max3} (°C)	Residue @ T_{max} (%)	Residue @700°C (%)
EB	391	443	45	5.0	335	394	63	442	41	580	12	1.5
EB-ZNP 4	373	442	40	12.3	353	394	71	440	42	563	16	6.4
EB-ZBP 4	394	443	44	11.4	343	392	67	439	41	572	13	5.7
EB-ZNF 4	396	442	45	11.5	348	393	70	436	45	572	13	5.4
EB-ZNL 4	390	443	42	12.5	335	387	65	440	40	572	14	6.6
EB-ZNF 10	372	412	58	12.4	356	384	72	427	53	549	19	12.1
EB-ZNF 20	367	407	67	20.0	356	386	71	427	54	547	28	20.2

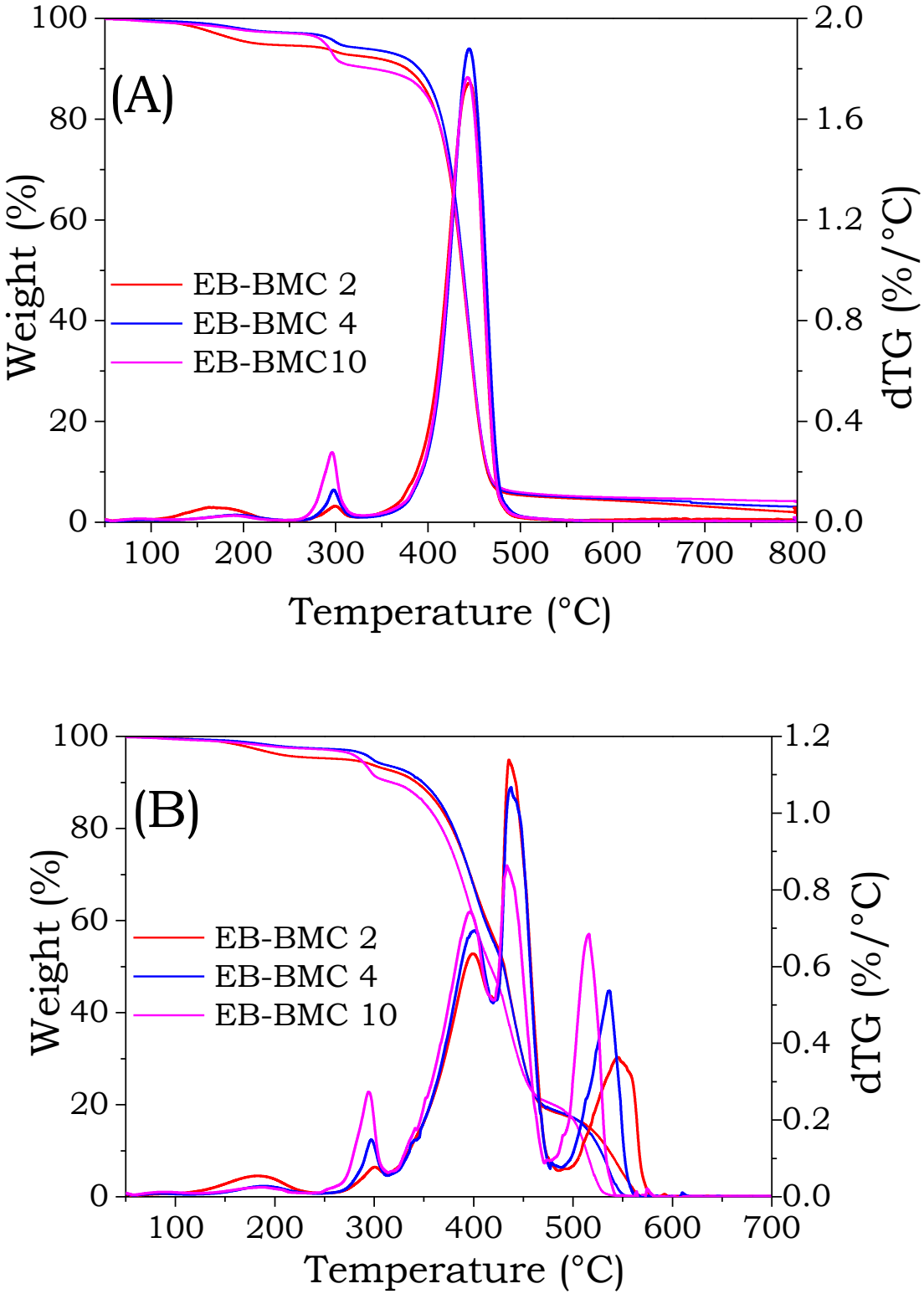

Figure 3.3.4. TG and dTG curves of ball milled cellulose (BMC) composite films in nitrogen (A) and air (B).

In nitrogen, the amount of ball milled cellulose does not significantly affect the resin degradation process (T_{max} is always about 443°C). However, $T_{10\%}$ significantly decreases by increasing the cellulose amount, thus indicating that the cellulose decreases the thermal stability of the resin in nitrogen atmosphere. This finding has been already reported in the literature [100-102] and can be ascribed to the release of sulfuric acid from anhydroglucose units that further accelerate the decomposition of the acrylic matrix. A similar behaviour has been found also for the composite films EB-C 4 and EB-C 10 (Table 3.3.2). In the thermo-oxidative conditions, the ball milled cellulose causes the anticipation of T_{max2} and T_{max3} with respect to neat EB at any composition. EB-BMC 2 and EB-BMC 4 have a higher $T_{10\%}$ with respect to EB, whereas for EB-BMC 10 this value drops significantly (i.e. at 318 °C vs. 335°C for the unfilled network). The composite films containing grinded cellulose follow the same trend of the films containing ball milled cellulose, with slightly lower values of degradation temperature. This finding indicates a higher stability of the ball milled composite as compared to the grinded counterparts.

Table 3.3.2. Thermogravimetric data of EB/cellulose composite films

	N_2					Air								
	T_{cell}	$T_{10\%}$ (°C)	T_{max} (°C)	Residue @ T_{max} (%)	Res. (700°C) (%)	T_{cell}	$T_{10\%}$ (°C)	T_{max1} (°C)	Residue @ T_{max1} (%)	T_{max2} (°C)	Residue @ T_{max2} (%)	T_{max3} (°C)	Res. @ T_{max3} (%)	Res. (700°C) (%)
EB*	-	391	443	45	5.0	-	335	394	63	442	41	580	12	1.5
EB-C 4	288	390	444	35	3.9	291	339	387	58	433	42	543	6	-
EB-C 10	287	385	443	40	5.2	294	330	386	57	433	44	544	8	-
EB-BMC 2	299	390	445	36	3.1	300	342	400	60	436	44	547	6	-
EB-BMC 4	297	377	443	42	3.8	297	347	400	60	438	42	536	6	-
EB-BMC 10	296	359	443	40	4.5	295	318	396	63	433	40	515	9	-

*In the table, the thermogravimetric data of EB are repeated for an easier comparison

Figures 3.3.5A and B show the TG and dTG curves of composite films containing different amounts of ball milled cellulose and ZFL or ZLN. In the thermograms, the peak at about 300°C is ascribed to the degradation of cellulose; it is noteworthy that the thermal degradation (both in air and in nitrogen) is similar to the previous series.

In nitrogen, both $T_{10\%}$ and T_{max} slightly decrease with respect to the unfilled resin; this behaviour is more evident at higher concentration of cellulose+ZnO. In air, again, the higher is the concentration of filler, the lower is the degradation temperature. However, $T_{10\%}$ and T_{max1} are always higher, whereas T_{max2} and T_{max3} are always lower as compared to UV-cured EB, hence indicating a higher thermal stability of the composite films. Again, the composite films containing grinded cellulose+ZnO follow the same trend of the films containing ball milled cellulose+ZnO, with slightly lower degradation temperatures. The higher stability of composite films containing ball milled cellulose with respect to the composite films containing grinded cellulose can be ascribed to the less accessible sulphated regions of the former. This causes the release of sulphuric acid only at higher temperature, hence promoting a higher thermal stability [102]. Furthermore, all the residues at T_{max} follow the same trend of those at 700°C and generally increase by increasing the filler loading.

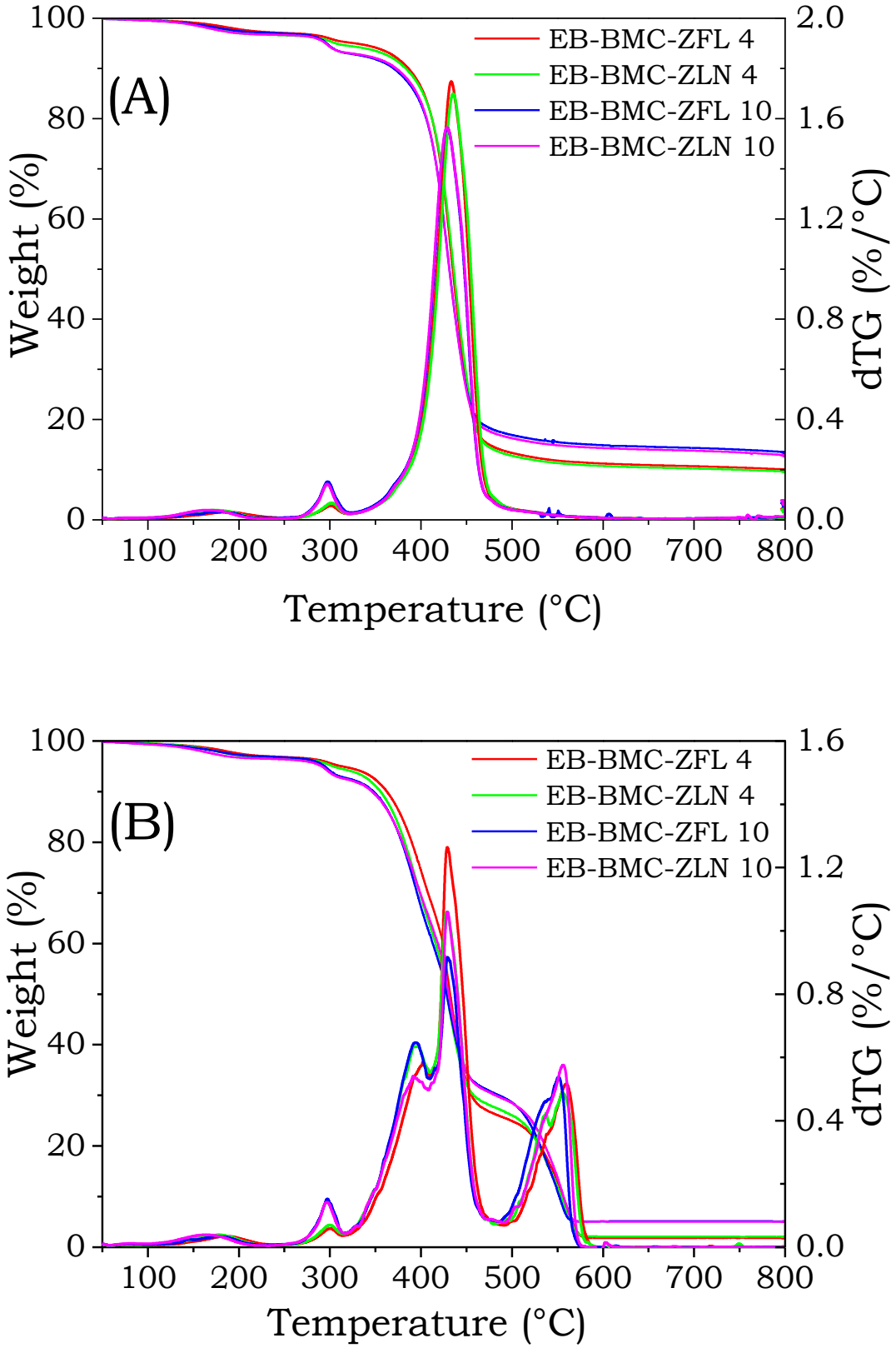

Figure 3.3.5. TG and dTG curves of BMC+ZnO composites in nitrogen (A) and air (B).

Table 3.3.3 Thermogravimetric data of EB/cellulose+ZnO composite films

	N_2					Air								
	T_{cell}	$T_{10\%}$ (°C)	T_{max} (°C)	Residue @ T_{max} (%)	Residue @ 700°C (%)	T_{cell}	$T_{10\%}$ (°C)	T_{max1} (°C)	Residue @ T_{max1}	T_{max2} (°C)	Residue @ T_{max2}	T_{max3} (°C)	Residue @ T_{max3}	Residue @ 700°C (%)
EB		391	443	45			335	394	63	442	41	580	12	1.5
EB-BMC- ZFL 4	302	386	433	53	10	300	362	398	75	429	54	559	8	2
EB-BMC ZFL 10	297	372	429	53	13	297	346	393	72	429	49	551	10	5
EB-BMC ZLN 4	302	383	435	52	10	300	356	394	73	429	49	556	9	2
EB-BMC ZLN 10	297	372	429	53	13	297	346	391	74	430	50	556	10	5
EB-C ZLN 4	288	383	433	50	10	293	335	377	71	430	46	545	8	2.5
EB-C ZFL 4	290	384	433	50	10	292	331	378	71	429	45	548	9	3

*In the table, the thermogravimetric data of EB are repeated for an easier comparison

3.3.3. DSC characterization of the composite films

DSC measurements have been performed in order to either confirm the completeness of the curing process (as evidenced by ATR-FTIR in the section 3.2) or to investigate the influence of fillers on the glass transition temperature of EB matrix. In Figure 3.3.6, the first and second heating up DSC runs for the different ZnO composite films are shown. For all the samples, in the first run, the appearance of enthalpy relaxation, which is superimposed to the specific heat changes associated with the glass transition of the polymer matrix, is ascribed to the high photocuring kinetics. More specifically, the UV-curing process freezes the macromolecules in a non-equilibrium thermodynamic state. Furthermore, in the first run, no exothermic phenomena are observed above the enthalpy relaxation, hence indicating that the completeness of the curing process was achieved in the adopted experimental conditions, even in the presence of the different fillers.

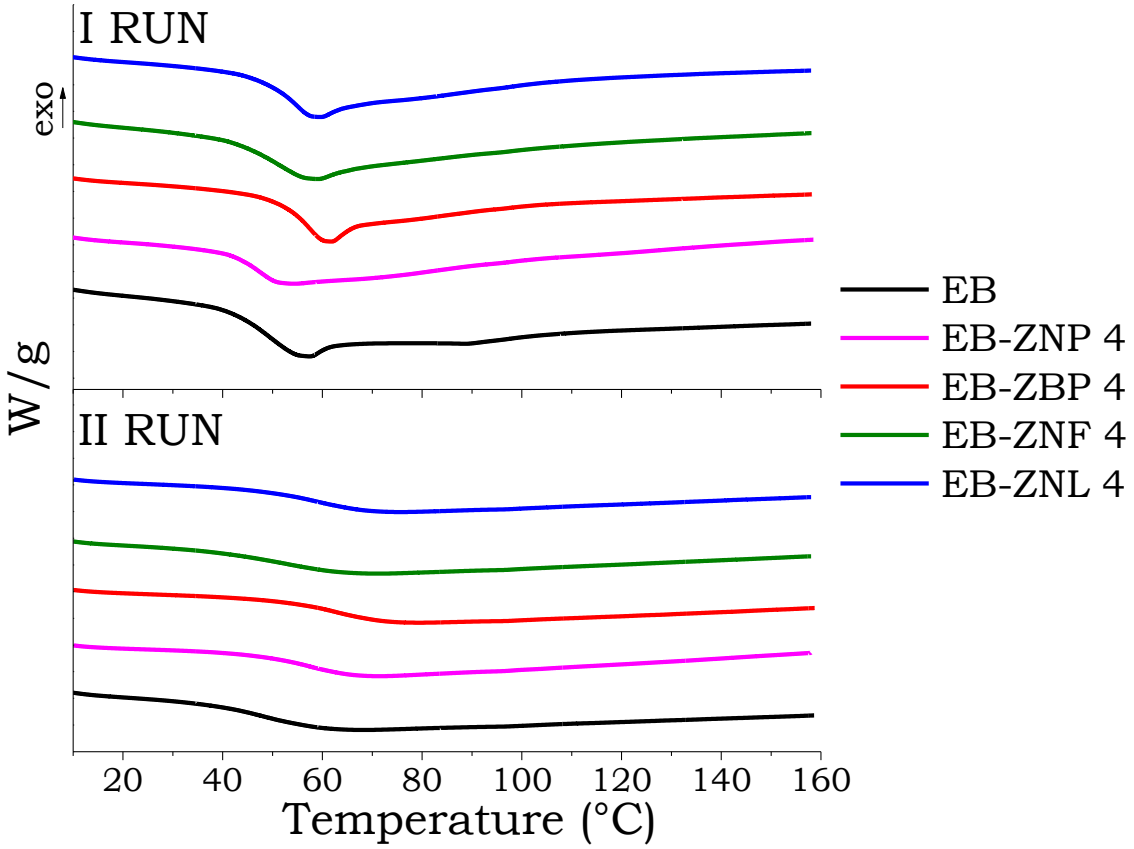

Figure 3.3.6. DSC thermograms (1st and 2nd run) of ZnO composite films (Heating rate: 10°C/min).

In the second run, the enthalpy relaxation disappears and only the glass transition is detectable, which is higher than that of the first run.
All the other composite films (i.e. EB-cellulose and EB-cellulose-ZnO) behave similarly to the unfilled UV-cured resin and the thermograms are not report for sake of simplicity. The glass transition temperature values of all the composite films are collected in Table 3.3.4.

Table 3.3.4. T_g of composite films by DSC thermograms

	T_g (I RUN)	T_g (II RUN)
Composite films containing ZnO in different morphologies		
EB	50	50
EB-ZNF 4	52	53
EB-ZLN 4	55	60
EB-ZBP 4	57	64
EB-ZNP 4	48	59
EB-ZNF 10	54	77
EB-ZNF20	54	65
Composite films containing cellulose grinded in a mortar(C)		
EB-C 4	50	63
EB-C 10	53	64
Composite films containing ball milled cellulose (BMC)		
EB-BMC 2	50	68
EB-BMC 4	48	68
EB-BMC 10	49	66
Ternary composite films containing grinded cellulose (C) and different ZnO morphologies		
EB-C-ZFL 4 (2-2)	53	68
EB-C-ZLN 4 (2-2)	54	65
Ternary composite films containing ball milled cellulose (BMC) and different ZnO morphologies		
EB-BMC-ZFL 4 (2-2)	48	65
EB-BMC-ZFL 10 (5-5)	51	71
EB-BMC-ZLN 4 (2-2)	45	65
EB-BMC-ZLN 10 (5-5)	46	59

All the composites have T_g similar or slightly higher with respect to that of unfilled UV-cured resin. In the second run, the increase in T_g is more evident, indicating that the fillers interact with the polymer segments, somehow limiting the mobility of these latter [103]. The thermal treatment the specimens underwent before the second heating run, i.e. the heating up beyond the glass transition and the subsequent cooling down, allows the free macromolecule segments between cross-link points to re-arrange in a more stable conformational structure. Furthermore, the amount of filler does not

modify the T_g (I RUN) of the resin (e.g. T_g =52°C, 54 and 54°C for EB-ZFL 4, EB-ZFL 10 and EB-ZFL 20, respectively). Besides, the presence of cellulose does not significantly affect the T_g of the resin. Finally, it is noteworthy that there is not a clear influence of the amount of filler on the T_g of composites. This can be ascribed to the possible formation of agglomerates, especially at high filler loadings.

3.4. Dynamic mechanical (DMTA) behavior of the composite films

3.4.1. Dynamical mechanical thermal analysis of EB composite films

In this chapter, the storage modulus, loss modulus and tanδ (i.e. the ratio of the loss modulus to the storage modulus) curves obtained by dynamical mechanical thermal analysis (DMTA) for all the composite films are reported and discussed. It is recall that the measurements were conducted in the temperature range from 25 to 120°C, heating rate of 3°C/min and 1 Hz of frequency. For each formulation, the tests were repeated three times and the experimental error was calculated as standard deviation for all the measured parameters. Figure 3.4.1 (A, B, C) shows the storage modulus, the loss modulus and tan δ as a function of temperature for all the EB-ZnO systems investigated. Figure 3.4.2 (A and B), 3.4.3 (A and B) and 3.4.4 (A and B) show the storage modulus and the tanδ of EB-ZFL 4, 10 and 20, EB-BMC 2, 4 and 10 and EB-BMC-ZnO 4 and 10 as a function of temperature, respectively. All the graphs also include EB curves for easier comparison. Glass transition temperatures (measured as the maximum of the tanδ peak) and storage modulus values at 30°C for all the systems are summarized in table 3.4.1.

The DMTA curves of EB-ZnO composite films containing different shaped ZnO (Figure 3.4.1) indicate that the presence of the fillers at 4wt.% slightly reduces (or has no effect in the case of EB-ZNF system) the storage modulus of neat EB in the glassy state. Conversely, in the rubbery plateau, the storage moduli E' increase with respect to the unfilled polymer network. In this case, the highest E' value is shown by EB-ZNL (20% higher as compared to unfilled UV-cured film), while EB-ZNP shows the lowest increase (10%).

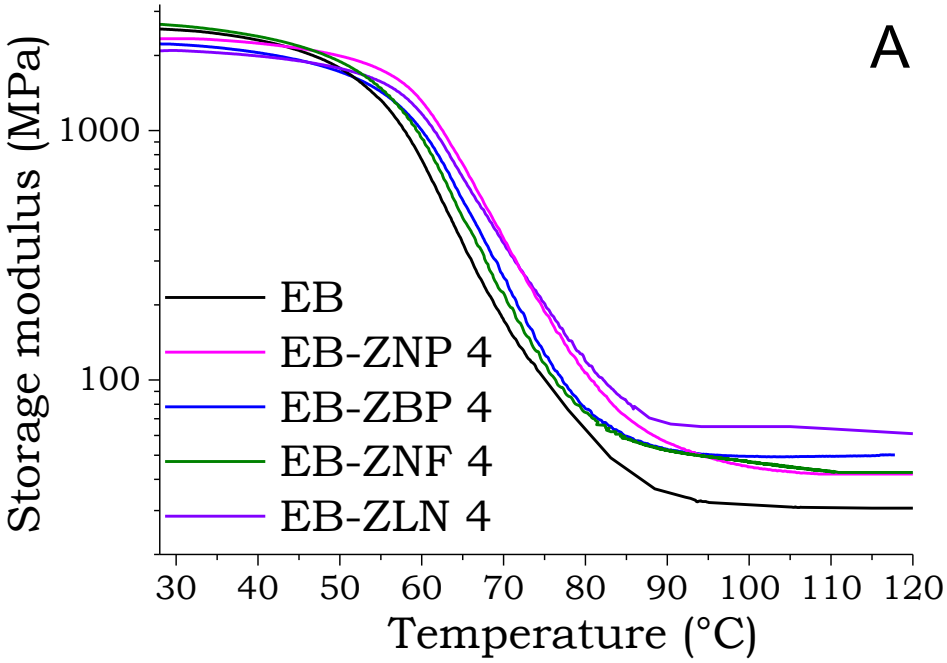
A
Storage modulus (MPa)
1000
100
EB
EB-ZNP 4
EB-ZBP 4
EB-ZNF 4
EB-ZLN 4
30 40 50 60 70 80 90 100 110 120
Temperature (°C)

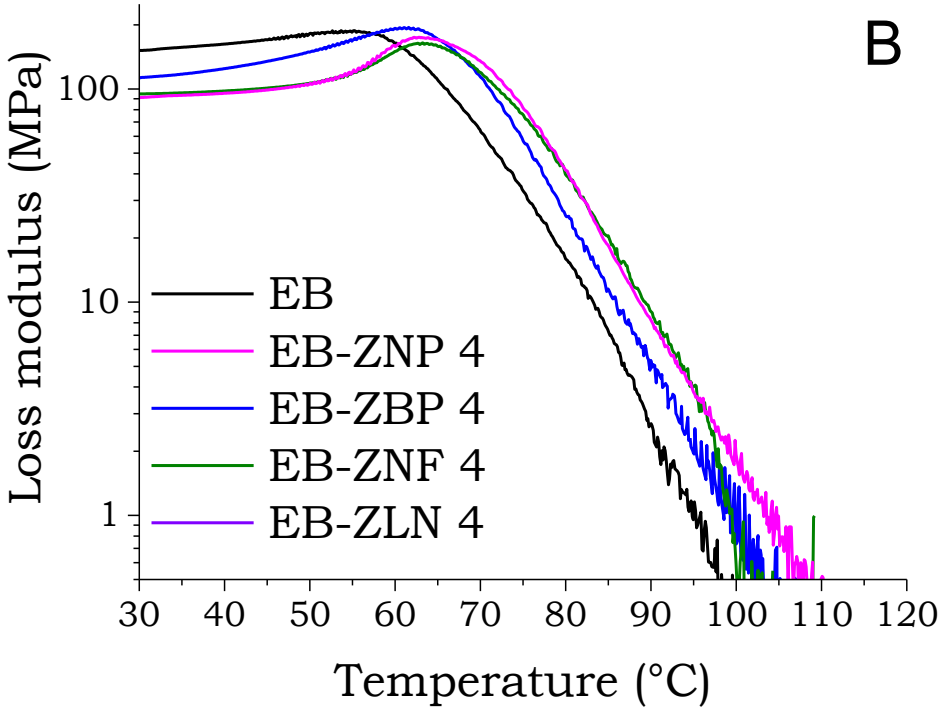
B
Loss modulus (MPa)
100
10
1
EB
EB-ZNP 4
EB-ZBP 4
EB-ZNF 4
EB-ZLN 4
30 40 50 60 70 80 90 100 110 120
Temperature (°C)

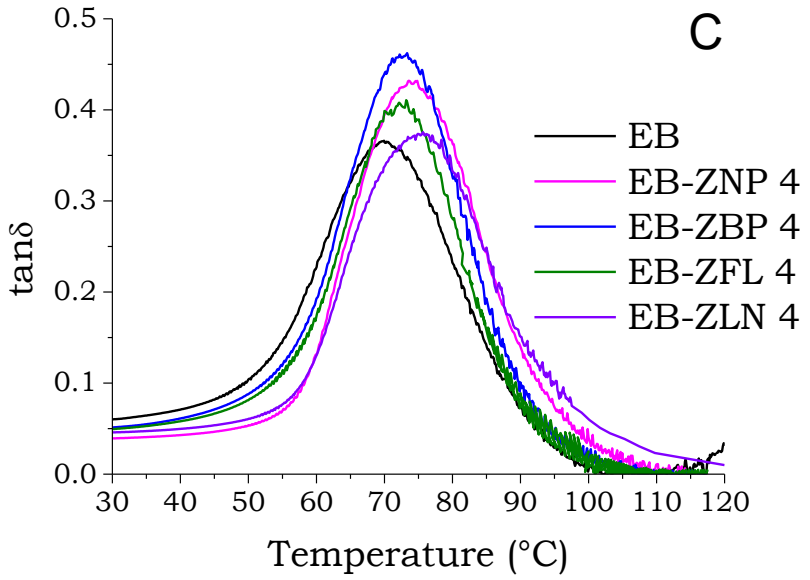

Figure 3.4.1. (A) Storage modulus (on log scale), (B) loss modulus (on log scale) and (C) tanδ of EB-ZnO composites.

From the dissipation factor (tan δ) values (Figure 3.4.2), it is clear that the glass transition temperature (T_g) of the composite films is slightly shifted towards higher temperatures by about 4-6°C, due to the presence of the ZnO, which acts as a reinforcement of the polymer network [104,105]. These findings are in good agreement with the DSC results previously discussed.

Figures 3.4.2 A and B show the storage modulus and tanδ of EB-ZFL composite with different amounts of ZFL, respectively. From an overall point of view, it is possible to note that by increasing the ZNF loading: i) the storage modulus (Figure 3.4.2 A) increases in the rubbery state (see also table 3.4.1); ii) the T_g increases (Figure 3.4.2 B and table 3.4.1). These findings may be ascribed to good interactions taking place between the filler and the polymer. Besides, the increase of ZNF concentration leads to a slight broadening of the tanδ (for EB-ZNF 10 and 20), due to restriction effects that suggest a small suppression of the glass transition by the presence of the flower-like morphologies [106]. As stated previously, the increase of the T_g confirms that ZnO acts as a reinforcing agent.

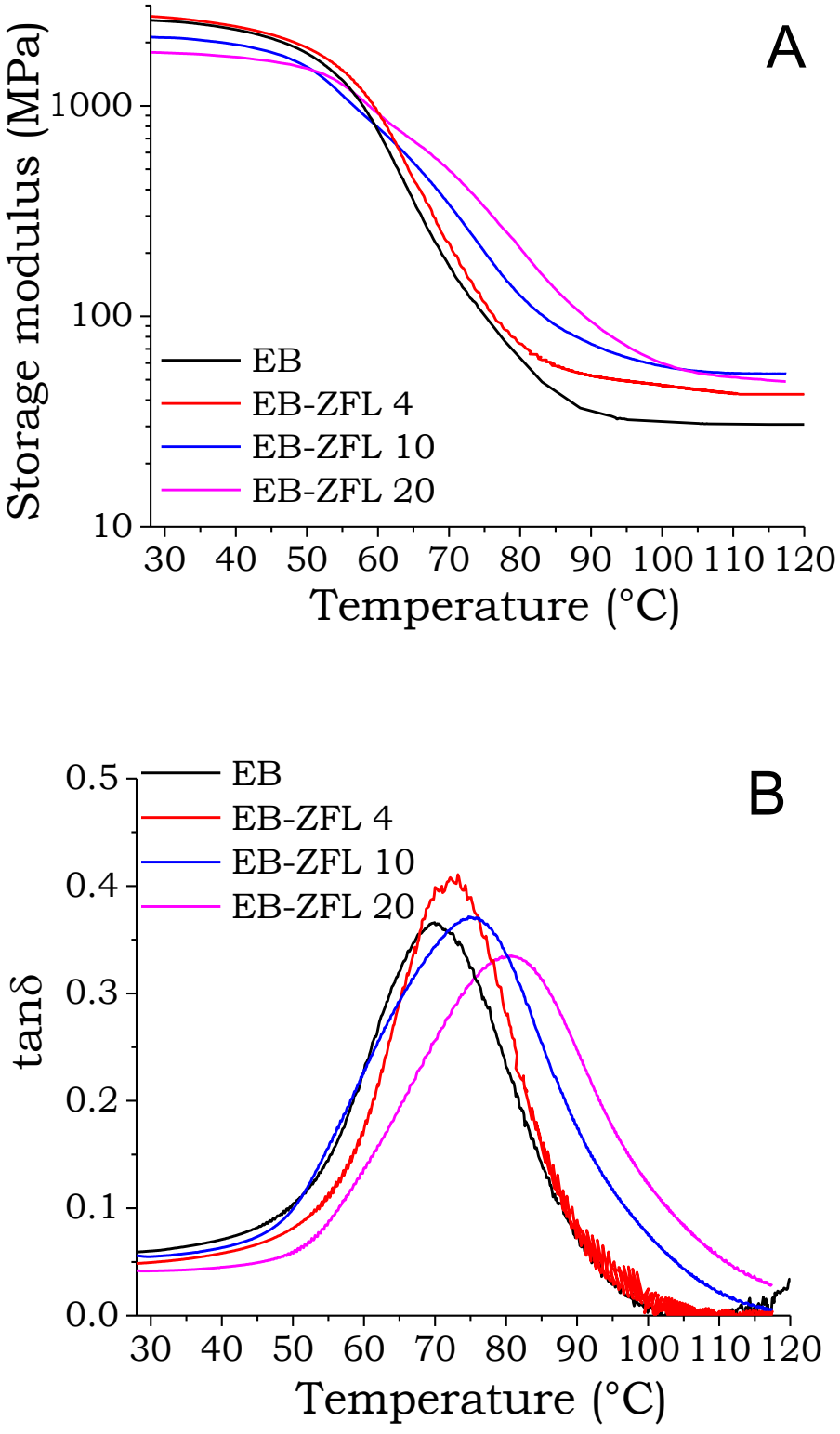

Figure 3.4.2. (A) Storage modulus (on log scale) and (B) tanδ of EB-ZNF composites containing different amount of ZNF.

Figures 3.4.3 A and B show the storage modulus and tanδ of EB-BMC composites containing different amounts of ball milled cellulose. Similarly, to the systems containing different ZFL loadings, the glass transition increases. The storage modulus in the rubbery state is always higher than that of neat EB, but it does not seem to be particularly affected by the amount of BMC (Figure 3.4.3 and table 3.4.1). Also in this case, cellulose reinforces the polymer matrix.

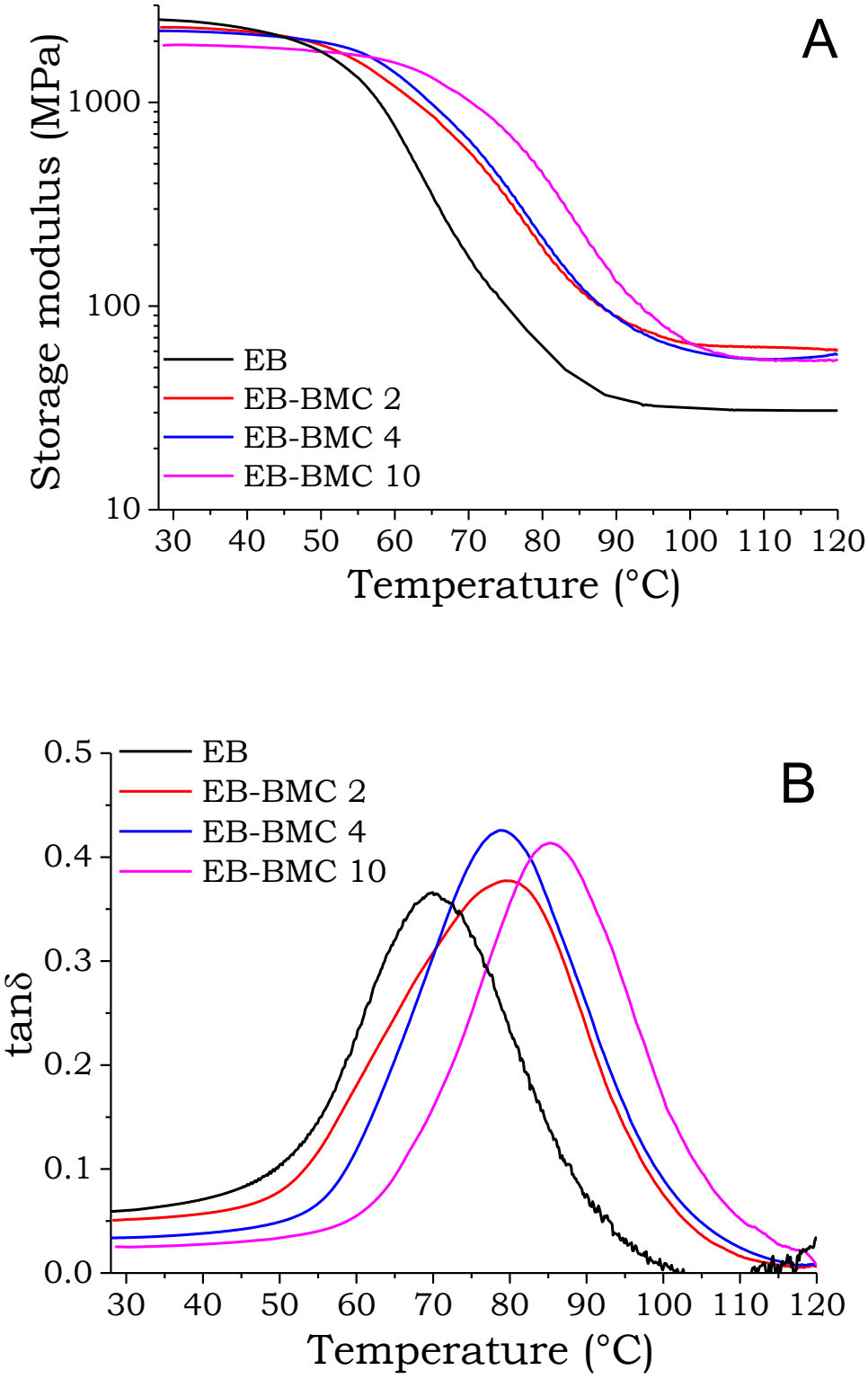

Figure 3.4.3. (A) Storage modulus (on log scale) and (B) tanδ of EB-BMC composites.

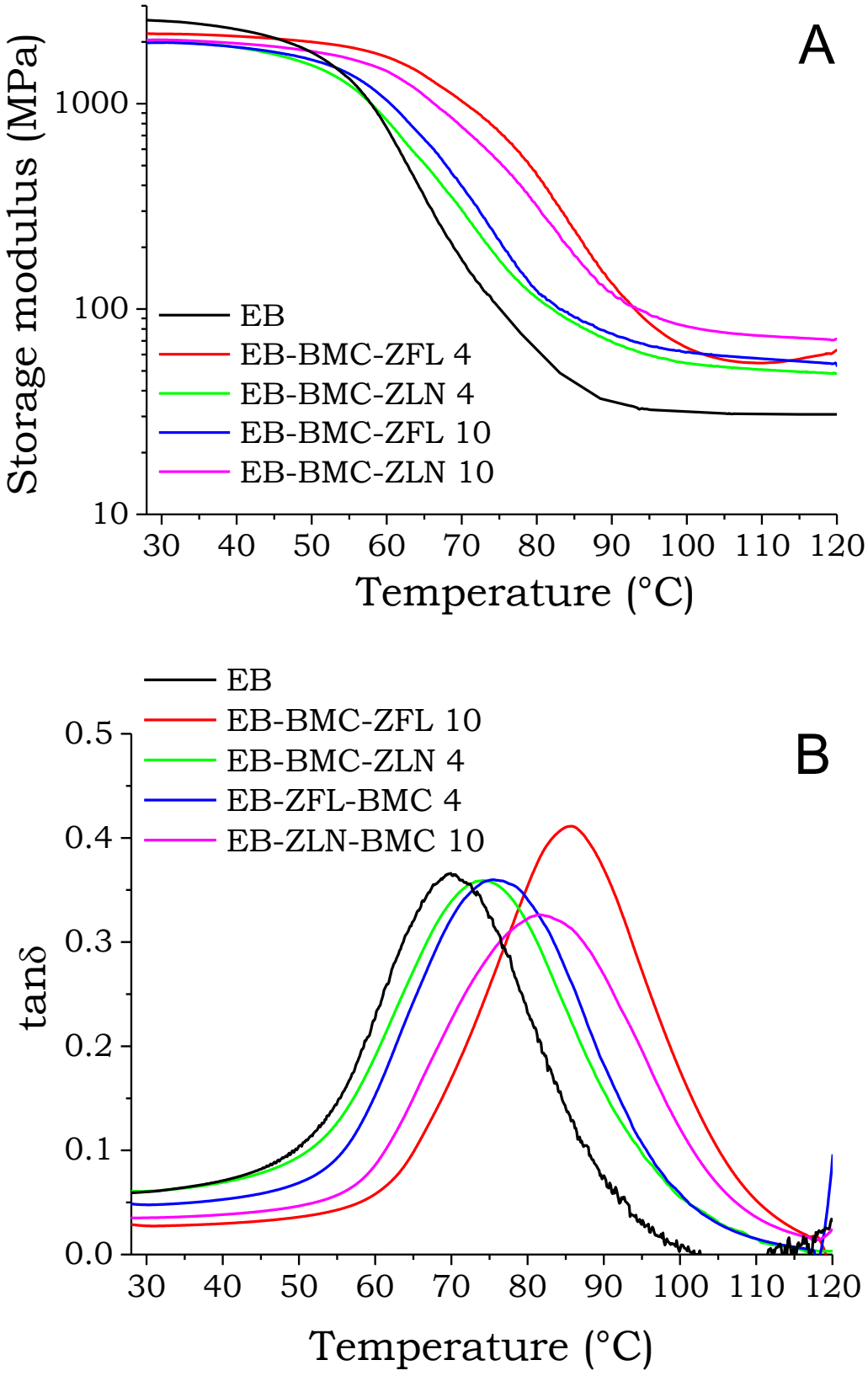

Figure 3.4.4. (A) Storage modulus (on log scale) and (B) tanδ of EB-BMC-ZFL and EB-BMC-ZLN composites.

The samples containing both BMC and ZnO show a viscoelastic behaviour similar to the other systems just described (Figure 3.4.4), with T_g values that increase with increasing the filler loadings.

From the values collected in Table 3.4.1, it is worthy to highlight that:

1) the sample containing grinded cellulose with or without ZnO (i.e EB-C 4 and 10, EB-C-ZFL 4 (2-2) EB-C-ZLN 4 (2-2)) show higher T_g values than those containing BMC (with the same composition).

2) the composites containing ZnO are stiffer than those containing cellulose (being equal the composition).

Table 3.4.1. T_g of composite films by tanδ, storage modulus at 30°C and 100°C

	T_g (°C)	E' (MPa) @ 30°C	E"(MPa) @ 100°C
Composite films containing ZnO in different morphologies			
EB	70±2	2537±52	32±3
EB-ZNF 4	73±1	2637±62	48±4
EB-ZLN 4	75±2	2089±49	67±5
EB-ZBP 4	73±2	2207±56	49±5
EB-ZNP 4	74±2	2333±57	44±4
EB-ZNF 10	76±3	2111±87	58±6
EB-ZNF20	81±3	1791±110	60±3
Composite films containing cellulose grinded in a mortar (C)			
EB-C 4	84±1	1669±74	44±4
EB-C 10	89±3	1443±67	40±2
Composite films containing ball milled cellulose (BMC)			
EB-BMC 2	79±3	2341±101	65±3
EB-BMC 4	80±2	2246±71	60±3
EB-BMC 10	85±2	1915±93	65±5
Ternary composite films containing grinded cellulose (C) and different ZnO morphologies			
EB-C-ZFL 4 (2-2)	82±3	1899±38	45±6
EB-C-ZLN 4 (2-2)	82±4	1136±96	35±2
Ternary composite films containing ball milled cellulose (BMC) and different ZnO morphologies			
EB-BMC-ZFL 4 (2-2)	76±2	2189±86	65±4
EB-BMC-ZLN 4 (2-2)	74±4	2042±88	55±7
EB-BMC-ZFL 10 (5-5)	86±5	1984±64	62±6
EB-BMC-ZLN 10 (5-5)	82±2	2042±58	83±4

3.5. Piezoelectric behavior of the composite films

3.5.1. Piezoelectric behaviour of neat EB resin

The responses, both in time and frequency domain, of the beams fabricated by using the synthesized composite films were evaluated as a preliminary step for experimentally assessing their behavior in terms of energy harvesting capability.

The effective piezoelectric character of composites films has been demonstrated by comparing their piezoelectric features with those of unfilled UV-cured resin. The generated voltages vs. excitation frequency were normalized to maximum acceleration and the obtained values were elaborated as root mean square (RMS) in order to compare the results with the filled systems reported in the next paragraphs. Table 3.5.1 shows the normalized generated voltages from 10 to 3500 Hz, which are close to noise limit, without any correlation with the excitation frequency.

Table 3.5.1. Normalized RMS voltage of a cantilever made of unfilled UV-cured resin at different excitation frequencies

	Max applied acceleration (g max)	Normalized RMS voltage (mV RMS/g max)
10 HZ	2.07 ± 0.01	0.017 ± 0.001
2000Hz	2.07 ± 0.01	0.017 ± 0.001
10 Hz	5.38 ± 0.01	0.017 ± 0.001
150 Hz	5.38 ± 0.01	0.017 ± 0.001
1000 Hz	5.38 ± 0.01	0.019 ± 0.001
2000 Hz	5.38 ± 0.01	0.021 ± 0.001
3005 Hz (resonance)	5.38 ± 0.01	0.019 ± 0.001

As an example, the generated output voltage (blue line) inside the limit noise recorded for the unfilled resin is depicted in Figure 3.5.1 for stresses applied at 150Hz. It is worthy to note that the bare resin is not able to generate any electrical signal when stressed at different frequencies and accelerations.

Figure 3.5.1. Example of input stress (yellow and pink curves) and output voltage (cyan line) for unfilled UV-cured EB at 150Hz.

3.5.2. Piezoelectric behaviour of EB-ZnO at 150 Hz and resonance frequencies

In all cases, the synthesized materials exhibit a piezoelectric response. The resonance frequency of the prepared cantilevers is 2488 for EB-ZNP, 2445 for EB-ZFL, 2899 for ZBP and 3195 Hz for EB-ZLN. Figure 3.5.2 and 3.5.3 show the output voltages generated by each selected nanofiller at the frequency of 150 Hz and at the resonance frequencies, respectively, at about 5.4 g of maximum acceleration. The generated voltage and current signals show a regular and stable time response with constant amplitude output, due to the homogeneous distribution of the nanofillers within the host polymer network, as already proven by SEM analyses. The generated output voltage values were elaborated as root mean square (RMS), as shown in Figure 3.5.4 A and B for both analyzed frequencies (150 Hz and resonance frequency).

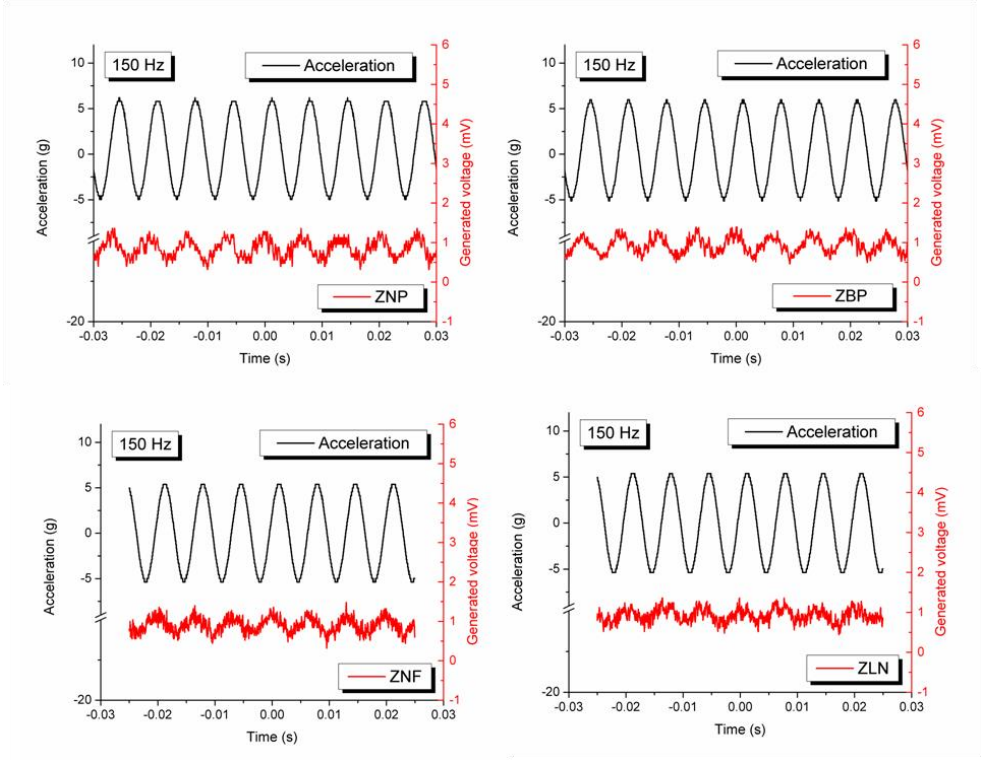

Figure 3.5.2. Generators output voltage (for EB-ZnO 96/4 containing different filler morphologies) at 150 Hz signal frequency.

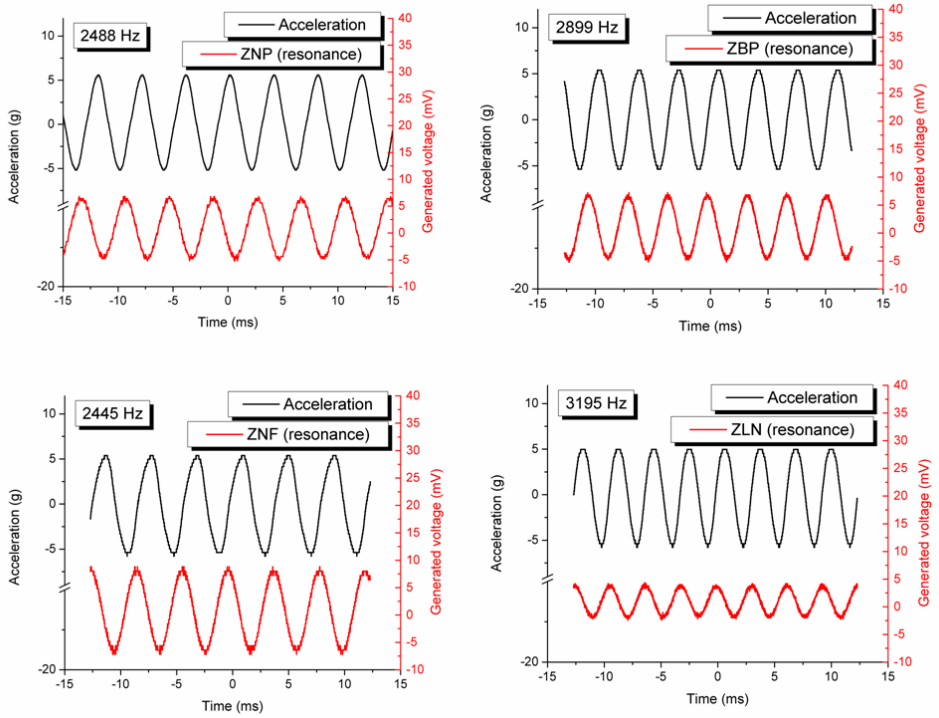

Figure 3.5.3. Generators output voltage (for EB-ZnO 96/4 containing different filler morphologies) at resonance frequency.

At lower frequency (150 Hz), the highest RMS voltage was registered for EB-ZNF and EB-ZLN films (maximum applied acceleration: 5.38 g) and it was

about 0.103±0.001 mV. It can be concluded that, at this frequency, there is no significant effect of the ZnO particle morphology on the piezoelectric response of the composites. Conversely, at the resonance frequency, some relevant differences can be underlined. In particular, the highest RMS voltage was measured on the UV-cured films containing ZNF filler (flower-like morphologies), with a maximum of 5.292±0.001 mV (that corresponds to a maximum peak-peak voltage of about 16.0±0.1 mVp-p (maximum applied acceleration: 5.79 g), whereas the lowest RMS voltage was measured for the UV-cured films containing ZLN filler (2.238±0.001 mV). In order to explain this different piezoelectric behavior, it is important to consider that the piezoelectric effect of ZnO depends on the orientation of the 0002 crystallographic planes. In particular, it is possible to reveal piezoelectricity if these planes are oriented perpendicularly to the applied mechanical stress [107]. In our systems, ZnO particles have random orientations; however, a small portion of (0002) crystals can be oriented in the desired direction, hence giving rise to voltage generation upon the application of the mechanical stress. The probability that the flower-like particles, in EB-ZFL films, have a higher number of 0002 planes oriented perpendicularly to the applied stress is higher with respect to the other morphologies. This is, therefore, due to their peculiar geometry that justifies the highest measured voltage at high frequencies. Conversely, ZLN particles, as also revealed by the SEM images shown in Figure 3.2.2, have mainly their z direction lying in the plane of the film. In the needle-like morphology, 0002 planes are perpendicular to their z direction [62,107]: this means that they are parallel to the stress application direction, hence determining the lowest RMS voltage recorded.

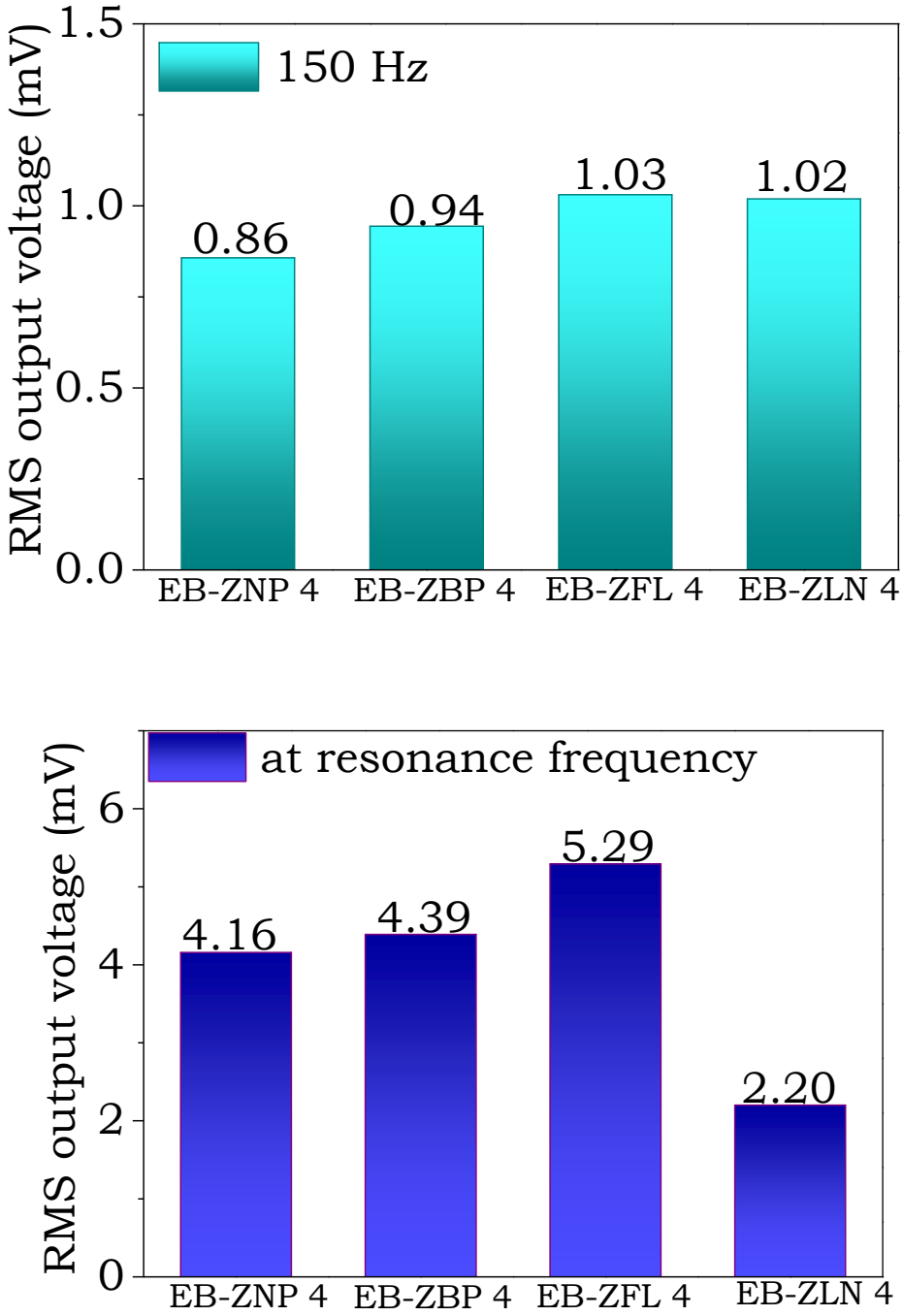

Figure 3.5.4. RMS voltage values (for EB-ZnO 96/4 containing different filler morphologies) at 150 Hz and resonance frequencies when acceleration is 5g (standard deviation of 0.02 mV).

Furthermore, it has to be considered that the mechanical properties can influence the piezoelectric response of a material. However, the influence of different particles on the storage modulus of EB composites (see Table 3.4.1) is not so relevant and therefore it cannot justify the observed different piezoelectric behavior.

3.5.3. Piezoelectric behaviour of EB-C and EB-C-ZnO at 150 Hz and resonance frequencies

The generated output voltage values for EB-C 95/5 and EB-C-ZNF and EB-C-ZLN, elaborated as root mean square (RMS), are reported in Figure 3.5.5 at 150 Hz and resonance frequency and at different accelerations (namely, 5, 7 and 10g).

In any case, the obtained films show a piezoelectric response, confirming the feasibility of the matrix-filler combinations in the design of the cantilevers. The resonance frequency of these latter is equal to 3.3 kHz.

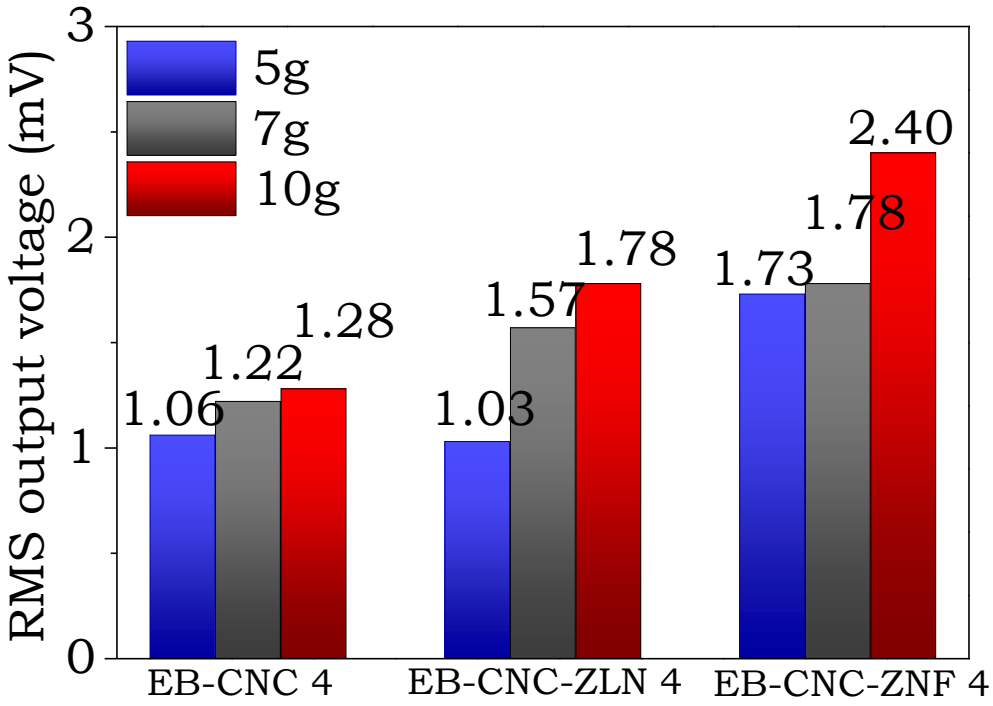

Figure 3.5.5. RMS voltage values for EB-C and EB-C-ZnO 96/4 containing different filler morphologies at the resonance frequencies when acceleration is 5, 7 and 10g (standard deviation: 0.02 mV).

For these systems, the output voltage signals are not detectable at 150Hz. At the resonance frequency, the output voltage increases with the applied acceleration. The contribution of grinded cellulose to voltage generation is quantifiable by the response of EB-C film at different accelerations, as the unfilled UV-cured resin did not show any detectable piezoelectric response. The piezoelectric capability of the composite was enhanced replacing 2 wt.% of CNC with ZnO morphologies. As indicated by the results, the composites containing ZnO flowers seem to be the most promising, in terms of generated

open circuit voltage, at different acceleration values. However, these systems have lower open circuit voltages with respect to the sample containing ZnO only. For getting significant output voltage signals, the acceleration has to be increased to 10g.

For these systems, the piezoelectric coefficient d_{33} was also measured in different points of the analyzed samples. The data have been organized through a normal probability plot. The following values have been found: 0.55 pC/N for EB-C, 0.17 for EB-C-ZLN and 0.23 for EB-C-ZFL. In particular, EB-C-ZFL generates higher voltage than ZLN, due to its higher d_{33} value. However, both EB-C-ZnO (ZnF and ZnN) produce higher output signals than EB-C sample (see Figure 3.5.5), though they exhibit a lower piezoelectric coefficient. This is probably due to the different direction of stress application used in the two experiments.

3.5.4. Piezoelectric behaviour of EB-BMC composites

For the systems containing ball milled cellulose in different amounts, the piezoelectric charge constant d_{33} was measured. The data have been plotted using a normal probability plot as shown in Figure 3.5.6.

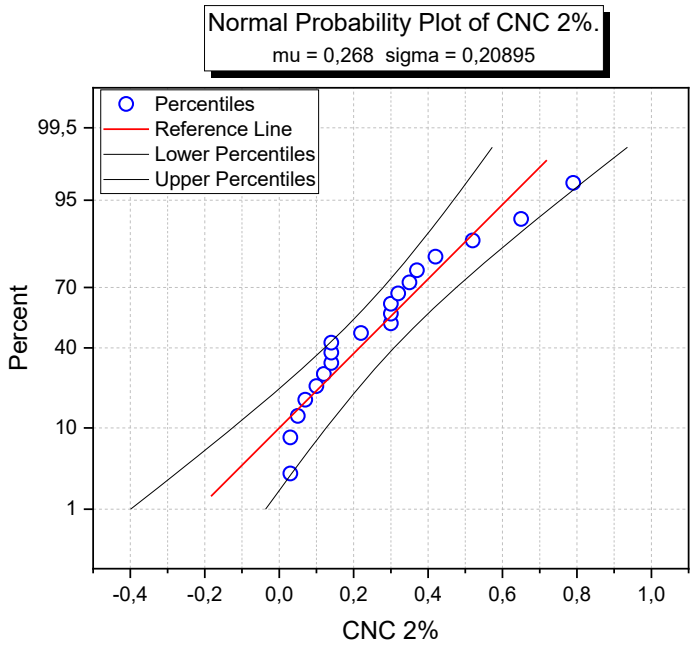

Figure 3.5.6. Normal probability plot for d33 of EB-BMC 98/2 composite film.

As shown in Figure 3.5.7, the d_{33} value increases by increasing the amount of BMC and reaches the maximum value of 1.07 pC/N for EB/BMC 90/10.

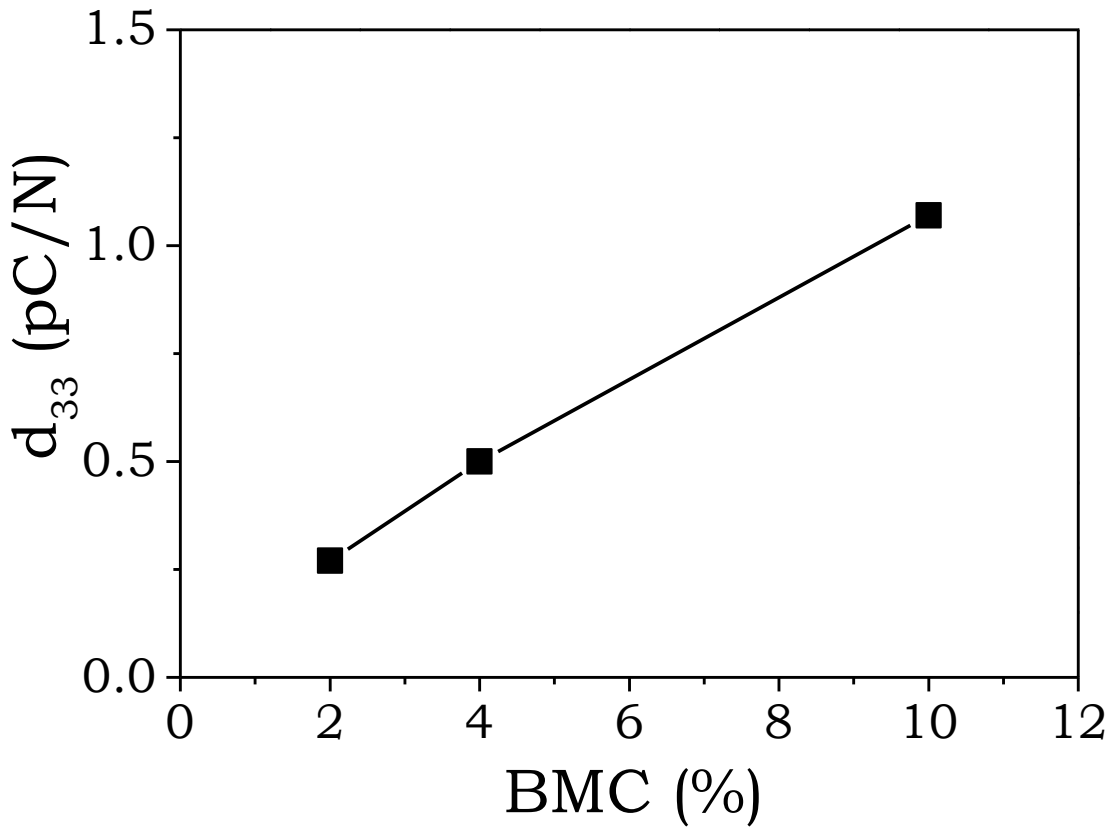

Figure 3.5.7. d_{33} coefficient for EB-BCM as a function of the BCM amount

3.5.5. Piezoelectric behaviour of EB-BMC-ZnO composites

Table 3.5.2 collects the piezoelectric coefficient for the systems containing both BMC and ZnO (ZFL and ZLN), together with the value for EB-BMC 4 and 10 for a better comparison.

Table 3.5.2. d_{33} for EB-BMC-ZnO composites

	d_{33} (pC/N)
EB-BMC 96/4	0.50
EB-BMC-ZFL 96/4 (2-2)	0.95
EB-BMC-ZLN 96/4 (2-2)	0.66
EB-BMC 90/10	1.07
EB-BMC-ZFL 90/10 (5-5)	1.30
EB-BMC-ZLN 90/10 (5-5)	1.10

The replacement of 2wt.% of BMC with 2wt.% of ZLN causes an increase of d_{33} from 0.50 to 0.66 pC/N (+25% increase), whereas the replacement with 2wt.% of ZFL increases d_{33} from 0.50 to 0.95 pC/N (+48% increase). Analogously, the replacement of 5wt.% of BMC with 5wt.% of ZnO raises d_{33} from 1.07 to 1.3 (+17%) and to 1.1 (+3%) for ZFL and ZLN, respectively. Again, ZFL morphology seems to perform better with respect to ZLN counterpart as already explained. However, it is worthy to underline that cellulose has a detrimental effect on the piezoelectric properties of the composite films as compared with ZnO. This is probably due to different factors including the lower crystallinity of cellulose, as well as the worse interfacial adhesion with polymer matrix. Besides, though the correlation with the storage modulus is not very clear, it seems that a lower storage modulus provides a lower piezoelectricity. Finally, it is also possible to observe that the ball milling process, by enhancing dispersion and distribution of cellulose in the acrylic resin improves the piezoelectricity and dielectric values with respect to the composites containing grinded cellulose [108,109].

3.5.6. Piezoelectric behaviour at low frequencies (≤ 100 Hz)

Some of the systems have also been investigated at the typical environmental vibration frequencies (<100 Hz and acceleration < 3g). To this aim, an electrically conductive layer was applied to the sample faces, using a conductive paint at room temperature, instead of a RF sputtering technique. Again, the generated output voltage of the unfilled resin is within the noise limit.

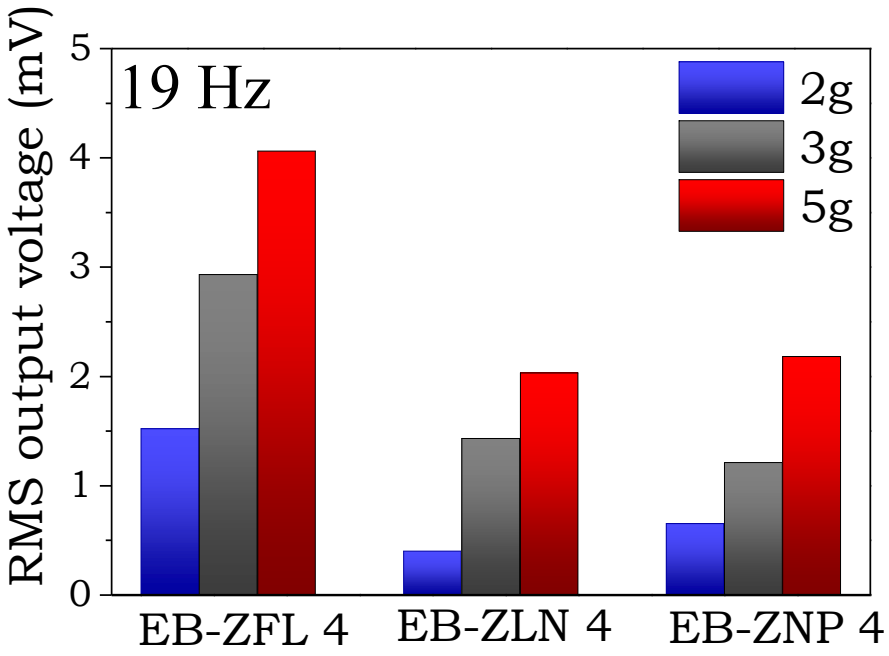

Figure 3.5.8. RMS output voltage produced by the composites containing 4 wt.% of ZnO at the frequency of 19 Hz and different acceleration value (standard deviation of 0.02 mV).

EB-ZnO composite films display enhanced generation properties at very low frequencies (i.e. at 11 and 19 Hz). The highest RMS voltage was registered for EB-ZNF in all the range of analyzed frequencies and irrespective of the loading and type of ZnO morphology employed. As an example, Figure 3.5.9 shows the normalized voltage RMS values (for the samples containing 4 wt.% of ZnO with different morphologies) at 19 Hz and different accelerations (namely, 2, 3 and 5g). Increasing the ZnO loading positively affects the piezoelectric response of the composites: as shown in Figure 3.5.9, the RMS voltage generated at 19 Hz as a function of acceleration is higher with the highest amount of ZFL used (i.e. 20 wt.%). However, the increase is not linearly correlable with the ZFL loading.

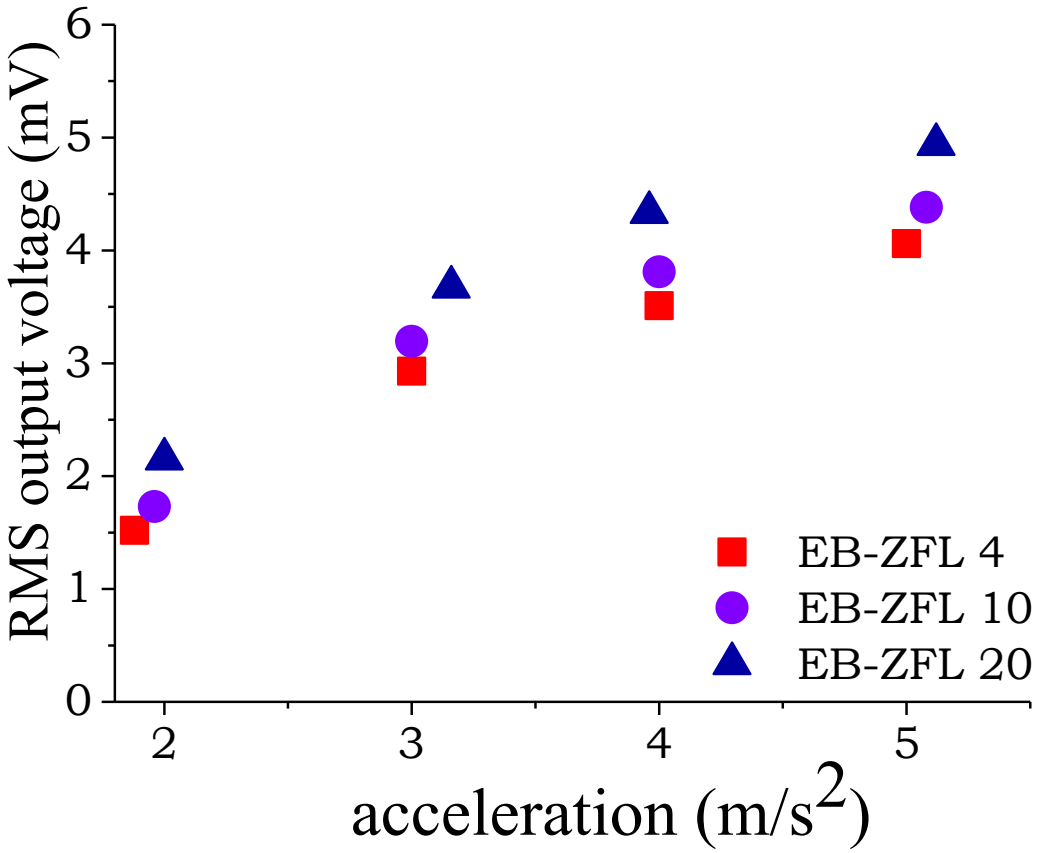

Figure 3.5.9. RMS output voltage by the sample EB-ZFL at different ZFL amount the frequency of 19 Hz vs. the acceleration value.

This piezoelectric behaviour does not depend on the dispersion of filler and on the number of particles on the surface as observed by SEM (section 3.2). Conversely, it seems more linked to the reduction of storage modulus of the composites at high ZFL concentration.

Chapter 4
Concluding Remarks

This chapter briefly highlights the main results obtained and discusses some possible perspectives for the future work.

4.1. Summary

In the present PhD thesis, cellulose and different morphologies of ZnO, synthesized on purpose, were embedded into a UV-curable acrylic resin (EB), aiming at studying the effect of the selected fillers on the piezoelectric properties of the resulting composite films. To this aim, four different morphologies of ZnO were synthesized, following a facile aqueous sol-gel route, namely: nano-particles (ZNP), bipyramidal (ZBP), flower-like (ZNF) and long needles (ZLN) morphologies. Cellulose nanocrystals (CNC) were purchased and subjected to mechanical treatments by grinding in a mortar (C) or by ball milling (BMC). Films of 150 μm of thickness were obtained with the highest achievable cross-linking density.

For the composites containing ZnO, only EB-ZLN and EB-ZNF showed a uniform distribution and dispersion of the fillers within the polymer matrix that was maintained also when the filler amount increased. For the composites containing cellulose, ball milling allowed obtaining a better dispersion, as well as a decrease of the size of cellulose domains dispersed in the polymer matrix as compared to the composites containing grinded cellulose.

The thermal stability of the composites was not worsened by the presence of the fillers. For ZnO composites, whatever the fillers morphology was, a slight increase in the thermal stability at low temperatures was observed; besides, at higher temperatures, ZnO was found to catalyse the degradation processes. For the cellulose-containing composites (with and without ZnO), ball milled cellulose promoted a higher stability of composite films with respect to those containing grinded cellulose.

In general, the increase of filler content (ZnO, cellulose or ZnO+cellulose) caused an increase of glass transition temperature (T_g) and a decrease of the storage modulus in the glassy state. The composites containing ZnO are stiffer than the composites containing cellulose; besides, the samples containing grinded cellulose with or without ZnO (i.e EB-C 4 and 10, EB-C-ZFL 4 (2-2) EB-C-ZLN 4 (2-2)) showed higher T_g values than those containing BMC (being equal the composition).

Then, the piezoelectric response generated by the polymer composites was satisfactory in terms of RMS (root mean squared) voltage measured as a function of the applied waveform, both at low and at resonance frequency. The highest voltage was registered for EB-ZNF (with and without cellulose) in all the range of analyzed frequencies. This result was explained by the higher probability that the flower-like particles, in the UV-cured films, have a higher number of 0002 planes oriented perpendicularly to the measured solicitation with respect to the other morphologies: indeed, this is due to their peculiar geometry.

Furthermore, the RMS voltage generated at 19 Hz as a function of the acceleration increased with increasing ZFL loading, reaching the maximum value at 20 wt.%, though the increase in RMS voltage increase is not linearly correlable with the ZFL loading. This finding was not ascribed to the dispersion of filler and to the number of particles on the surface of the composite films. Conversely, this behavior seemed to be more related to the decrease of storage modulus of the composites at high ZFL concentration.

As far as cellulose-containing composites are considered, it worthy to underline that cellulose showed a detrimental effect on the piezoelectric properties of the composite films as compared with ZnO. This is probably due to different factors, including the lower crystallinity of cellulose, as well as the worse interfacial adhesion with the polymer matrix. Besides, though the correlation with the storage modulus was not clearly interpreted, it seems that a lower storage modulus provides lower piezoelectricity. Finally, it was also possible to observe that ball milling process, by enhancing dispersion and distribution of cellulose within the UV-cured acrylic network, improved the

piezoelectricity and dielectric values with respect to the composites containing grinded cellulose.

4.2. Perspectives for the future work

Despite the high gap between the measured voltage values in this PhD thesis and those related to fully inorganic piezoelectric systems (which are 2-3 orders of magnitude higher) [110], the proposed piezoelectric films show two main advantages, i.e. flexibility and cost-effective scalability, which are key elements for innovative devices in the field of green technologies [66,111]. This suggests to continue the work by exploring i) new film components and ii) different electrode depositions.

In the first case, the idea is to use and study: 1) different UV-curable matrices and different filler ratios and/or 2) doped ZnO particles in order to obtain a ferroelectric material with switchable spontaneous polarization [112,113], able to increase the piezoelectric response.

Then, it could be reasonable to assessing the piezoelectric behaviour, changing the deposition of the electrodes on the composite film. In this work, the electrodes were deposited on the two surfaces of each film. However, different solutions have been considered in collaboration with the Institute of Metrological Research (INRIM), which consist in the deposition of electrodes, with different shapes, on a single surface. This solution becomes particularly relevant when the composite films would be exploited as coatings of moving objects. Furthermore, the solution of a single electrode, extended to the whole surface, will be modified by considering multiple electrodes, in interdigitated configuration, with series (to amplify the output voltage) and/or parallel (to maximize the detected current) connections.

Articles published in peer-review journals

1. “Preparation and characterization of UV-cured composite films containing ZnO nanostructures: effect of filler geometric features on piezoelectric response” G. Malucelli, A. Fioravanti, L. Francioso, C. De Pascali, M.A. Signore, M.C. Carotta, A. Bonanno, **D. Duraccio**. *Progress in Organic Coatings* 109 (2017) 45–54.

2. “UV-Cured Composite films Containing ZnO Nanostructures: Effect of Filler Shape on Piezoelectric Response” L. Francioso, G. Malucelli, A. Fioravanti, C. De Pascali, M.A. Signore, M.C. Carotta, A. Bonanno, **D. Duraccio**. Paper in Electrical Engineering book series (LNEE, volume 457).

3. “Synthesis and characterization of UV-curable nanocellulose/ZnO/AlN acrylic flexible films: thermal, dynamic-mechanical and piezoelectric response” M. A. Signore, C. De Pascali, **D. Duraccio**, G. Malucelli, A. Fioravanti, E. Melissano, M. C. Martucci, M. Masieri, P. Siciliano, L. Francioso. Journal of Applied Polymer Science. 138(4) (2021), 49731.

Proceedings

1. “UV-Cured Composite films Containing ZnO Nanostructures: Effect of Filler Shape on Piezoelectric Response” L. Francioso, G. Malucelli, A. Fioravanti, C. De Pascali, M.A. Signore, M.C. Carotta, A. Bonanno, **D. Duraccio**. AISEM Annual Conference on Sensors and Microsystems AISEM 2017: Sensors and Microsystems pp 323-330, Lecce (Italy), February 21-23, 2017.

2. “Hybrid piezoelectric films functionalized with ZnO nanostructures and cellulose nanocrystals” **D. Duraccio**, V. Strongone, A. Fioravanti, G. Malucelli. XXIII Convegno Nazionale dell'Associazione di Scienza e Tecnologia delle Macromolecole, Catania (Italy), September 9-12, 2018.

3. “Piezoelectricity measurements of hybrid films functionalized with ZnO nanostructures and cellulose nanocrystals” **D. Duraccio**, A. Fioravanti, G. Malucelli, R. Filippo, P.P. Capra. 19th International Congress of Metrology (CIM2019), Paris (France), September 24-26, 2019.

References

[1] C.R. Bowen, H.A. Kim, P.M. Weaver, S. Dunn, Piezoelectric and ferroelectric materials and structures for energy harvesting applications. Energ. Environ. Sci., 7 (2014) 25–44.
[2] J. Briscoe, S. Dunn, Piezoelectric nanogenerators—a review of nanostructured piezoelectric energy harvesters. Nano. Energ., 14 (2015) 15–29.
[3] X. Wang. Piezoelectric nanogenerators-harvesting ambient mechanical energy at the nanometer scale. Nano. Energ., 1 (2012) 13–24.
[4] Z.L. Wang, W. Wu, Nanotechnology-enabled energy harvesting for self-powered micro-/nanosystems. Angew. Chem. Int. Ed., 51 (2012) 11700– 11721.
[5] M. A. Karami and D. J. Inman. Powering pacemakers from heartbeat vibrations using linear and nonlinear energy harvesters. App. Phys. Lett. 2012,100, 042901-4.
[6] S.P. Beeby, M. J. Tudor and N.M. White. Energy harvesting vibration sources for microsystems applications. Meas. Sci.Tech. (17) 2006 R175---195.
[7] C. Chang, V.H. Tran, J. Wang, Y.-K. Fuh, L. Lin. Direct-write piezoelectric polymeric nanogenerator with high energy conversion efficiency. Nano Lett, 10 (2010) 726–731.
[8] Z.Y. Wang, J. Hu, A.P. Suryavanshi, K. Yum, M.F. Yu. Voltage generation from individual BaTiO3 nanowires under periodic tensile mechanical load. Nano. Lett. 7 (2007) 2966–2969.
[9] H.S. Kim, J.-H. Kim, J. Kim. A review of piezoelectric energy harvesting based on vibration. Int. J. Precis. Eng. Manuf. 12 (2011) 1129–41.
[10] S.R. Anton, H.A. Sodano. A review of power harvesting using piezoelectric materials (2003-2006). Smart Mater. Struct. 16 (2007) R1–21. .
[11] S. Priya, H.-C. Song, Y. Zhou, R. Varghese, A. Chopra, S.-G. Kim, I. Kanno, L. Wu, D. S. Ha, J. Ryu, R. G. Polcawich. A review on piezoelectric energy harvesting: materials, methods, and circuits. Energy Harvesting and Systems 4 (2019), 3-39.
[12] P.K. Panda & B. Sahoo. PZT to Lead Free Piezo Ceramics: A Review. Ferroelectrics, 474 (2015) 128-143.
[13] X. Wang. Piezoelectric nanogenerators—Harvesting ambient mechanical energy at the nanometer scale. Nano Energy, 2012,1, 13-24.
[14] Z. L. Wang, G. Zhu, Y. Yang, S. Wang, and C. Pan. Progress in nanogenerators for portable electronics. Mater. Today, 2012,15, 532-543.
[15] P. Hiralal, H. Unalan, and G. A. J. Amaratunga. Nanowires for energy generation. Nanotech., 2012,23, 194002.
[16] A. Nechibvute, A. Chawanda, and P. Luhanga. Wireless sensor networks for scada and industrial control systems. Smart Mater. Res. 3 (2013) 853481.
[17] S. Dunn, D. Tiwari, P.M. Jones, D.E.Gallardo. Insights into the relationship between inherent materials properties of PZT and photochemistry for the development of nanostructured silver. J.Mater. Chem. 17 (2007) 4460.
[18] S. Harada, S.Dunn. Low temperature hydrothermal routes to various PZT stoichiometries. J. Electroceram. 20 (2007) 65-71.
[19] E. Cagin, D.Y. Chen, J.J. Siddiqui, J.D. Phillips. Hysteretic metal–ferroelectric–semiconductor capacitors based on PZT/ZnO heterostructures. J. Phys. D Appl. Phys.40 (2007) 2430-2434.
[20]Y.Cui, J.Briscoe, S.Dunn. Effect of Ferroelectricity on Solar-Light-Driven Photocatalytic Activity of $BaTiO_3$ Influence on the Carrier Separation and Stern Layer Formation. Chemistry of Materials 25 (2014)4215- 4223.
[21] A. Koka, Z. Zhou, H.A. Sodano. Vertically aligned $BaTiO_3$ nanowire arrays for energy harvesting. Energy Environ. Sci. 7 (2014) 288-296.

[22] C.K. Jeong, K.-I. Park, J. Ryu, G.-T. Hwang, K.J. Lee. Large-area and flexible lead-free nanocomposite generator using alkaline niobate particles and metal nanorod filler. Adv. Funct. Mater. 24 (2014) 2620-2629.
[23] C. T. Huang, J. Song, W.-F. Lee, Y. Ding, Z. Gao, Y. Hao, L.-J. Chen and Z. L. Wang. GaN nanowire arrays for high-output nanogenerators. J. Am. Chem. Soc. 132 (2010) 4766-4771.
[24] J. Briscoe, N. Jalali, P. Woolliams, M. Stewart, P. M. Weaver, M. Cain and S. Dunn. Measurement techniques for piezoelectric nanogenerators. Energy Environ. Sci. 6 (2013) 3035-3045.
[25] L. Lin, Y. Hu, C. Xu, Y. Zhang, R. Zhang, X. Wen, Z. L. Wang. Transparent flexible nanogeneratoras self-powered sensor for transportation monitoring. Nano Energy 2 (2013) 75–81.
[26] C.E. Chang, Y-K Fuh, L. Lin, in A direct-write piezoelectric PVDF nanogenerator, transducers 2009, solid-state sensors, actuators and Microsystems conference, (Denver, 2009) p. 1485–1488.
[27] S.N. Cha, S.M. Kim, H. Kim, J. Ku, J.I. Sohn, Y.J. Park, B.G. Song, M.H. Jung, E.K. Lee, B.L. Choi, J.J. Park, Z.L. Wang, J.M. Kim, K. Kim. Porous PVDF as effective sonic wave driven nanogenerators. Nano. Lett., 11 (2011) 5142–5147.
[28] L. Csoka, C. I. Hoeger, J. R. Orlando, I. Peszlen, J. J. Pawlak. Piezoelectric Effect of Cellulose Nanocrystals Thin Films. ACS Macro letters 2012, 1, 867−870.
[29] J. Kim, S. Yun, Z. Ounaies. Discovery of Cellulose as a Smart Material. Macromolecules 39 (2006) 4202-4206.
[30] S. Yun, J. H. Kim, Y. Li, J. Kim. Alignment of cellulose chains of regenerated cellulose by corona poling and its piezoelectricity. Journal of Applied Physics 103 (2008) 083301.
[31] P. Thakur, A. Kool, N. A. Hoque, B. Bagchi, F. Khatun, P. Biswas, D. Brahma, S. Roy, S. Banerjeeb, S. Das. Superior performances of in situ synthesized ZnO/PVDF thin film based self-poled piezoelectric nanogenerator and self-charged photo-power bank with high durability. Nano energy 44, (2018) 456-467.
[32] S.K. Mahadeva, K. Walus, B. Stoeber Piezoelectric Paper Fabricated via Nanostructured Barium Titanate Functionalization of Wood Cellulose Fibers. ACS Appl. Mater. Interfaces 6 (2014) 7547-7553.
[33] H. Gullapalli, V. S. M. Vemuru, A. Kumar, A. Botello-Mendez, R. Vajtai, M. Terrones, S. Nagarajaiah, P. M. Ajayan. Flexible Piezoelectric ZnO–Paper Nanocomposite Strain Sensor. Small 6 (2010) 1641–1646.
[34] L. Loh, S. Dunn, Recent Progress in ZnO-Based Nanostructured Ceramics in Solar Cell Applications, Journal of nanoscience and nanotechnology 12 (2012) 8215-8230.
[35] S.M. Hatch, J. Briscoe, S. Dunn. Improved CuSCN–ZnO diode performance with spray deposited CuSCN. Thin Solid Films 531 (2013) 404-407.
[36] S. Gupta, D. Maurya, Y. Yan, S. Priya. Development of KNN-based piezoelectric materials. In: Priya S, Nahm S, editors. Lead-free piezoelectrics. New York: Springer; 2012. p. 89–119.]
[37] Z.-H. Lin, Y. Yang, J.M. Wu, Y. Liu, F. Zhang, Z.L. Wang. BaTiO3 nanotubes-based flexible and transparent nanogenerators. J Phys Chem Lett 3 (2012) 3599–604.
[38] S.K. Mahadeva, K. Walus, B. Stoeber. Piezoelectric paper fabricated via nanostructured barium titanate functionalization of wood cellulose fibers. ACS Appl Mater Interfaces 6 (2014) 7547–53.
[39] S.-H. Shin, Y.-H. Kim, M.H. Lee, J.-Y. Jung, J. Nah. Hemispherically aggregated BaTiO3 nanoparticle composite thin film for high-performance flexible piezoelectric nanogenerator. ACS Nano 8 (2014) 2766–73.
[40] C.K. Jeong, I. Kim, K.-I. Park, M.H. Oh, H. Paik, G.-T. Hwang, et al. Virus-directed design of a flexible BaTiO3 nanogenerator. ACS Nano 7 (2013) 11016–25.

[41] J. Yan, Y.G. Jeong. High performance flexible piezoelectric nanogenerators based on BaTiO3 nanofibers in different alignment modes. ACS Appl Mater Interfaces 8 (2016) 15700–9.
[42] J. Yan, Y.G. Jeong. Roles of carbon nanotube and BaTiO3 nanofiber in the electrical, dielectric and piezoelectric properties of flexible nanocomposite generators. Compos Sci Technol 144 (2017) 1–10.
[43] X. Wang, X. Deng, H. Wen, L. Li. Phase transition and high dielectric constant of bulk dense nanograin barium titanate ceramics. Appl Phys Lett 89 (2006) 162902.
[44] Ertuğ B. The overview of the electrical properties of barium titanate. Am J Eng Res 2 (2013):1–7.
[45] R. Zhu, W. Zhang, R. Yang. High output piezoelectric nanogenerator: development and application. Sci Adv Mater 4 (2012) 798–804.
[46] L. Xu, Y. Hu, Candice I. Pelligra, C. Chen, L. Jin, H. Huang, S. Sithambaram, M. Aindow, R. Joesten, S. Suib. ZnO with Different Morphologies Synthesized by Solvothermal Methods for Enhanced Photocatalytic Activity. Chemistry of Materials 21 (2009) 2875-2885.
[47] B. Cheng, E.T. Samulski. Chem. Comm. 8 (2004) 986-987.
[48] S.K.N. Ayudhya, P. Tonto, O. Mekasuwandumrong, V. Pavarajarn, P. Praserthdam. Cryst. Growth Des. 6(11) (2006) 2446-2450.
[49] H.M. Cheng, H.C. Hsu, S.L. Chen, W.T. Wu, C.C. Kao, L.J. Lin, W.F.J. Hsieh. Cryst. Growth 277 (1-4) (2005) 192-199.
[50] C.Fauteux, R. Longtin, J. Pegna, D. Therriault. Inorg. Chem. 46(26) (2007) 11036-11047.
[51] S.H. Jung, E. Oh, K.H. Lee, Y. Yang, C. G. Park, W. Park, S.H. Jeong. Cryst. Growth. Des. 8(1) (2008) 265-269.
[52] D.K. Bhat, Nanoscale Res. Lett. 3(1) (2008) 31-35.
[53] M.-Y. Choi, D. Choi, M.-J. Jin, I. Kim, S.-H.S.-W. Kim, J.-Y. Choi, S.Y. Lee, J.M. Kim. Mechanically Powered Transparent Flexible Charge-Generating Nanodevices with Piezoelectric ZnO Nanorods. Adv. Mater. 21 (2009) 2185
[54] R.A. Surmenev, T. N. Orlova, R.V. Chernozem, A.A. Ivanova, A. Bartasyte, S. Mathu, M.A. Surmeneva. Hybrid lead-free polymer-based scaffolds with improved piezoelectric response for biomedical energy-harvesting applications: A review. Nano Energy 62 (2019) 475–506.
[55] M.A. Rahman, B.-C. Lee, D.-T. Phan, G.-S. Chung. Fabrication and characterization of highly efficient flexible energy harvesters using PVDF–graphene nanocomposites. Smart Mater. Struct. 22 (2013) 085017.
[56] J. Chang, M. Dommer, C. Chang, L. Lin. Piezoelectric nanofibers for energy scavenging applications Nano Energy 1 (2012) 356-371.
[57] M. Sajad Sorayani Bafqi, R. Bagherzadeh, M. Latifi, Fabrication of composite PVDF-ZnO nanofiber mats by electrospinning for energy scavenging application with enhanced efficiency, J. Polym. Res. 22 (2015) 130-138.
[58] Bazhenov, V. A. Piezoelectric Properties of Woods; Consultants Bureau: New York, 1961.
[59] N. Soin, T.H. Shah, S.C. Anand, J. Geng, W. Pornwannachai, P. Mandal, D. Reid, S. Sharma, R.L. Hadimani, D.V. Bayramol, E. Siores, Novel “3-D spacer” all fibre piezoelectric textiles for energy harvesting applications. Energy Environ Sci. 7 (2014) 1670–1679.
[60] J. Granstrom, J. Feenstra, H.A. Sodano, K. Farinholt. A review of power harvesting from vibration using piezoelectric materials. Smart Mater. Struct., 16 (2007) 1810-1820.
[61] X. Bian, H.Jin, , X. Wang, et al. UV sensing using film bulk acoustic resonators based on Au/n-ZnO/piezoelectric-ZnO/Al structure. Sci Rep 5, (2015) 9123-9127.
[62] Z.L. Wang, J.H. Song. Piezoelectric nanogenerators based on zinc oxide nanowire arrays. Science 312 (2006) 242–246.

[63] J. Briscoe, S. Dunn. Piezoelectric nanogenerators—a review of nanostructured piezoelectric energy harvesters. Nano Energy 14 (2015) 15–29.
[64] X. Wang. Piezoelectric nanogenerators-harvesting ambient mechanical energy at the nanometer scale. Nano Energy 1 (2012) 13–24.
[65] Z.L. Wang, W. Wu. Nanotechnology-enabled energy harvesting for self-powered micro-/nanosystems. Angew. Chem. Int. Ed. 51 (2012) 11700–11721.
[66] F.R. Fan, W. Tang, Z.L. Wang. Flexible Nanogenerators for Energy Harvesting and Self-Powered Electronics. Adv. Mater. 28 (2016) 4283-305.
[67] Q. Yang, W. Wang, S. Xu, and Z. L. Wang. Enhancing Light Emission of ZnO Microwire-Based Diodes by Piezo-Phototronic Effect. Nano Letters 11 (2011) 4012-4017.
[68] Q. Yang, Xin Guo, W. Wang, Y. Zhang, S. Xu, D. H. Lien, and Z. L. Wang. Enhancing Sensitivity of a Single ZnO Micro-/Nanowire Photodetector by Piezo-phototronic Effect. ACS Nano 4 (2010) 6285–91.
[69]E. Lee, J. Park, M. Yim, Y. Kim, and G. Yoon. Characteristics of piezoelectric ZnO/AlN2 stacked flexible nanogenerators for energy harvesting applications. Appl. Phys. Lett. 106 (2015) 023901-5.
[70] Y. Hu, Z.L. Wang. Recent progress in piezoelectric nanogenerators as a sustainable power source in self-powered systems and active sensors. Nano Energy Volume 14(2015) 3-14.
[71] H. J. Fan, W. L., R. Hauschild, M. Alexe, G. Le Rhun, R. Scholz, A. Dadgar, K. Nielsch, H. Kalt, A. Krost, M. Zacharias, and U. Gösel. Template-Assisted Large-Scale Ordered Arrays of ZnO Pillars for Optical and Piezoelectric Applications. Small 2 (2006) 561-568.
[72] K. Prashanthi, H. Zhang, V. Ramgopal Rao and T. Thundat. Local piezoelectric response of ZnO nanoparticles embedded in a photosensitive polymer. Phys. Status Solidi RRL 6, No. 2 (2012) 77–79.
[73] M. Kandpal, C. Sharan, P. Poddar, K. Prashanthi, P. R. Apte, and V. R. Rao. Photopatternable nano-composite (SU-8/ZnO) thin films for piezoelectric applications. Applied Physics Letters 101, (2012) 104102-5.
[74] C. Li, Y. Xie, Q. Liu, Y. Zheng, X. Zhang, W. Dong. The formation and UV-blocking property of flower-like ZnO nanorod on electrospun natural cotton cellulose nanofibers. Fibers and Polymers 15 (2014) 281-285.
[75] A. Kumar, H. Gullapalli, K. Balakrishnan, A. Botello-Mendez, R. Vajtai, M. Terrones, P.M. Ajayan. Flexible ZnO-cellulose nanocomposite for multisource energy conversion. Small 7 (2011) 2173-8.
[76] E. Saleh, P. Woolliams, B. Clarke, A. Gregory, S. Greedy, C. Smartt, R. Wildman, I. Ashcroft, R. Hague, P. Dickens, C. Tuck. 3D inkjet-printed UV-curable inks for multi-functional electromagnetic applications**,** Addit. Manuf. 12 (2017) 143-148.
[77] S. Banerjee, K.A. Cook-Chennault, W. Du, U. Sundar, H. Halim, A. Tang. Piezoelectric and dielectric characterization of corona and contact poled PZT-epoxy-MWCNT bulk composites. Smart Mater. Struct. 25 (2016) 115018.
[78] H.M. Rietveld. Line profiles of neutron powder-diffraction peaks for structure refinement. Acta Crystallogr. 22 (1967) 151-152.
[79] D.B. Wiles, R.A. Young. A new computer program for Rietveld analysis of X-ray powder diffraction patterns. J. Appl. Crystallogr. 14 (1981) 149-151.
[80] U. Holzwart, N. Gibson. The Scherrer equation versus the 'Debye-Scherrer equation. Nat. Nanotechnol. 6 (2011) 534.
[81] Segal L, Creely JJ, Martin AE Jr., Conrad CM. An empirical method for estimating the degree of crystallinity of native cellulose using the X-ray diffractometer. Text Res J 29 (1959) 786–794.
[82] Al Ahmad, M., Allataifeh, A. Electrical extraction of piezoelectric constants, Heliyon 4 (2018) 00910-15.

[83] G. Malucelli, A. Fioravanti, L. Francioso, C. De Pascali, M.A. Signore, M.C. Carotta, A. Bonanno, D. Duraccio. Preparation and characterization of UV-cured composite films containing ZnO nanostructures: Effect of filler geometric features on piezoelectric response. Progress in Organic Coatings 109 (2017) 45–54.
[84] C.J. Garvey, I.H. Parker, G.P. Simon. On the interpretation of X-ray diffraction powder patterns in terms of the nanostructure of cellulose I fibers. Macromol Chem Phys 206 (2005) 1568–1575.
[85] A.D. French, C.M. Santiago. Cellulose polymorphy, crystallite size, and the Segal crystallinity. Cellulose 20 (2013) 583–588.
[86] Y. Nishiyama, P. Langan, H. Chanzy. Crystal structure and hydrogen-bonding system in cellulose Ib from synchrotron X-ray and neutron fiber diffraction. J Am Chem Soc 124 (2002) 9074– 082.
[87] M. Ago, T. Endo, T. Hirotsu. Crystalline transformation of native cellulose from cellulose I to cellulose II polymorph by a ball-milling method with a specific amount of water. Cellulose 11(2004) 163–167.
[88] A. Thygesen, J. Oddershede, H. Lilholt, A. B. Thomsen, K. Ståhl. On the determination of crystallinity and cellulose content in plant fibre. Cellulose (2005) 12 563–576.
[89] M. Schwanninger, J.C. Rodrigues, H. Pereira, B. Hinterstoisser. Effects of short-time vibratory ball milling on the shape of FT-IR spectra of wood and cellulose Vibrational Spectroscopy 36 (2004) 23–40.
[90] S. Jafarzadeh, M. Johansson, P.E. Sundell, M. Claudino, J. Pan, P. M. Claesson. UV-curable acrylate-based nanocomposites: effect of polyaniline additives on the curing performance. Polym. Adv. Technol. 24 (2013) 668–678.
[91] G. Socrates. Infrared and Raman Characteristic Group Frequencies: Tables and Charts, 3rd ed.; Wiley: New York, NY, USA, 2004.
[92] M. Roman and W.T. Winter. Effect of Sulphate Groups from Sulfuric Acid Hydrolysis on the Thermal Degradation Behavior of Bacterial Cellulose. Biomacromolecules 5 (2004) 1671-1677.
[93] M. Rahimi Kord Sofla, R.J. Brown, T. Tsuzuki, T.J. Rainey. Adv. Nat. Sci: Nanosci. Nanotechnol.7 (2016) 035004-12.
[94] H Kargarzadeh, I Ahmad, I Abdullah, A Dufresne, S.Y. Zainudin and R.M. Sheltami. Effects of hydrolysis conditions on the morphology, crystallinity, and thermal stability of cellulose nanocrystals extracted from kenaf bast fibers. Cellulose 19 (2012) 855-866.
[95] A. Arbelaiz A, B. Fernandez, J. Ramos, I. Mondragon. Thermal and crystallization studies of short flax fibre reinforced polypropylene matrix composites: Effect of treatments. Thermochimica Acta 2 (2006) 111-121.
[96] S. Julien, E. Chornet, R.P.J. Overend. Influence of acid pretreatment (H_2SO_4, HCl, HNO_3) on reaction selectivity in the vacuum pyrolysis of cellulose Anal. Appl. Pyrolysis 27 (1993) 25-43.
[97] H.M. Lee, P. Tarakeshwar, J. Park, M.R. Kołaski, Y. Jin Yoon, H.B. Yi, W.Y. Kim, K.S. Kim. Insights into the structures, energetics, and vibrations of monovalent cation-(water) 1-6 clusters. J. Phys. Chem. A 108 (2004) 2949-2958.
[98] K. Chrissafis, K.M. Paraskevopoulos, E. Pavlidou, D. Bikiaris. Thermal degradation mechanism of HDPE nanocomposites containing fumed silica nanoparticles. Thermochim Acta 485 (2009) 65-71.
[99] S. Sinha Ray, M. Bousmina. Biodegradable polymers and their layered silicate nanocomposites: in greening the 21st century materials world. Prog. Mater. Sci. 50 (2005) 962-1079.
[100] S. Xu, N. Girouard, G. Schueneman, M. L. Shofner, J. Carson Meredith. Mechanical and thermal properties of waterborne epoxy composites containing cellulose nanocrystals, Polymer 54 (2013) 6589-6598.

[101] P. Dhar, D. Tarafder, A. Kumar and V. Katiyar. Effect of cellulose nanocrystal polymorphs on mechanical, barrier and thermal properties of poly(lactic acid) based bionanocomposites. Adv. RSC, 2015, 5, 60426-440.
[102] H.-Y. Yu, Z.-Y. Qin, L. Liu, X.-G. Yang, Y. Zhou, J.-M. Yao. Comparison of the reinforcing effects for cellulose nanocrystals obtained by sulfuric and hydrochloric acid hydrolysis on the mechanical and thermal properties of bacterial polyester. Composites Science and Technology 87 (2013) 22–28.
[103] A. Dorigato, A. Pegoretti, Y. Dzenis. Filler aggregation as a reinforcement mechanism in polymer nanocomposites. Mech. Mater. 61 (2013) 79-90.
[104] O. Zabihia, S.M. Mostafavi, F. Ravari, A. Khodabandeh, A. Hooshafza, K. Zare, M. Shahizadeh, The effect of zinc oxide nanoparticles on thermo-physical properties of diglycidyl ether of bisphenol A/2,2′-diamino-1,1′-binaphthalene nanocomposites. Thermochim. Acta 521 (2011) 49-58.
[105] L.E. Nielsen, R.F. Landel. Mechanical properties of polymers and composites. Marcel Dekker, New York, 1994.
[106] G. Jimenez, N. Ogata, H. Hawai, T. Ogihara, Structure and thermal/mechanical properties of poly (ϵ-caprolactone)-clay blend. J. Appl. Polym. Sci. 64 (1997) 2211-2220.
[107] Z. L. Wang. Zinc Oxide nanostructures: growth, properties and applications. J. Phys.: Condens. Matter, 16 (2004) R829.
[108] R. A. Surmenev, T. Orlova R. V. Chernozem A. A. Ivanova A. Bartasyte S. Mathur, M. A. Surmeneva.Hybrid lead-free polymer-based nanocomposites with improved piezoelectric response for biomedical energy-harvesting applications: A review. Nano Energy 62 (2019) 475–506,
[109] E. J. Lee, T. Y. Kim, S.-W. Kim, S. Jeong, Y. Choi, S. Y. Lee. High-performance piezoelectric nanogenerators based on chemically-reinforced composites. Energy Environ. Sci. 11 (2018) 1425–1430.
[110] M. Lee, J. Bae, J. Lee, C.-S. Lee, S. Hong, Z.L. Wang. Self-powered environmental sensor system driven by nanogenerators. Energy Environ. Sci. 4 (2011) 3359-3363.
[111] G. Zhang, P. Zhao, X. Zhang, K. Han, T. Zhao, Y. Zhang, C.K. Jeong, S. Jiang, S. Zhang, Q. Wang. Flexible three-dimensional interconnected piezoelectric ceramic foam based composites for highly efficient concurrent mechanical and thermal energy harvesting. Energy Environ. Sci. 11 (2018) 2046-2056.
[112] Y. C. Yang, C. Song, X. H. Wang, F. Zeng, and F. Pan. Giant piezoelectric d33 coefficient in ferroelectric vanadium doped ZnO films. Appl. Phys. Lett. 92 (2008) 012907-3.
[113] Y.-H. Lin M. Ying, M. Li, X. Wang, C.-W. Nan. Room-temperature ferromagnetic and ferroelectric behavior in polycrystalline ZnO based thin films. Appl. Phys. Lett. 90 (2007) 222110-2.